Shining Diamond:
from Micro- and Nano-Engineering to Quantum Photonics

Présentée le 31 mars 2021

Faculté des sciences et techniques de l'ingénieur
Groupe Quack
Programme doctoral en photonique

pour l'obtention du grade de Docteur ès Sciences

par

Sichen MI

Acceptée sur proposition du jury

Prof. L. Thévenaz, président du jury
Prof. N. Quack, directeur de thèse
Prof. I. Aharonovich, rapporteur
Prof. M. Loncar, rapporteur
Prof. C. Galland, rapporteur

■ École
polytechnique
fédérale
de Lausanne

2021

Acknowledgements

To start with, I thank my thesis supervisor Prof. Niels Quack, for putting his bet on me among dozens of phd applicants shortly after he launched his lab at EPFL. Without this opportunity, I wouldn't have been able to go from knowing nothing about diamond fabrication to writing this text, neither could I have enjoyed the sunshineless cleanroom and the breathtaking lac Léman. Niels has always been keen on sharing everything interesting he knows, and what I learnt from him goes way beyond science and technology.

I owe my gratitude to Prof. Igor Aharonovich, Prof. Marko Lončar and Prof. Christophe Galland for reviewing this work and serving as jury members in the examination committee, and I cannot thank enough Prof. Luc Thévenaz for serving as the president for both my candidacy exam and my doctoral defense. This committee shares sixteen hours of time diffrence and only with every professor's kindness and professionalism could it have become possible. Your comments are invaluable for me in finalizing this thesis.

I thank Dr. Teodoro Graziosi and Dr. Marcell Kiss [1] for being my colleagues and friends. I only put colleague before friend because this is my thesis and it is a professional outcome. You two are definitely more of a friend to me than a colleague. If you will allow me to put it simple, this thesis would not have been possible without your works and, much more importantly, the personal supports you have lent me.

For the rest of the team, I would start with thanking Adrien Toros for always being a kind and warm-hearted local Lausannois, especially during the early time when I struggled to adapt to a French-speaking environment. I shall also not forget that you taught me so much which put me into work quickly in the cleanroom. I appreciate a lot the help from Dr. Gergely Huszka who shared his cleanroom top-secret recipe with me so that I can accelerate my fabrication works. I thank the MORPHIC subteam, Alain Yuji Takabayashi, Dr. Hamed Sattari, and Dr. Yu Zhang, from whom I received much support both in work and in life, especially the delicious meals at Yuji's place. I thank Dorian Herle who was my most frequent visitor in the office on weekends, for keeping me less lonely, for his youth tricking me into falsely feeling young of myself, and for him kindly translating the abstract of this thesis into Deutsch. I thank Dr. Hernan Fernando Furci, Dr. Micol Previde Massara, Dr. Anton Lagosh, Dr. Anna Varini and Dr. Elena Losero who joined us recently, as their diverse research backgrounds have made me learn so much that I wouldn't have learnt otherwise. And to Mrs. Beatrice Raball: Grazie mille for your constant patience in the administrative works in our group.

---

[1] Not pronounced as kiss in English

Abstract

The discovery of room-temperature single photon emission from color centers in diamond has in recent years boosted research interest in this renowned material in photonics and quantum community and beyond. Following understanding some basic principles of how the color centers work, new challenges arose: designing and fabricating real devices that leverage the unrivaled properties that diamond possesses. Due to this material's extreme physical hardness and its chemical resistance to etchants, the established semiconductor technologies cannot straightforwardly answer to the call for scalable and reliable fabrication of micro- and nano-photonic devices in single crystal diamond. In this thesis, we first demonstrate an unconventional polishing protocol with ion beam etching, which makes possible wafer-scale fine finishing of diamond substrates, the starting point for any subsequent processing. Following this we present the experimental observation of self-organized nanotextures on diamond induced by ion beam irradiation, a lithography-free approach for nanoengineering periodic structures. Regarding device fabrication, we obtained free-standing micro- and nano-photonic structures using angled reactive ion etching, facilitated by a novel and reproducible Faraday cage design. We also propose possible designs to interconnect individual components in hope of realizing a photonic integrated circuit in the future. Last but not least, we present spectroscopic characterization of single and ensemble color centers either grown by microwave plasma chemical vapor deposition, or fabricated by ion implantation with subsequent high-temperature annealing, which are the fundamental building blocks for quantum applications. Photoluminescence spectra that, to our knowledge, are not seen in literature were recorded for ensemble silicon-vacancy centers at cryogenic temperature, signifying potentially unknown mechanism for tuning the optical transitions, and unexplored possibilities with this exciting material platform for quantum technologies.

Keywords: diamond, color center, microfabrication, quantum photonics

Zusammenfassung

Die Entdeckung der Einzelphotonenemission von Farbzentren in Diamant bei Raumtemperatur hat in den letzten Jahren das Forschungsinteresse an diesem renommierten Material in der Photonik- und Quantencommunity und darüber hinaus verstärkt. Dem Verständnis einiger grundlegender Prinzipien, aus denen sich die Funktionsweise der Farbzentren ergibt, folgten neue Herausforderungen: die Entwicklung und Herstellung echter Geräte, die die unvergleichlichen Eigenschaften des Diamanten nutzen. Aufgrund der extremen physikalischen Härte dieses Materials und seiner chemischen Beständigkeit gegen Ätzmittel können die etablierten Halbleitertechnologien nicht ohne weiteres auf die Forderung nach skalierbarer und zuverlässiger Herstellung von mikro- und nanophotonischen Bauelementen in einkristallinem Diamant antworten. In dieser Arbeit demonstrieren wir zunächst ein unkonventionelles Polierprotokoll mit Ionenstrahlätzen, das eine Feinbearbeitung von Diamantsubstraten im Wafermaßtab ermöglicht, die den Ausgangspunkt für jede nachfolgende Bearbeitung darstellt. Im Folgenden stellen wir die experimentelle Erfassung von selbstorganisierten Nanotexturen auf Diamant vor, die durch Ionenstrahlbestrahlung induziert wurden: ein lithographiefreier Ansatz für das Herstellen periodischer Strukturen. Bei der Herstellung von Bauelementen haben wir freistehende mikro- und nano-photonische Strukturen durch angewinkeltes reaktives Ionenätzen hergestellt, erleichtert durch ein neuartiges und reproduzierbares Faraday-Käfig-Design. Des weiteren, präsentieren wir mögliche Designs, um einzelne Komponenten miteinander zu verbinden, in der Hoffnung, in Zukunft einen photonischen integrierten Schaltkreis zu realisieren. Zu guter Letzt stellen wir die spektroskopische Charakterisierung von Einzel- und Ensemble-Farbzentren vor, die entweder durch mikrowellenplasmachemische Gasphasenabscheidung gezüchtet oder durch Ionenimplantation mit anschließender Hochtemperatur-Temperung hergestellt wurden und die die grundlegenden Bausteine für Quantenanwendungen darstellen. Photolumineszenzspektren, die unseres Wissens nach nicht in der Literatur zu finden sind, wurden für Ensemble-Silizium-Vakanzzentren bei kryogener Temperatur aufgezeichnet, was auf einen möglicherweise unbekannten Mechanismus zur Abstimmung der optischen Übergänge und unerforschte Möglichkeiten mit dieser spannenden Materialplattform für Quantentechnologien hinweist.

Schlüsselwörter: Diamant, Farbzentrum, Mikrofabrikation, Quantenphotonik

Contents

List of Figures

List of Tables

List of Abbreviations

AFM	Atomic force microscpy
ALD	Atomic layer deposition
AuNPs	Gold Nanoparticles
DOI	Diamond-on-insulator
FCC	Face-centered cubic
FDM	Finite difference method
FEM	Finite element method
IBE	Ion beam etching
HBT	Hanbury Brown-Twiss
HPHT	High-pressure high-temperature
HSQ	Hydrogen silsesquioxane
MPCVD	Microwave plasma chemical vapor deposition
NV	Nitrogen-Vacancy
ODMR	Optically detected magnetic resonance
PCD	Polycrystalline diamond
PDE	Partial differential equation
PECVD	Plasma enhanced chemical vapor deposition
PIC	Photonic integrated circuits
PL	Photoluminescence
PLE	Photoluminescence excitation
r.h.s	Right hand side
RIE	Reactive ion etching
SCD	Single crystal diamond
SEM	Scanning electron microscopy
SiV	Silicon-Vacancy
SOI	Silicon-on-insulator
ZPL	Zero phonon line

1 Introduction

Billions of years prior to human history had diamond come to earth [1]. Its name originated from ancient Greek ἀδάμας, meaning unbreakable, and up to date it still remains the hardest known bulk material [1]. Because of its hardness, long before diamond was marketed as a gem, human had started using it as a tool — the earliest application of diamond in human activity is believed to date back to 2500 B.C. in Neolithic China, for polishing corundum till a mirror-like surface [5].

Literature has noted since early Christian times many properties of diamond that lure men and women. In *Naturalis Historia* [6] for instance, Pliny the Elder goes:

There is the Indian octahedral diamond, which is not formed in gold and has a certain affinity with rock-crystal, which it resembles in its transparency and in its smooth faces meeting at six corners.

The hardness of the diamond defies description, and similarly that property by which it resists fire yet never becomes hot.

These short descriptions already covered four important characteristics that diamond has: it is an optically transparent crystalline material with ultra-high hardness and thermal conductivity.

In fact, these properties may well have passed what scholars at that time could grasp. Except for a small window from 2.6 to 6.2 μm due to two-, three- and four-phonon absorption, the transparency of diamond spans from 235 nm to 500 μm [7], way beyond the range that human vision can feel. The thermal conductivity of diamond is the highest of all materials and it is therefore deemed as the ultimate solution for thermal management in high-power electronics and microwave photonics. The unrivaled hardness of diamond made possible room-temperature[2] superconductivity in carbonaceous sulfur hydride under a pressure of 267 GPa [8], the first and so far the only one of its kind ever known to human.

---

[1]Some thin films of nanomaterials were claimed to be harder than diamond [2, 3, 4].
[2]The critical temperature measured in this sample was 287 K: temperature of a chilly room.

Interestingly, despite its first popularization in the European elite society during 1400s, it was not until 1772 when French chemist Antoine-Laurent Lavoisier burned diamond in oxygen with CO_2 being the only product that people became aware of that this precious jewelry is composed only of carbon atoms - the fundamental ingredient of coal and pencils.

Taking a leap to the 3rd millennium, the quest for better understanding diamond in our time has been boosted by another new finding [9] in 2000 in Germany: a color center hosted in diamond can emit single photons even at room-temperature. Very soon its advantage over faint laser pulses in the field of quantum cryptography was demonstrated [10], and these discoveries undoubtedly placed diamond as an important, if not irreplaceable, resource in the quantum age. Not surprisingly, the diamond mine has quickly attracted increasing interest from researchers all over the world, and in two decades we have witnessed its application in a wide range of cutting-edge technologies such as quantum sensing, computing, communication, imaging, *etc.*

With all these possibilities that diamond promises, technologies for the miniaturization and scaling-up of diamond-based devices became in great demand. However, the fabrication of diamond devices is not a trivial task and we will need to invent novel technologies to shape diamond the way we fancy, which is the topic that will be discussed in detail in this thesis.

In the next chapter, an overview of the field of diamond photonics is laid out, following which we introduce ion beam etching as a versatile tool for the scalable engineering of diamond surfaces in Chap. 3 and 4. After this, we demonstrate angled reactive ion etching for the fabrication of free-standing structures, and discuss about the design optimization for on-chip couplers with this processing technique (Chap. 5). In Chap. 6 we present the optical characterization results of color centers in diamond which are the core for quantum applications. By the end of this thesis, a brief discussion about integrated diamond photonics platform is given, where some open questions are addressed and possibilities envisaged.

2 Diamond for Photonics

We begin with introducing the basic properties of diamond and color centers, following which the applications of diamond photonics are briefly summarized to give an idea about the context of this thesis work.

2.1   Material Properties of Diamond

Diamond [1] is a crystalline material composed of carbon atoms in a pair of intersecting FCC (face-centered cubic) lattices as shown in Fig. 2.1. Due to the small atomic size of carbon and tightly bound crystal structure, extreme properties result, which are compared with other common optical materials in Table. 2.1. In addition to its favorable physical properties, diamond is also corrosion resistant, making it suitable for applications in harsh environments [11, 12].

The wide bandgap of ~ 5.5 eV gives diamond not only a large transparency window but also the possibility to host various color centers [15] — atomic-size defects that form additional energy levels in the bandgap, which absorb light in the visible wavelength, giving diamond a colorful appearance. Such defects can be as simple as a GR1 center [16], which is merely a vacancy in the carbon lattice. We will dive into this topic in the next section, as it is the core ingredient for diamond gaining its popularity as a quantum photonics platform.

In spite of the advantageous properties this material possesses, only recently has it become feasible to obtain (relatively) large diamond substrates with well-controlled impurity level and high crystallinity, thanks to the progress in synthesizing diamond via microwave plasma chemical vapor deposition (MPCVD) [17]. In contrast, natural diamonds are with properties that vary from one sample to another (let alone its cost), and HPHT diamond (high pressure high temperature synthesized diamond) not only has limited dimensional extent restricted by

---

[1] Unless specifically noted, we refer to single crystal diamond (SCD) all the time, as polycrystalline diamond has grain boundaries that introduces additional optical loss and the orientation of color centers formed in such material is out of control.

Table 2.1 – A comparison of physical properties among common optical materials

	Diamond	Si	SiO_2	Si_3N_4	Al_2O_3	$LiNbO_3$	GaN
Refractive index (@ 633 nm)[†]	2.41	3.86[*]	1.46	2.04	1.77	2.29	2.38
Bandgap (eV)	5.5	1.14	8.9	5.3	8.7	4	3.4
Young's modulus (GPa)	1050	169	97	230	350	170	338
Thermo-optic coefficient (K^{-1})	1E-6	5.15E-5	1E-5	2.5E-5	5.1E-6	1.7E-6	1.6E-4
Thermal conductivity ($W \cdot m^{-1} \cdot K^{-1}$)	2200	130	1.4	30	34.6	38	130

Note: [†]The experimentally measured physical quantities are usually within a range and depend highly on the crystallinity and crystallography. The values quoted here are only indicative [13].

[*]The refractive index for silicon (single crystal) at 633 nm is complex [14] (3.8636+0.015796i) due to its narrow bandgap.

the growth apparatus but also suffers from uncontrolled impurity incorporation. [2]

2.2 Diamond Quantum Photonics

In this chapter we explain what makes a color center and why they are important for quantum applications, after which we discuss about the elementary components needed for integrated quantum photonics, and give a brief overview of demonstrated applications with this material platform. The field is too vast to be comprehensively covered in this overview section, and dedicated review articles such as Ref. [19, 20, 21, 22, 23, 24, 25, 26] can be found in literature.

2.2.1 Color Centers

Up to now over 500 kinds of color centers have been discovered in diamond [15, 25], identifiable by their different spectral responses. While the molecular structures and physical properties are not studied in depth for all of them, a few well-understood color centers already can be fabricated under various degrees of control. For example, the abovementioned GR1 center can be created via ion implantation as some of the carbon atoms are displaced by accelerated ions from its original lattice position, leaving a vacancy. The C centers [27] are the simplest nitrogenous defects in diamond which are just substitutional nitrogen atoms and can be incorporated into diamond during growth. The most famous and extensively studied NV center consists of a nearest neighbor pair of a substitutional nitrogen atom and a lattice

---

[2]Since the synthesis of diamond is a complex topic deserving a whole chapter (if not more), yet all diamond substrates used in this thesis are not grown by ourselves, we refer interested readers to [18] for more information on diamond substrate technologies. We will only briefly touch the topic of homoepitaxial growth in Chap. 5 in the context of thin film fabrication.
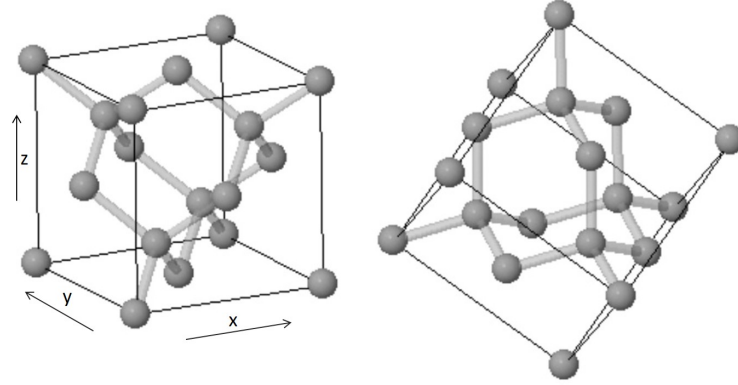
Figure 2.1 – The conventional unit cell of diamond viewed at different angles: the crystal structure is composed of two intersecting FCC lattices, offset from one another along a body diagonal by 1/4 of its length. At room temperature, the cubic side length approximately equals to 3.567 Å, with C–C bond length d ≈ 1.54 Å. The conventional cell contains equivalently 8 whole C atoms, and with these numbers one can calculate the atomic density to be around 1.76E23 atoms/cm^3.

vacancy, and it can be fabricated through various techniques that will be detailed in Chap. 6. The chemical composition can also be more complicated, involving more than one foreign elements, such as NE8 center [28] which is composed of one nickel atom surrounded by four nitrogen atoms. The incorporation of this color center into diamond requires the presence of nickel and nitrogen during crystal growth.

As mentioned in Sec. 2.1, color centers form additional energy-levels within the bandgap of diamond. As an example, we show in Fig. 2.2 the energy-level diagrams of negatively and neutrally charged NV centers [30, 29]. Given the resemblance of their properties (such as optical transition and spin manipulation) to individually trapped atoms, they are also called artificial atoms, and their natural embedment within solid-state systems allows large-scale integration of devices or even circuits that enable sophisticated light-matter interactions on a chip, with possible applications such as, but not limited to, those in Table 2.2. It is worth noting that in contrast to real isolated atoms, being hosted in a solid-state matrix makes these artificial atoms suffer from inhomogeneous local environment such as strain and electrical fields caused by nearby crystalline defects or impurities, leading to slight difference in energy-levels among individual color centers, inhibiting coherent interaction between remote nodes. By engineering, however, it is possible not only to spectrally align their transitions [31, 32, 33], but also to improve their properties such as increased spin coherence time [34, 35]. Furthermore, compared to quantum dots [36] in III-V compound semiconductors, another material platform being actively studied for integrated quantum photonics, diamond color centers allow direct integration of both single photon sources and long coherence time quantum memories [37, 38] in highly transparent hosting materials [39], facilitating low-loss light routing on a chip. Consequently, together with the fabrication technologies for integrated diamond photonics
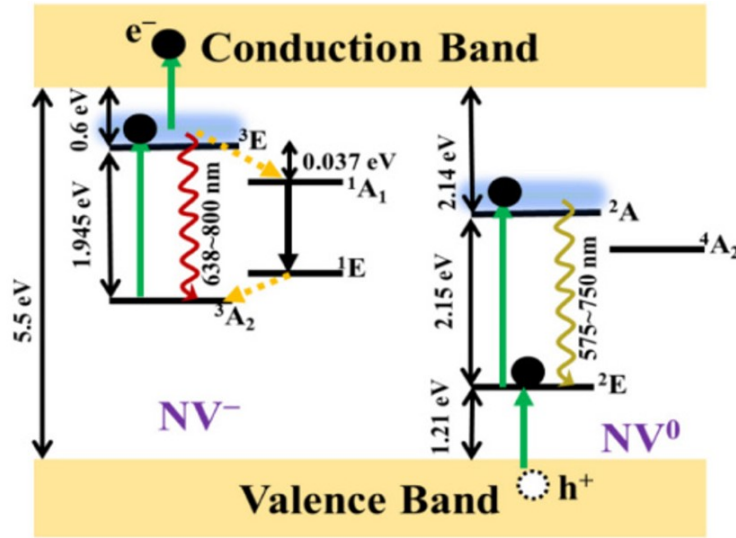
Figure 2.2 – Electronic structures of NV centers (negatively and neutrally charged). The discrete energy levels between conduction and valence bands behave like atoms and therefore these defects are sometimes termed artificial atoms. Harnessing the optical and spin properties of these defects could enable quantum applications within a solid-state platform. Reprinted from Ref. [29] with permission of OSA publishing.

which is expected to approach maturity in the near term [19], color centers promise a bright future towards complex and scaled-up quantum technologies.

2.2.2 Integrated Photonic Components

To enable efficient quantum computing with photons, a minimum set of components including single photon sources, beam splitters, phase shifters, and photo detectors [80] are needed. Up to now all these devices have been demonstrated as integrated components in diamond [3] as shown in Fig. 2.3. However, as will be explained in the following, the integration of all these components onto a single chip has not been realized due to fabrication challenges.

Single photon sources (SPSs) in diamond can be as simple as a single point defect, such as NV, SiV, and NE8 centers [40, 41, 42, 78]. For practical uses, nevertheless, individual SPSs must exhibit high indistinguishability (*e.g.,* > 0.99 for all-optical quantum repeater [78]), which requires their emission at near-identical center wavelength, and with near-identical linewidth. Due to the inhomogeneous local environment for individual SPSs embedded in a solid-state matrix, a tuning mechanism is indispensable for achieving this goal. NV centers can be tuned by Stark effect [82, 83] with integrated local electrodes, and SiV centers in a suspended nanobeam can be tuned by stress [35], as they are sensitive to electrical and strain field respectively. Such developments have, for example, facilitated the establishment of

---

[3]Phase shifter has been demonstrated on polycrystalline diamond film only [81].

6

Table 2.2 – Experimentally demonstrated applications with diamond color centers.

	Application	Color center	Reference
quantum information	single photon source	NV, SiV, NE8, *etc.*[†]	[40, 41, 42]
	quantum memories	NV, SiV	[43, 44, 45, 46]
	quantum simulation	NV	[47]
	quantum computing	NV	[48]
sensing	magnetic field	NV	[49, 50, 51, 52]
	electric field	NV	[53, 54]
	stress	NV	[55]
	pressure	NV	[56]
	temperature	NV, SiV, GeV	[57, 58, 59, 60, 61]
	gyroscope	NV	[62]
imaging	magnetic field	NV	[63, 64, 65, 66, 67]
	stress	NV	[68, 69]
	temperature	NV	[70]
	fluorescence microscopy	NV, SiV	[71, 72]
miscellaneous	navigation	NV	[73]
	radio	NV	[74]
	spectrum analyzer	NV	[75, 76]
	laser spin-cooling	NV	[77]

Note: [†] Not all color centers have been verified as single photon emitters. A more complete list can be found in review articles [20, 21, 78, 79].

entanglement between remote color centers [84], which is the essential resource required for quantum information processing.

Beam splitters are one of the most fundamental light-routing components and are straightforward to fabricate in a thin film [85], but as will be discussed in section 5.1.1, large-area thin films with satisfactory quality (*e.g.* uniform thickness, intact crystallinity, strain-free) are currently unavailable in SCD. An alternative way to carve diamond photonic structures is via angled [86] or quasi-isotropic [87] etch directly in a bulk substrate. For example, the

suspended nanobeam shown in Fig. 2.3 (a) is fabricated by angled-etch process, with its cross-section defined by the etch-angle. This feature, nevertheless, restricts the possible resulting waveguide geometries, and an efficient (low reflection loss) beam splitter is challenging to design and fabricate. By taking into consideration the fabrication restrictions, Dory [88] *et al.* demonstrated a beam splitter (Fig. 2.3 (c)) fabricated with the quasi-isotropic etch method, but the performance (power-splitting ratio, reflection loss, *etc.*) was not reported. To facilitate on-chip integration of complex photonic functionalities, further development either in the design and fabrication techniques for bulk substrate structuring, or in the manufacturing of large high-quality SCD thin films, would be required.

Phase shifting requires controllable modification of the local effective mode index in a waveguide. In silicon or III-V compound materials, this can be done by free carrier injection with integrated electrodes. In contrast, with diamond this approach is not viable given its large bandgap. Alternative tuning mechanisms are thermal and electromechanical modulation, in the former case the waveguide is locally affected by Joule heating for changing the refractive index, which potentially causes thermal crosstalk that may compromise the performance of nearby SPSs or single photon detectors (SPDs). Consequently, the most suitable solution for on-chip phase shifting is believed to be electromechanical modulation as shown in Fig. 2.3, where two waveguides are evanescently coupled, and by electromechanically controlling their separation, effective mode index change can be achieved. This approach, however, is only suitable for device fabrication based on thin film diamond, as it is extremely challenging to realize strong coupling between nearby waveguides via bulk structuring, which we further explain in Chap. 5.

SPDs directly integrated on photonics circuits have been demonstrated in various material platforms [89] by depositing thin films of superconducting materials on top of waveguides and structuring it into nanowires. An example SPD is shown in Fig. 2.3, where the SPD is made from 4.6 nm of niobium nitride. Below critical temperature and critical current, the absorption of a single photon is sufficient for breaking the superconductivity, leading to voltage pulse readable by electronics. In diamond, such devices have been fabricated by both thin film and bulk structuring [85, 90]. The high sensitivity and accuracy operation of this type of SPD requires high biased current, therefore it is of vital importance to fabricate devices with high critical current [91]. Given that the thickness of the superconductive film is on the order of few nm, successful and reliable fabrication of such devices requires the substrate surface smoothness reaching sub-nm level. A scalable process fitting this purposed will be discussed in Chap. 3.

Beyond the linear optics scheme [80], it is also of interest to realize nonlinear interactions between photons. However, since direct photon-photon interaction is extremely weak [92], light-matter interaction mediated processes are typically required to fit this purpose. Integrated resonators can strongly confine light in a small mode volume, enhancing light-matter interaction by magnitudes [93], and are therefore highly of interest for optomechanics and quantum photonics. This topic has drawn intensive efforts in the community, with photonic
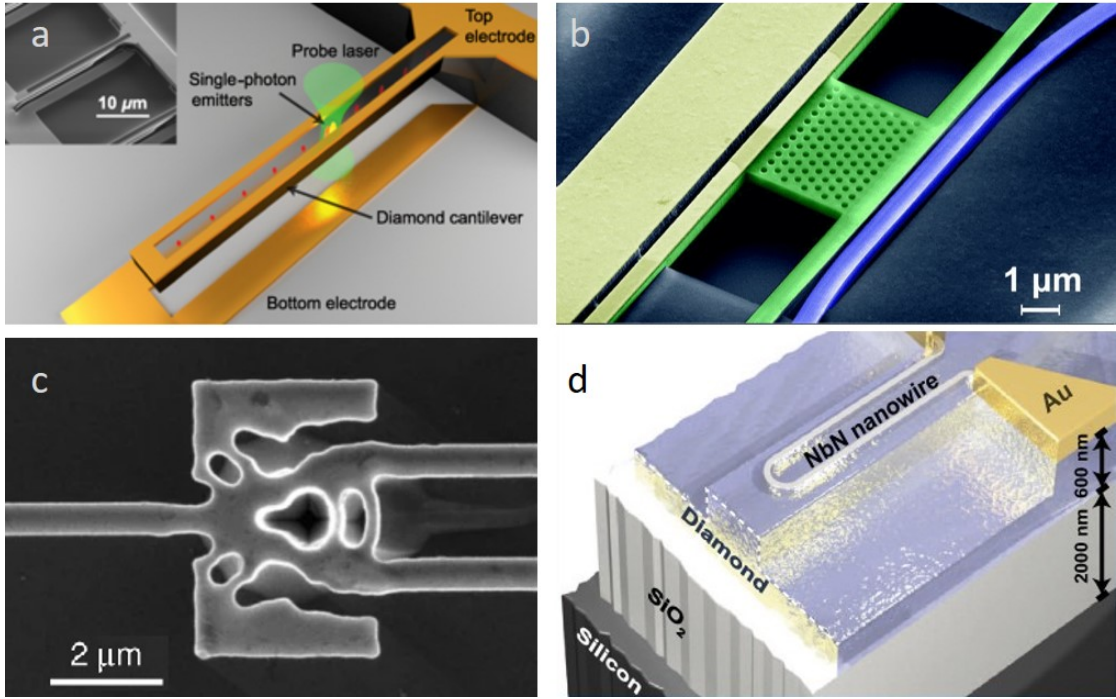
Figure 2.3 – (a) GeV single photon source tunable by strain field. Reprinted from Ref. [32] with permission of APS (the American Physical Society).(b) Electromechanical phase shifter, fabricated in polycrystalline diamond film. Reprinted from Ref. [81] with permission of AIP publishing. (c) Suspended power splitter fabricated by quasi-isotropic etch. Reprinted from Ref. [88] with permission of Springer-Nature publishing (creative commons license). (d) Superconducting nanowire single photon detector fabricated on polycrystalline diamond film. Reprinted from Ref. [85] with permission of Springer-Nature publishing (creative commons license).

crystal cavities with mode volume $\sim 0.5 \, (\lambda / n)^3$, race-track cavities with Q-factor > 100'000 having been fabricated via both thin film and bulk structuring.

In addition, the rapid development of quantum photonics has witnessed a range of devices which goes beyond the conventional concepts in photonics integrated circuits. For example, with diamond color centers, the charge state of the point defects can be tuned by surface termination or current injection, and the spin coherence can be engineered by local strain field. A comprehensive review of the performance of recently demonstrated integrated photonic devices in SCD is found in Ref. [19].

2.2.3 Quantum Applications

Despite that further technological advances are required for the on-chip integration of fully functioning quantum circuits in diamond, some quantum applications in this material plat-

form are approaching or have reached maturity, such as quantum sensing. The most prominent example is NV-center based quantum magnetometry [94], where the optical signal from NV centers in diamond respond to their magnetic environment, acting as an atomic sized sensor. Similarly, thermometry, electrometry, *etc.* have also been shown feasible with NV centers [57, 53]. In combination with atomic force microscopy, this instrument allows high-resolution imaging of various physical quantities, and has drawn considerable interest [95] in research applications. In parallel, both university spin-offs [96] and traditional high-tech companies [97] are active in pursuing diamond quantum technologies for commercializable sensing and navigation products.

On the other hand, quantum information processing tasks remain challenging to achieve at large scale. For quantum computing, preliminary successes have been reported only involving a small number of quantum bits (qubits) in diamond, such as 7-qubit GHZ state preparation, 10-qubit quantum memory, 2-qubit quantum gate with fidelity > 97%, etc [98]. A quantum memory capable of bell-state measurement was demonstrated recently with SiV centers embedded in a diamond nanobeam cavity, which has the potential to be used for building quantum repeaters for quantum internet, but the experiment employed gas-condensation technique [43] for cavity-resonance tuning, and it still remains challenging to fabricate devices with identical performance. Similarly, quantum simulation has been demonstrated feasible in proof-of-concept experiments, but further material engineering and protocol development are still required to scale up this technology [99, 100].

Beyond the above-mentioned applications, it has also been suggested to use color centers for time keeping [101] or laser cryo-refrigeration [102]. With such broad possibilities, it is of great interest to develop miniaturized and scaled-up diamond-based devices and circuits for next-generation technologies. In the next section, we will see that the challenge even begins from polishing — the first step before any subsequent processing.

3 Scalable Fine Polishing for Photonic Integration

Diamond tools were briefly mentioned in chapter one, which are made possible thanks to the ultimate mechanical hardness of this material. This very property, nevertheless, serves both a blessing and a curse, as when it makes diamond unlikely to degrade in an unwanted fashion, it also prevents us from easily shaping it in a desired way. We begin this chapter by reasoning the necessity of polishing diamond to sub-nanometer smoothness, following which a short overview of in-contact polishing is given. We will see how hardness can be a curse and why it is of much value to develop a process to achieve smooth surfaces, repeatably while at a reasonable cost, and that is what follows therefrom: the non-contact polishing technique by ion beam etching (IBP as in ion beam polishing referred to hereafter). The content of this chapter has been published partially in Diamond and Related Materials [103].

3.1 Nanoscale Roughness in Photonic Integration

Single mode waveguides are basic yet essential building blocks for photonic integrated circuits (PIC). For a slab waveguide with air-diamond-silica configuration, as shown in Fig. 3.1, the thickness of the diamond layer has to be thinner than $\sim 250\ nm$ to preclude high-order mode propagation at 637 nm (ZPL of NV^- center). When more than one mode is supported by the waveguide, interference may take place as the modes have different propagation constants. Beside that excitation of only one mode is practically not feasible, being mathematically orthogonal to each other cannot prevent multiple modes from cross-talking if, for example, there is a particle on the waveguide which causes scattering, or the slab thickness is not uniform over large area.

For a fundamental TE mode guided by a diamond slab with thickness t, Tien theory [104] predicts the scattering loss to be

$$\alpha = \frac{8\pi^2(\sigma_1^2 + \sigma_2^2)cos^3\theta}{\lambda^2 sin\theta[t + 1/p_1 + 1/p_2]},$$

(3.1)
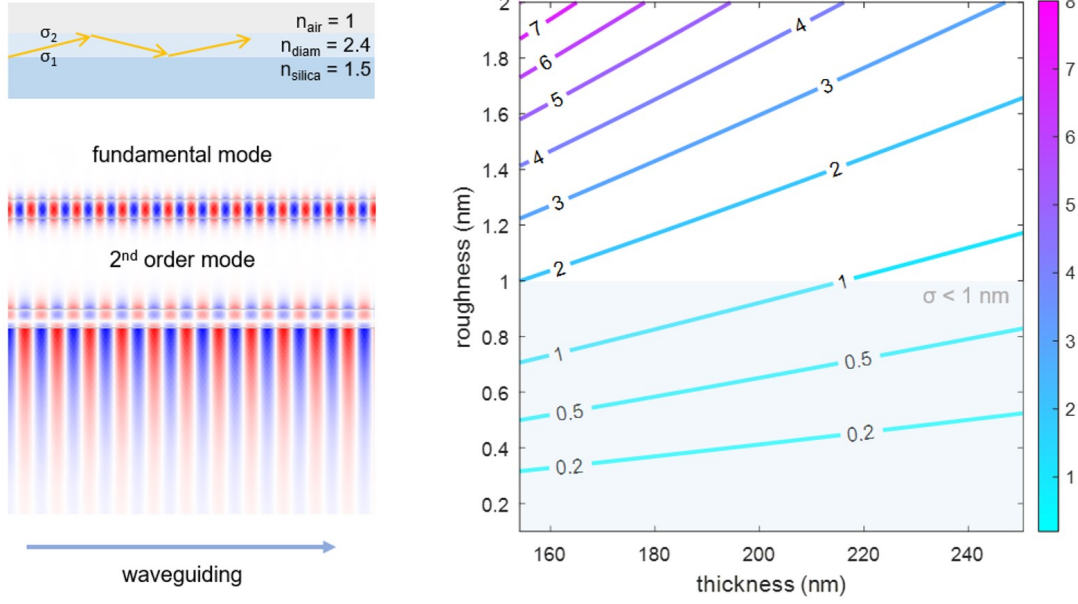
Figure 3.1 – Left: a slab waveguide of 250 nm thickness is able to guide two propagating modes at 637 nm in air-diamond-silica configuration, simulated in COMSOL software. As the slab thickness in the simulation is chosen to be close to threshold for guiding 2nd order mode, the field distribution has a long tail in the silica substrate. Right: contour plot showing the dependence of scattering loss (attenuation coefficient in cm^{-1}) for fundamental TE mode on surface roughness and slab thickness, with values on contours indicating the attenuation coefficient. We can translate α into q-factor via $Q = 2\pi n/(\alpha\lambda)$, and a scattering loss of $\alpha = 0.2\ cm^{-1}$ alone already limits the q-factor to be below 1E6, let alone other loss mechanism.

where $\sigma_{1(2)}$ is the surface roughness [1] on the interface between silica (air) and diamond, θ is the beam incidence angle within the guiding material, and both t and wave-number $p_{1(2)}$ are functions of θ,

$$p_{1(2)} = k\sqrt{n_{diam}^2 sin^2\theta - n_{silica(air)}^2}, \tag{3.2}$$

$$t = (\Phi_1 + \Phi_2)/(kn_{diam}cos\theta), \tag{3.3}$$

with $k = 2\pi/\lambda$, and

$$tan\Phi_{1(2)} = \frac{\sqrt{n_{diam}^2 sin^2\theta - n_{silica(air)}^2}}{n_{diam}cos\theta}. \tag{3.4}$$

Assuming $\sigma_1 = \sigma_2$, we plot α against slab thickness and surface roughness in Fig. 3.1. Knowing that $Q = 2\pi n/\alpha\lambda$, one can see immediately that sub-nanometer roughness is indispensable for the realization of high-quality (q-factor > 1E6) resonators for on-chip integration of narrow-

---

[1] Ra and Rq are the frequently used measures for characterizing surface roughness, with Ra being the arithmetic average of surface height deviation from mean value, and Rq the root mean square average. Throughout this text we refer to Ra roughness as the measure of surface quality.
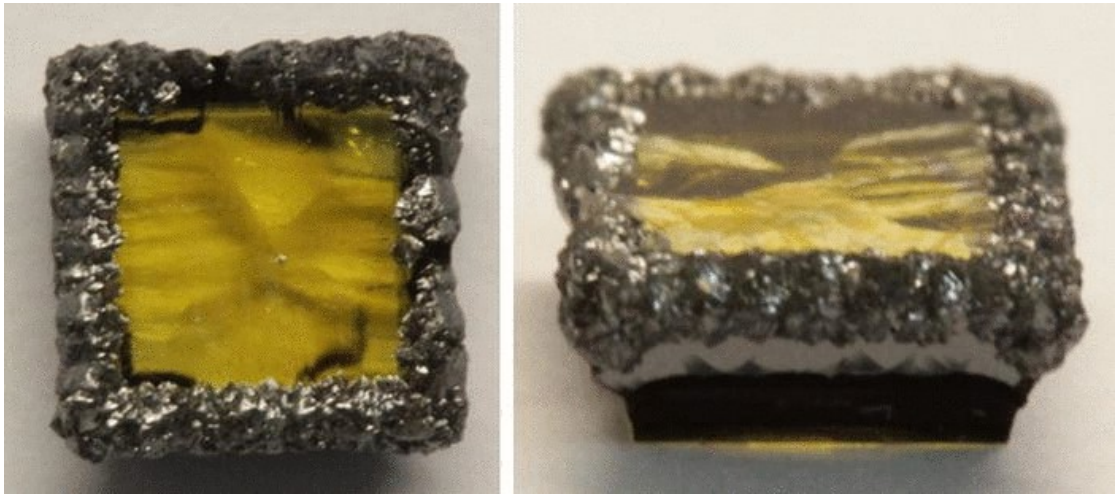
Figure 3.2 – Homoepitaxial single crystal diamond grown at 1020 °C for 19.5 hours. The yellow color is due to the HPHT (high-pressure high-temperature) seed diamond below the expitaxial layer. The polycrystalline rim needs to be removed, and the surface area in the middle needs to be flattened after laser-cutting the growth layer. Reprinted from Ref. [17], with the permission of AIP Publishing.

band filters, lasers, and frequency comb sources. In addition, with the same surface roughness, it is preferred to use a thicker (but thinner than threshold thickness for single-mode guidance) slab if lower loss is desired. This in turn requires the slab of high uniformity, otherwise a gradually increasing thickness causes fundamental mode to couple to higher-order mode, introducing unwanted complexity in signal due to interference.

In a real device the waveguide is usually strip- or rib-shaped, and the roughness on both top/bottom surfaces and sidewalls matters. In the top-down approach for the microfabrication of optical waveguides, the sidewall roughness is closely related to the etching process (*e.g.* Fig. 5.7), a topic we further explore in Chap 5. Here in the following we dive into the polishing techniques that are responsible for top/bottom surface roughness.

3.2 Polishing Induced Damage in Diamond

As-grown diamond substrates commonly feature a polycrystalline rim and non-flat surface, as shown in Fig. 3.2 for instance. From a raw stone to a substrate shipped for further fabrication, diamond has to undergo a series of processing: cutting, grinding, lapping, polishing. In fact, even in the last step there are coarse, fine and ultra-fine polishing sub-steps, resulting in different grades of surface finishing. In Fig. 3.3 we show a commercially available SCD substrate (general grade) purchased from Element Six, whose surface under an optical microscope shows abundant black spots, which are micro-sized pits induced by mechanical polishing, their details better observable under SEM (scanning electron microscopy).
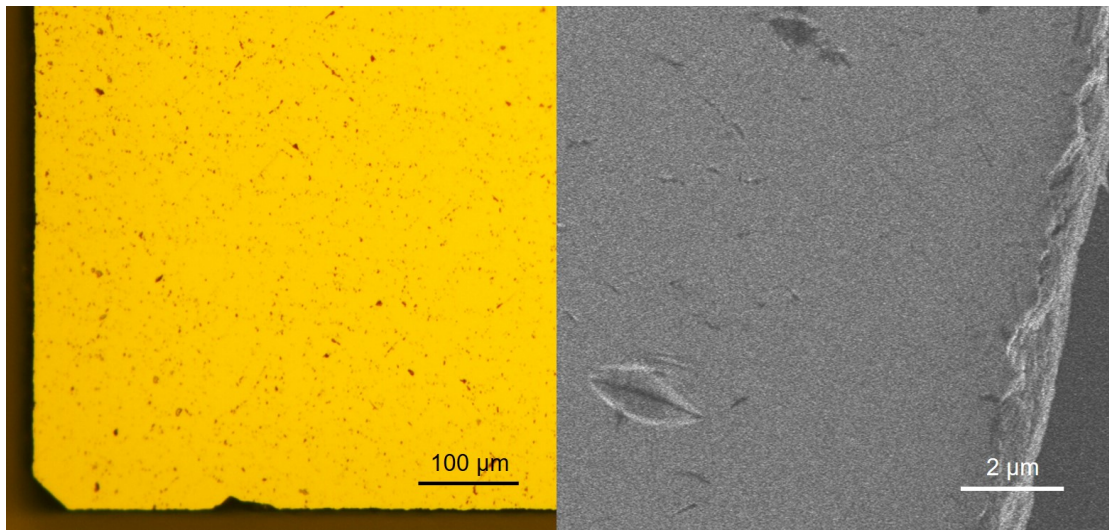
Figure 3.3 – Surface of commercially available SCD substrate under optical microscope (left) and SEM (right). The defected region observed under SEM corresponds to the black dots seen under optical microscope.

With AFM (atomic force microscopy) we can characterize the polishing damage quantitatively. The measured surface roughness for a sample looking like Fig. 3.4 is about 0.7 nm in the flat areas, and not surprisingly if we include the defected region it increases drastically (4.6 nm). We have measured individual scratches/pits featuring depths of up to 330 nm on as-received SCD substrates, which prohibits large-scale optoelectronic applications.

The challenge in polishing diamond lies fundamentally in the fact that it is the hardest and most brittle material. Mechanical polishing causes not only defects on the surface but also extended subsurface damage up to several microns deep [105, 106]. A gentle polishing carefully carried out along the <100> directions is able to help counter these problems, but this manual process is slow and not applicable to very thin or large plates as the pressure imposed onto the substrate is still high enough to cause bending and fracture. Consequently, a few new techniques have been developed to provide high-quality surface finishing of SCD substrates without severe damage, including but not limited to UV-assisted polishing [107], plasma-assisted polishing [108, 109], iron-based chemical mechanical polishing [110], *etc.* In spite of their success, they either require specifically developed equipment or very long processing time, not to mention the limitations commonly shared by in-contact polishing methods such as risk of fracture when thin plates are polished, and the low-tolerance in processing multiple samples with different heights.

To facilitate scalable SCD surface processing, we develop a non-contact polishing protocol leveraging ion beam etching (IBE), which is commonly used and readily available in semiconductor industry. The proposed method is non-contact, therefore capable of polishing large and thin substrates, or parallel processing of many plates regardless of their height variation.

14
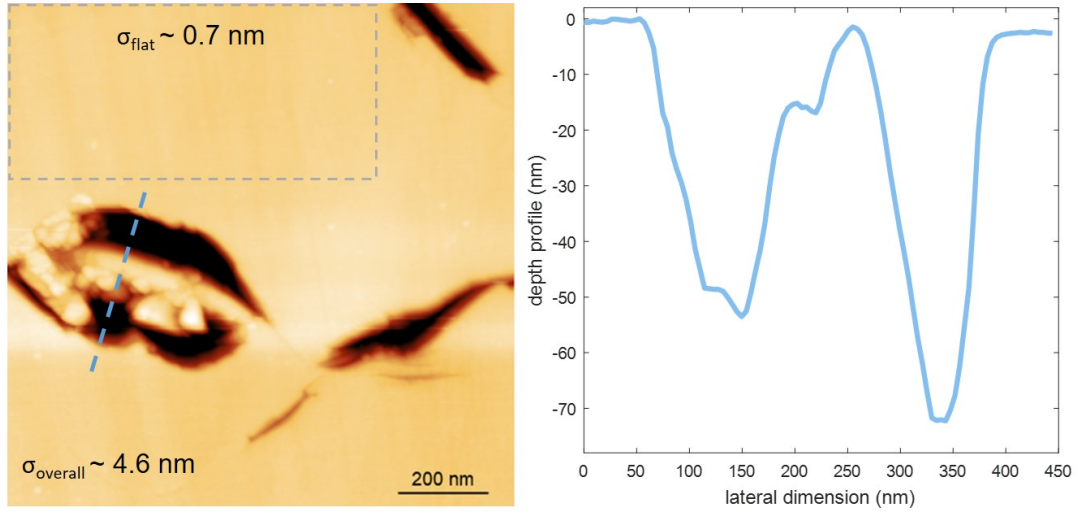
Figure 3.4 – AFM imaging of a commercially available as-received diamond substrate. The plot on the right corresponds to the depth profile along the dashed blue line in the left panel. If one looks carefully, some faint polishing lines can also be observed which typically exist after mechanical polishing. The local roughness of the flat (defect-free) area is below 1 nm but when the surface damage is included the roughness goes worse to several nanometers.

3.3   Ion Beam Polishing

Ion beam etching (IBE) has been investigated for polishing purposes for decades. For example, Ref. [111] employed near-grazing-angle IBE to polish a polycrystalline diamond film from 3 μm roughness to 0.5 μm, where geometrical shading was at work. In Ref. [112], protrusion-like roughness was flattened out due to angle-dependent sputtering yield with IBE carried out at normal incidence. Down to the nanoscale, it was also demonstrated that roughness on the order of 0.1 nm is achievable given an original surface with roughness on the order of 1 nm [113]. In each case the working mechanism is different and the method is suitable for certain surface characteristics, with specific processing conditions. For a substrate shown in Fig. 3.3, however, none of these methods provides a rapid and high-quality finishing, as a grazing angle condition would rapidly enlarge the surface defect and a small incidence angle could not remove this kind of damage. In the following we propose and demonstrate a new protocol using IBE that is able to fine-finish a mechanically polished diamond plates, after which we also note with two examples the versatility of this technique.

3.3.1   Angle-Dependency of Ion Sputtering Yield

IBE is a well-established process in which inert gas molecules are ionized and subsequently driven towards the material surface as depicted in Fig. 3.5, with uniform beam profile and defined acceleration energy. The material removal mechanism is dominated by physical bombardment, therefore IBE is well suited for processing various materials [115] regardless of
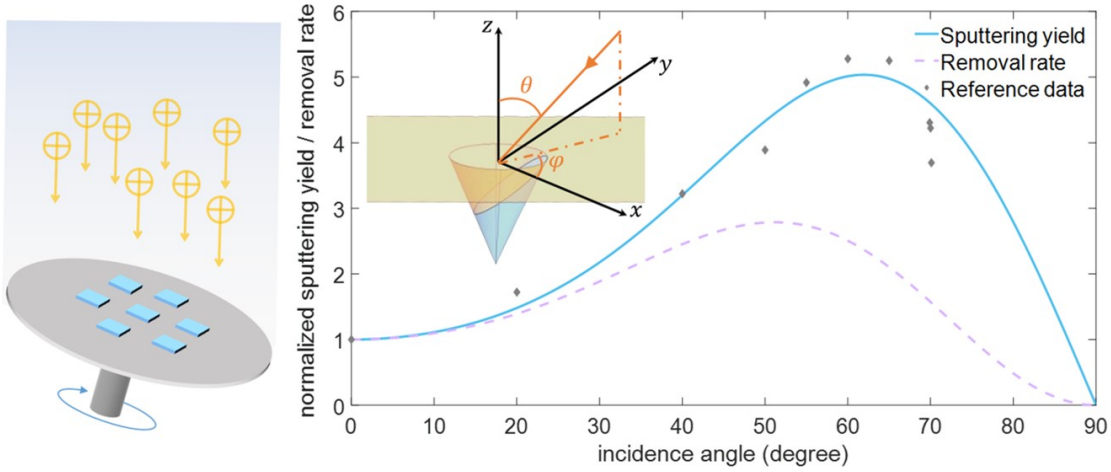
Figure 3.5 – Left: schematic of IBE process, where the substrate can be inclined and rotated, with arrows indicating the ion impingement. Multiple samples can be processed simultaneously regardless of their height difference. Right: angle-dependency of normalized sputtering yield/removal rate for Ar$^+$ ion with 750 eV acceleration energy, where the inset shows the local coordinate of a polishing pit. The reference data is taken from Ref. [114] and the sputtering yield is a fitting of this data based on Eq. 3.5. The etch-rate is normalized to that at normal incidence.

their chemistry.

The etch-rate in this process is determined by ion sputtering yield and ion flux. While the latter can be tuned by the apparatus, the former is physics-related and depends on the nature of the target material/the ion species, and the acceleration energy of ions. The sputtering yield, defined as atoms removed by per incident ion, has an incidence-angle dependent behavior [116] that is ubiquitous for many materials. For example, the sputtering yield for 750 eV Ar$^+$ ion beam impinging onto SCD (100) surface at incidence angle (θ) of 60° is about five times of that at $\theta = 0°$. In general, the angle dependency can be modeled by [116]

$$Y(E, \theta) \propto \frac{E}{UN(2\pi A)^{0.5}} \exp(-\frac{cos^2\theta a^2}{2A}) \tag{3.5}$$

where $A = cos^2\theta \alpha^2 + sin^2\theta \beta^2$, with $\alpha(\beta)$ being the energy range straggling along longitudinal(lateral) direction, U the surface binding energy, E the ion acceleration energy, N the atomic density, and a the projected energy range. Although originally this formula was proposed to model the sputtering of amorphous and polycrystalline materials, very good agreement between empirical data for single crystalline materials and the theory was observed [114], which is consistent with the fact that a thin amorphized surface layer is developed under ion bombardment for crystalline materials. Besides, molecular dynamics (MD) simulation also confirmed good over-all agreement with Eq. 3.5 despite of local maxima/minima [117] which is believed to originate from the crystallographic nature, but has negligible impact to

16
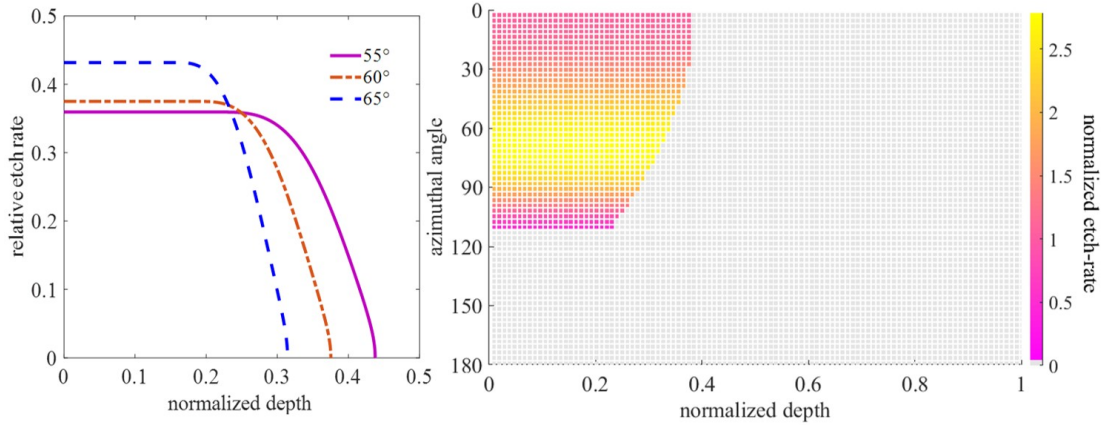
Figure 3.6 – Left: selectivity (etch-rate ratio between sidewall and top-surface) dependence on ion incidence angle, with shallow cut-off depth and small relative etch-rate preferred for selective removal of the planary top-surface thus a better finishing. Right: normalized etch-rate on a generatrix of the polishing pit, and its dependency on depth and azimuthal angle, with $\chi = 0.4$ and $\theta = 60°$ used for simulation. The cut-off angle and depth suggest that during sample rotation, a generatrix is not always exposed to ion beam and the etch-rate not only is depth-dependent but also vanishes beyond cut-off.

the process described below.

3.3.2   Non-Contact Polishing via IBE: Theory

The essence of polishing is to selectively remove materials above a certain level so that the remaining substrate exhibits a flat and smooth surface. With this in mind, we list the three working mechanisms [2] that make ion beam polishing possible, supposing the pit in Fig. 3.5 is the surface defect we would like to remove:

(i) geometrical shading. When the sample is etched by ion beam at any oblique angle, only parts of the sidewall of the pits are etched, resulting in selective material removal of the close-to-surface layer.

(ii) dynamic averaging. As the substrate rotates, the top planary surface is constantly etched by the ion beam, but inside a pit, only part of the sidewall is etched at any given time (provided that the pit is steep enough). Rotation effectively introduces selective material removal of the subsurface layer.

(iii) angle dependent etch-rate. As we can see in Fig. 3.5, the etch rate peaks at certain angle given specific etching conditions. By choosing ion incidence angle appropriately, the selectivity can be optimized.

---

[2] In the next chapter we will see that during IBE there are more things happening such as mass-redistribution [118] at the atomic scale than just simple geometrical or macroscopic arguments, but we will not be bothered to develop an all-inclusive theory as long as a simple picture is satisfactory in terms of explaining the observations, as the great mind George Box many times wrote: all models are wrong, but some are useful.
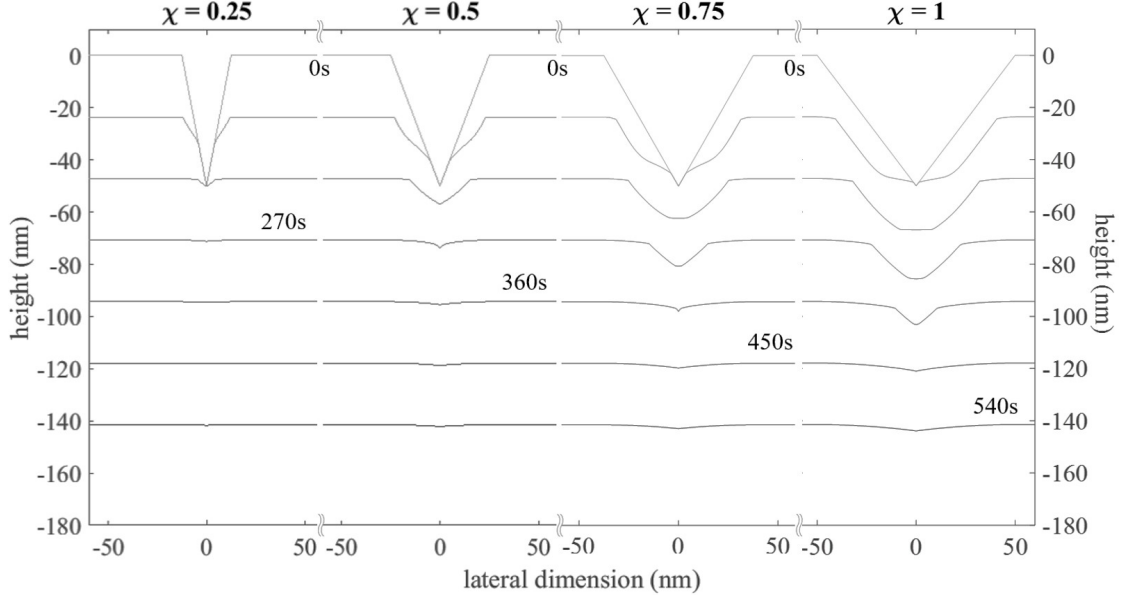
Figure 3.7 – Simulation of polishing process for different χ, where the pit depth is kept the same and the base radius is varied. The surface profile is drawn for every 90 seconds spacing. A pit with smaller χ requires shorter time to become flat, while the final finishing quality is not much different. θ is set to 60° for all simulations. The timescale is calibrated according to experimentally measured material removal rate $\sim$ 16 nm/min on the top planary surface.

Since these three mechanisms work together in an intertwined way, we perform numerical simulation to get a better, quantitative understanding of the process. The simulation was set up according to real-world etch rate we measured for diamond being etched by Ar^+ ion with acceleration energy 700 eV and current 1.1 mA in a Veeco Nexus IBE350 at EPFL-CMi. To facilitate the explanation of the working mechanism, we clarify some definitions: the surface pit is simplified as an inverse cone, as shown in Fig. 3.5, where φ and θ are the azimuthal and polar angle of the incident ion beam, respectively. We define $\chi \equiv r/h$ where r is the base radius of the cone and h is the height (depth), as a measure of pitting steepness. Due to symmetry we will only discuss the etching effect on the generatrix of the cone. Since the absolute etch rate only determines the processing duration and is irrelevant of the polishing quality in the limit of slow-etch (which is the case here as diamond is etched very slowly with the experimental conditions we employed), the etch-rate is normalized in the following discussion to that at normal incidence condition.

During IBE the substrate keeps rotating (varying φ) at a fixed speed, and the inclination is kept the same (constant θ). The top planar surface is thus etched at a fixed rate, while the sidewall of the pit experiences local ion incidence angle variation depending on φ. Assuming $\theta = 60°$ and $\chi = 0.4$, we plot in Fig. 3.6 the etch-rate on the generatrix against azimuthal rotation and depth based on Eq. 3.5 (fitting parameters used here are $\alpha = 42.15$, $\beta = 50.37$, and $a = 103.5$), where the maximum depth is normalized to unity without loss of generality. In slow-etch

limit, the pit geometry can be assumed to be invariant during one rotation cycle. The cut-off depth and cut-off angle clearly suggest that while the sample is rotated, a certain region on the sidewall is etched intermittently (cut-off azimuthal angle), and the etch-rate on the sidewall is depth dependent and vanishes below cut-off depth, giving rise to selective removal of material closer to the top surface. Therefore ion beam is able to polish substrates like those shown in Fig. 3.3. Note that the optimal θ can be chosen based on simulation as explained in Fig. 3.6. As χ changes, which corresponds to non-identical damages (scratches and pits) on a mechanically polished diamond surface, the finishing quality and speed would be inevitably different. Nevertheless, as illustrated in Fig. 3.7, with the same ion incidence angle, pits with various sharpness all show a good surface finishing by the end. This simulated result is further confirmed by experiments as detailed in the following section.

3.3.3 Non-Contact Polishing via IBE: Experiment

In order to observe the time evolution of the surface characteristics quantitatively, we first fabricate a 10×10 array of square-shaped plateaus on the mechanically polished substrate, each with 200 nm height and 10 μm side-length. The process flow is as follows: after cleaning of the as-received sample with piranha solution, a thin film of SiO$_2$ is sputtered onto diamond to protect the surface features, which also works as a hard mask for subsequent etching; standard photo-lithography is used to pattern and develop spin-coated photoresist, and the patterns are transferred to diamond with 2 steps of plasma etching (first to the oxide layer via fluorine chemistry, then to the diamond substrate via oxygen chemistry); finally the oxide is completely removed in BHF and the sample is cleaned with piranha once again. SEM examination revealed at least two deep scratches on each plateau.

The substrate is then fed to an IBE tool (Veeco Nexus IBE350) operating at 700 eV acceleration energy and 1.1 mA current, for 28 minutes of etching by Ar$^+$ ions with sample rotation at 10 rpm, inclined at 60°. The time evolution of individual scratches were tracked by SEM before and after 4, 12, 20 minutes of IBE. An example is shown in Fig. 3.8, and AFM measurement was carried out to confirm the trench depth reduction from 108 nm to 3 nm for this scratch in 28 minutes. Approximately 500 nm diamond layer was removed during polishing.

As illustrated by Fig. 3.7, the polishing mechanism in our method needs to etch deeper than the actual depth of the defect to planarize the surface. It is nonetheless still of similar or much faster polishing speed compared to other fine finishing techniques (for example, Ref. [108, 122] cost about 1 hour and Ref. [123] 10 hours to finish the process). Besides, the process can be accelerated linearly by increasing the ion flux. By comparing our experiment conditions with Ref. [124], the effective pressure exerted onto diamond substrate due to Ar$^+$ ions can be estimated to be on the order of 1 Pa, six magnitudes smaller than that in Ref. [123, 122]. The mildness of our method is of particular interest for avoiding microns deep of subsurface damage. We note that a thin layer of amorphous carbon [125] will be present on the very surface after IBE process, which is estimated to be less than 5 nm by TRIM simulation [126]
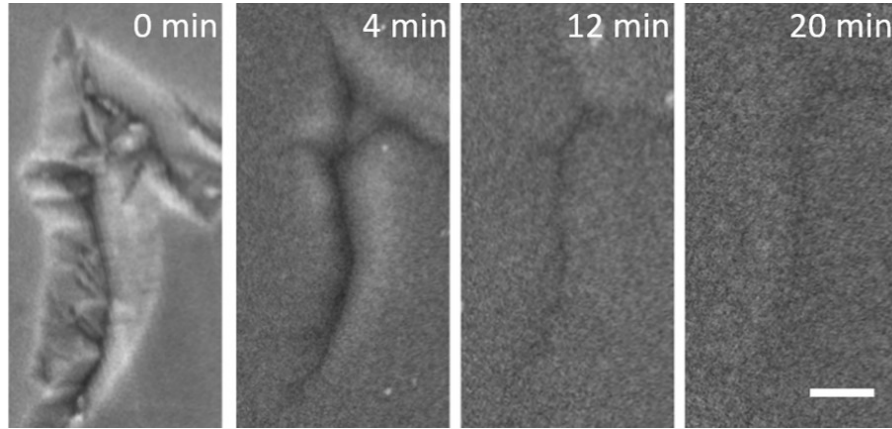
Figure 3.8 – SEM observation of the time evolution of a single scratch during polishing (scalebar 100 nm). AFM measurement confirmed the trench depth was reduced from 108 nm to 8 nm in 20 min and further to 3 nm after another 8 min (not shown here). Nano-dot like structures appeared after polishing, which can be easily removed with normal incidence IBE [113]. Their origin will be discussed in the next chapter.

for 700 eV Ar$^+$ ions. This ion beam induced amorphized layer can be readily removed by annealing in oxygen-containing atmosphere [127] though.

Nano-sized roughening can be observed in Fig. 3.8, which is the topic we explore in the next chapter. Here for the purpose of polishing, we can simply remove the roughness by normal incidence ion beam etching [113], resulting in a surface with sub-nanometer smoothness. In
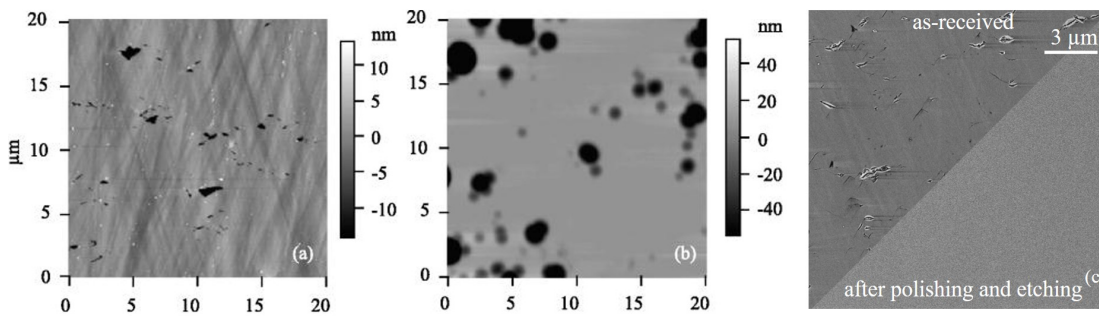
Figure 3.9 – Left two pictures show AFM characterization of a diamond surface without fine polishing before and after plasma etching [119]. The scratches originally present on the surface are enlarged due to plasma etching. On the right we show SEM pictures of the as-received substrate and a diamond surface after polishing with the above-mentioned approach and subsequent oxygen plasma etching. The challenge arising from plasma-etching a damaged surface is ubiquitous and can be noticed in many reports such as Ref. [120, 121], highlighting our polishing technique as an important process for scalable fabrication of diamond devices. (a) and (b) are reprinted from Ref. [119], with the permission of AIP Publishing.
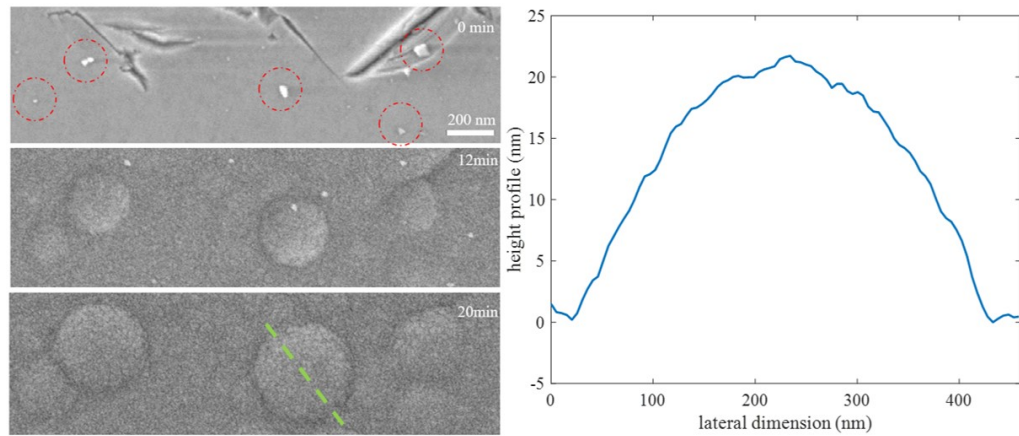
Figure 3.10 – Time evolution of diamond surface due to initial presence of nanodiamond abrasives. On the right we show AFM measurement along the dashed line in the left panel. The height of this bump changed little (from 22 nm to 19 nm) in 20 min, consistent with the picture we described in the preceding section.

our process only a few hundred of nanometers of diamond needs to be removed, shallower than the extent of sub-surface damage caused by mechanical polishing. The ion beam polished surface can be further etched by reactive ions to completely remove the damaged sub-surface layer, without introducing defects that have been frequently observed in literature as shown in Fig. 3.9. Thin films fabricated from mechanical polishing (c.f. Fig. 5.1) are usually of the thickness about $5 – 20\ \mu m$ and our process can also be applied to treat them safely.
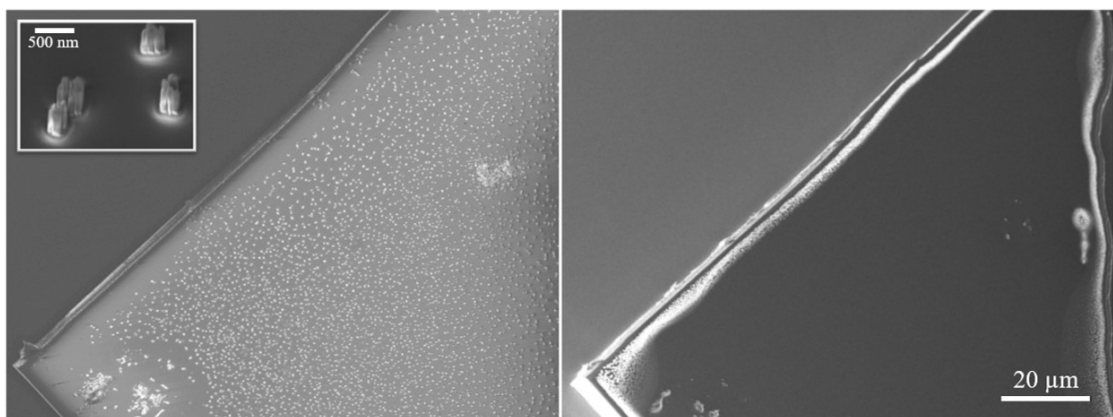
Figure 3.11 – Polishing of a diamond substrate initially with abundant nanopillars. Image courtesy of Dr. Marcell Kiss.

3.4   Versatility of IBE

The polishing method demonstrated above leverages the fact that the etch-rate for the planar top surface is higher than that for the side-wall of the pits, if the ion incidence angle is chosen properly. When we have protrusion-like defects on the surface, this fact remains true and would lead to enlargement of initial structures. In a region of the diamond substrate shown in Fig. 3.8, residual nanodiamond abrasives remained after mechanical polishing were identified and their time evolution was tracked by SEM as well. We show in Fig. 3.10 that they grew much larger in diameter. AFM measurement confirmed that the height changed little which is consistent with the model we described in the preceding section. This observation suggests that IBE can also be employed for fabricating 3D microstructures such as microlens array [128, 129].

We also present another example of IBE polishing, this time the initial surface has abundant nanopillars, shown in Fig. 3.11. This kind of surface is frequently found after plasma etching due to redeposition of mask materials and micro-masking effects [130]. IBE processing with ion incidence angle ~ 25° for 40 min was able to make the surface smooth again. The angle was chosen as such so that the side-wall is etched faster and the nanopillars quickly shrink in diameter.

4 Ion Beam Induced Self-Organization on Diamond Surfaces

The spontaneous formation of regular nanostructures is a fascinating topic that has attracted wide interest from both fundamental science and engineering communities. The potential to leverage these phenomena in a controllable way could eventually lead to scalable and affordable fabrication of devices at nano scale. The unexpected observation of nanodots on diamond inspired us to further explore their origin, and potential ways of harnessing this phenomenon for nanofabrication. In fact, the self-organization on material surfaces during ion beam etching has been observed decades ago. On diamond surfaces, nonetheless, it has not been extensively studied, and is rarely reported in the literature in the low-energy regime. In this chapter we present further experimental evidence on this topic, which potentially can lead to the establishment of a maskless nanofabrication method, and contribute to the continuing efforts in refining the theoretical understanding of this process [131]. In the following we first show the time and incidence-angle dependent observation of self-organized nanostructures, after which a qualitative understanding of the process is addressed with numerical simulation. The structured surface was then applied for templated solid-state dewetting, resulting in clear morphological control of dewetted gold nanoparticles, which not only is interesting for plasmonics studies by itself, but also suggests a potential approach, with the metal nanostructures serving as the hardmask during diamond etching, for scalable processing of diamond at the nano scale.

4.1 Self-Organized Diamond Surfaces by IBE

One can notice in both Fig. 3.8 and Fig. 3.10 that nano-sized irregularities exist on diamond after IBE. A clearer inspection of these features is shown in Fig. 4.1, confirming dynamic evolution of the nanodots with prolonged IBE treatment. In fact, the nanodots formation is a special case of self-organized surface patterns when IBE is carried out with sample rotation. In the case that ion beam reaches the diamond surface from a fixed direction, nanoripples form. Early observation of this phenomenon on diamond was reported by a few groups [132, 133, 134, 135] with a relatively high ion acceleration energy (from a few keV to 100 keV), and more recently it has been discovered also for diamond after ion beam treatment below 1
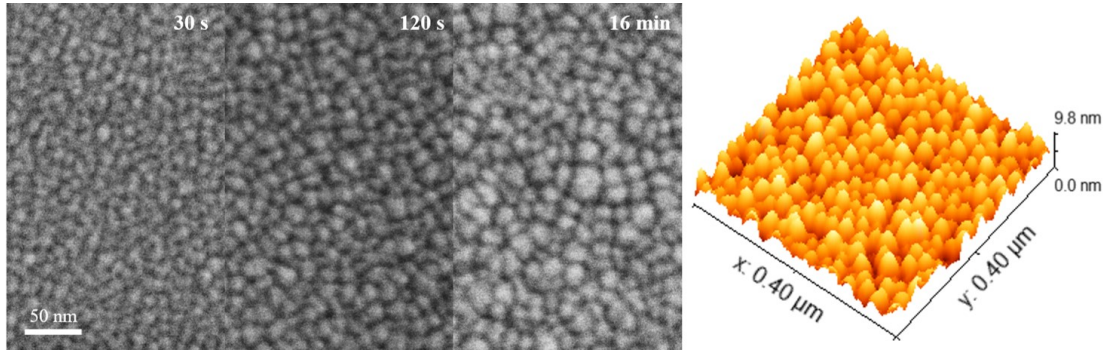
Figure 4.1 – Time evolution of nanodots formation under IBE with Ar$^+$ ions accelerated at 700 eV, ion incidence angle of 70°, and sample rotation at 10 rpm, recorded after 30s, 120s, and 16min of treatment. On the right is an AFM measurement of diamond surface after 4 min of treatment, resulting in nanodots with varying height from 1 nm to 4 nm.

keV [113, 136, 137]. With low acceleration energy, nanoripples with periodicity below 20 nm can appear, but very few data is available in the literature. Experimental observations with varying ion incidence angle and processing time are presented in this section, along with an attempt to qualitatively explain the phenomena.

4.1.1 Experimental Observations

In all experiments we used IBE with 700 eV Ar$^+$ ion. In Fig. 4.2 we show diamond surface treated at 70° ion incidence angle for prolonged time. Coarsening of ripples and growth in
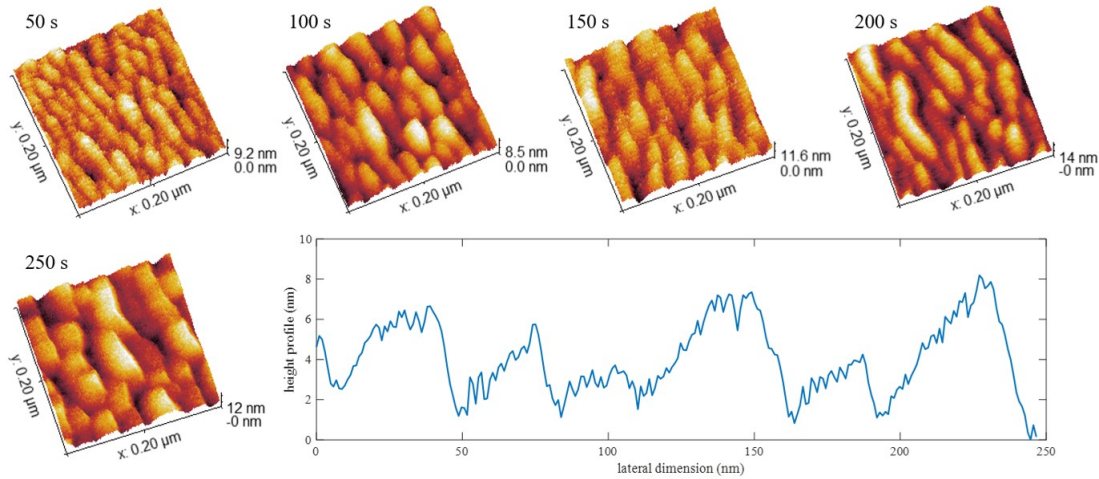
Figure 4.2 – Time evolution of nanoripples on diamond surface treated by Ar$^+$ at 70° and 700 eV. Prolonged treatment is accompanied with pattern coarsening, and in the long-time limit terraced ripples were observed, similar to that reported in [138].
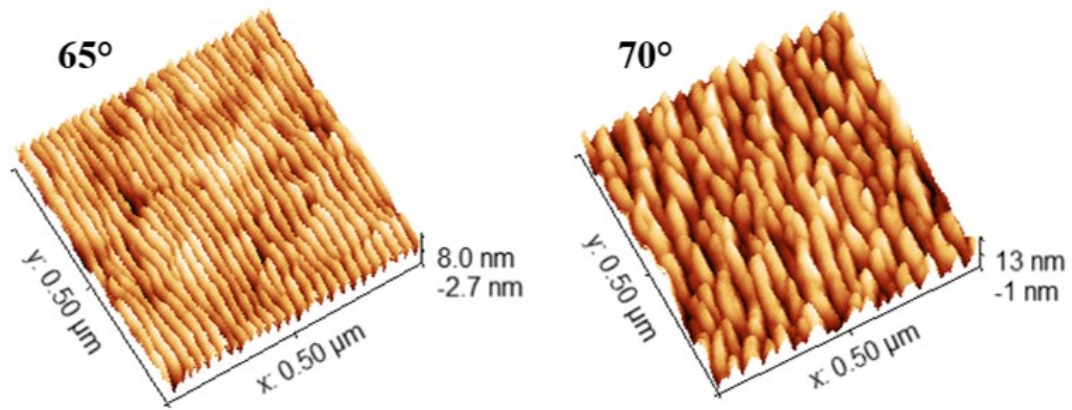
Figure 4.3 – We observed ripple formation for ion incidence from 55° to 70°. While below 65° the ripples look better ordered (only the measurement at 65° is shown as they have the same visual characteristics, see Fig. 4.4 for a quantitative comparison), they appear less regular and a tendency towards nanodots becomes clear with the angle approaching 70°. For all samples the ion dose was 1.28E18 ions/cm^2.
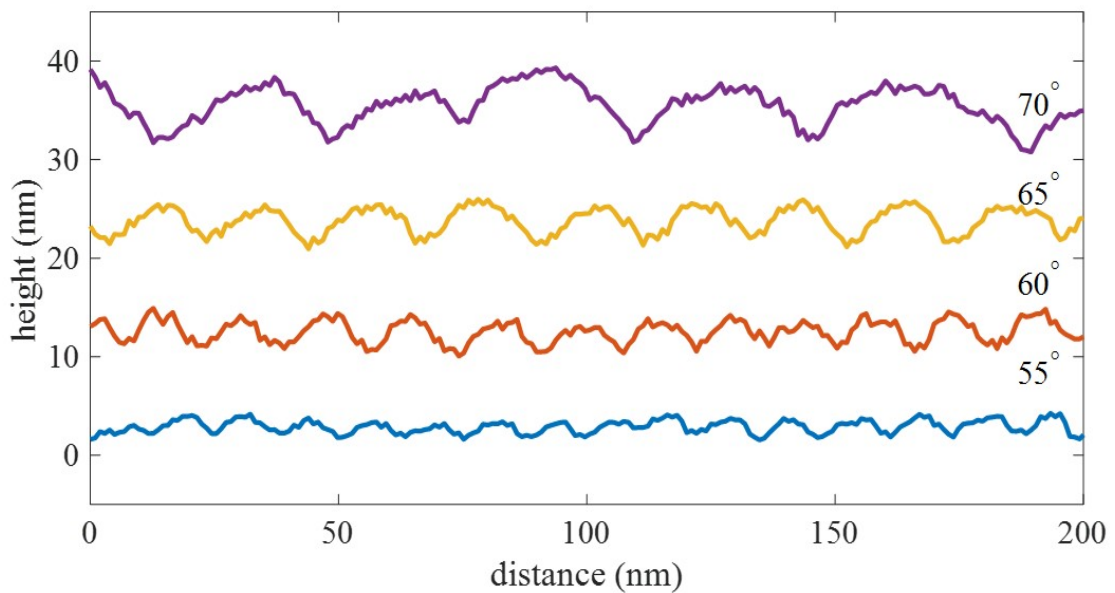
Figure 4.4 – Crossline height profiles for quantitative comparison between nanoripples created at different ion incidence angle. Both the wavelength of the ripple and their amplitude grows with the angles. Below 65° long ripples can be observed and a well-defined period can be measured from the crossline profile, while approaching 70° the long-range order disappears, therefore the crossline profile looks less regular. The profiles are offset by 10 *nm* from each other for visual convenience.

ripple amplitude were observed, along with terraced ripple formation in the long-time limit. In Fig. 4.3 and 4.4 we observed ordered ripple formation with angle incidence from 55° to 65°, but with different ripple wavelength and amplitude. As the angle increases further, the ripples become less regular, and long ripples as can be observed for lower ion incidence angle no longer exist.

4.1.2 Modeling with adKS Equation

The first report of self-organized nanoripples on a glass surface after ion beam treatment dates back to 1962 [139, 140]. With the advancement in microscopy, similar observations were made on metallic and compound materials through the 1970s and 1980s [141, 142, 143]. Since then theoretical frameworks for understanding these phenomena have been under active development for decades, from investigating the atomic scale motions by molecular dynamics simulation [144] at very short time-scale, to predicting long-term and large-scale results with continuous models described by partial differential equations (PDEs) [131, 145]. A crater function approach [146] that combines the advantages of both has also been investigated, but it has been proven computationally far more expensive than initially thought [147]. As a result, the most prevailing theoretical tools for predicting these dynamics at a reasonable spatiotemporal scale remain to be the continuous models described by PDEs.

In spite of the continuous progress made in this field since the Bradley–Harper theory postulated in 1988 [148], the complex nature of this process makes it extremely challenging to build an accurate predictive model [131], and among the various approaches developed, each has its advantages and limitations [145]. Here we employ anisotropic damped Kuramoto–Sivashinsky (adKS) equations for simulating the process, as it is both (relatively) simple and generalizable [149], aiming at providing a qualitative understanding of what is happening.

The adKS equation, in its scaled and simplified form, reads

$$\partial_t h = -(\gamma + \partial_x^2 + \alpha \partial_y^2 + \Delta^2)h + (\partial_x h)^2 + \beta(\partial_y h)^2 + \eta, \tag{4.1}$$

where $h \equiv h(\boldsymbol{r} \equiv x \cdot \hat{e}_x + y \cdot \hat{e}_y, t)$ represents the surface profile. To understand the meaning of each term, however, we have to take a look at the first PDE model built by Bradley and Harper [148].

A qualitative explanation of surface instability (spontaneous amplification of roughness) under IBE can be understood with Fig. 4.5, where on the left we show the simulated energy loss to diamond from 700 eV incident Ar^+ ions, which resembles a Gaussian distribution centered at $\sim 1.5\ nm$ (this value is referred to as penetration depth a hereafter and is indicated in Fig. 4.5). On the right, it can be seen that the distance between surface point A and energy deposition centers B is shorter than that between A* and B* due to the local curvature, therefore the carbon atoms at point A is sputtered faster, leading to any initial roughness being amplified. We further observe that the radius curvature of the ripples as seen in Fig. 4.4 is much larger
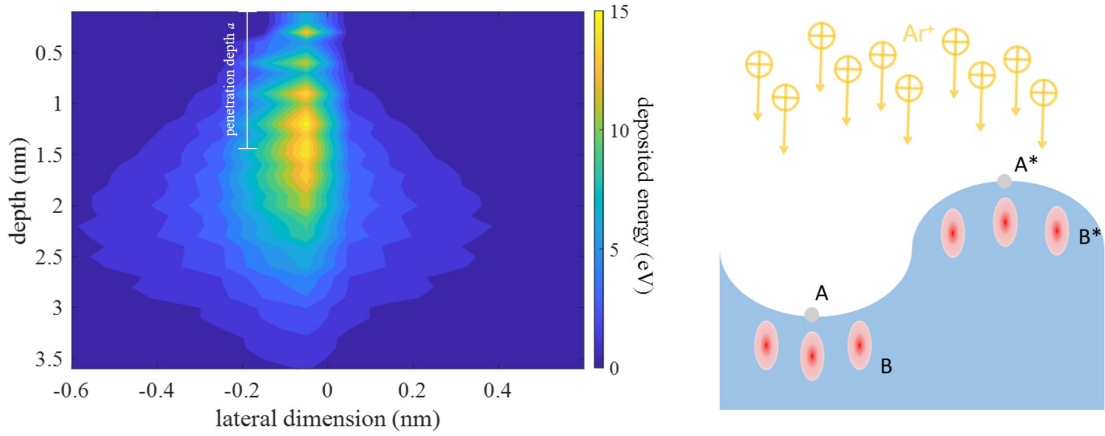
Figure 4.5 – Left: SRIM simulation of 700 eV Ar$^+$ ion into diamond where the distribution of deposited energy resembles a Gaussian centered at penetration depth a. Right: Sigmund theory for surface instability explains how an initially near-flat surface develops roughness (see main text for details).

than a. In this limit, *i.e.*, $R_{x(y)} >> a$, with $R_{x(y)}$ indicating radius curvature along x(y) direction, Bradley and Harper derived the temporal evolution of surface height to be

$$\partial_t h = -v(\varphi, R_x, R_y)\sqrt{1 + (\nabla h)^2},\qquad(4.2)$$

where φ is the angle between the ion incidence direction and the local surface normal, with the x-axis chosen to be along the projected direction of the ion beam. The r.h.s of Eq. 4.2 can be expanded in terms of spatial derivatives of h,

$$\partial_t h = -v_0 + \Gamma\partial_x h + v_x\partial_x^2 h + v_y\partial_y^2 h,\qquad(4.3)$$

with v_0 accounting for the etch rate of the global surface, Γ for the lateral movement of surface patterns, and $v_{x(y)}$ for the surface instability. Further, they incorporated a diffusion mechanism leading to

$$\partial_t h = -v_0 + \Gamma\partial_x h + v_x\partial_x^2 h + v_y\partial_y^2 h - K\Delta^2 h,\qquad(4.4)$$

where K is the relaxation rate due to thermally activated surface self-diffusion.

In 2000, the BH model was further developed [150] by taking into consideration the lowest-order nonlinear terms when expanding the r.h.s. of Eq. 4.2, giving

$$\partial_t h = -v_0 + \Gamma\partial_x h + (v_x\partial_x^2 + v_y\partial_y^2)h - K\Delta^2 h + \frac{\varsigma}{2}(\partial_x h)^2 + \frac{\varsigma}{2}(\partial_y h)^2 + \eta,\qquad(4.5)$$

with the additional noise term η accounting for the stochastic arrival of ions. Note that all coefficients except K in the equation are derived [145] to be functions of variables that can
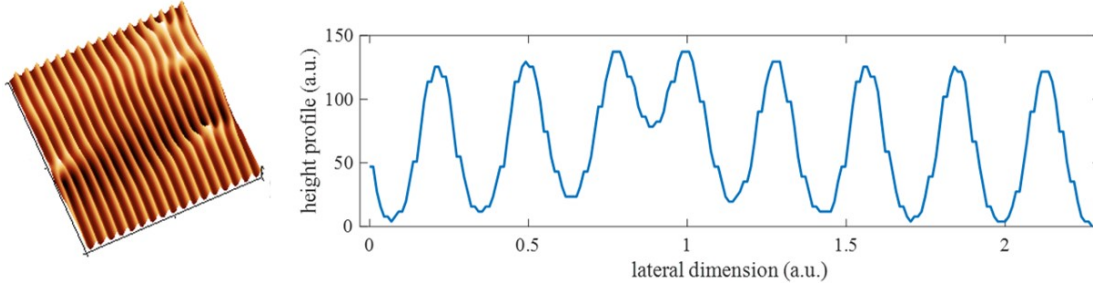
Figure 4.6 – Numerical integration of Eq. 4.1. The surface profile and crossline characteristics resemble the observation in experiments. Quantitative agreement was not found though. Numerical setup: dt = 0.002, dx = 0.5, grid size 400 × 400.

be extracted from Monte Carlo simulation. Eq. 4.5 is an anisotropic and noisy variant of Kuramoto–Sivashinsky (KS) equation [151, 152].

Shortly, following the observation of regular hexagonal patterns on gallium antimonide surface [153], Facsko *et al.* [154] introduced an *ad hoc* term with χ as a phenomenological parameter, its value set arbitrarily [1], to account for redeposition of materials, leading to

$$\partial_t h = -v_0 - \chi(h - \bar{h}) + \Gamma \partial_x h + (v_x \partial_x^2 + v_y \partial_y^2)h - K\Delta^2 h + \frac{\varsigma}{2}(\partial_x h)^2 + \frac{\varsigma}{2}(\partial_y h)^2 + \eta, \qquad (4.6)$$

where $\bar{h}$ is the average height of the overall surface. Mathematically, with $\chi > 0$, this term leads to stabilization of the surface at any point. The meaning and influence of this redeposition-related contribution to the dynamics were further solidified by the studies carried out by Linz *et al.* [155, 156]. Eq. 4.6 can then be scaled in time and spatial coordinates, as demonstrated in Ref. [149], resulting in Eq. 4.1, the simplified adKS equation we numerically integrate in the following. The parameters appearing in Eq. 4.1 can be related to the original ones by $\gamma = K\chi/v_x^2, \alpha = v_y/v_x, \beta = \varsigma_y/\varsigma_x$. Here the arbitrariness of χ leads to that of γ (we set $\gamma = 0.1$ in the following), and the exact value of finite K becomes irrelevant. As above-mentioned, α and β, which quantify the anisotropy for the linear and nonlinear terms in adKS equation, can be extracted from SRIM simulation, and with diamond being treated with Ar^+ ions at 70° and 700 eV, we have $\alpha = -0.3556$ and $\beta = 0.3024$. Result from numerical integration of Eq. 4.1 with finite difference method is shown in Fig. 4.6. The simulated pattern shows formation of ripples and local defects, similar to that observed in experiments, but the current theoretical development cannot quantitatively predict the process [131].

4.2 Nanoparticles Dewetted on Textured Surface

It is a well-known phenomenon that the morphology of surface influences the characteristics of metal film dewetted thereon, and this fact has led to the development of many interesting

---

[1]We discuss in more detail in Appendix A how χ influences the simulation results.

self-organized structures [157, 158]. Below we show that the nanoripples on diamond may also work as a template for the morphological control of gold nanoparticles (AuNPs).

4.2.1 AuNPs on Nanodots

Similar to the abovementioned procedure, we use IBE to treat a diamond (100) surface at ion incidence angle 60° with sample rotation of 10 rpm for 30 minutes. The employed flux and acceleration energy were 1.1 mA/cm^2 and 700 eV respectively. A gold film was then sputtered with varying thickness using Alliance-Concept DP 650, followed by annealing at 500°C for one hour, resulting in AuNPs with different diameter and spatial distribution. For comparison, we fabricate AuNPs on reference samples that are polished to sub 1 nm roughness.

In Fig. 4.7 one can readily observe that the distribution in both diameter and spacing for AuNPs on textured surfaces is much more uniform compared to the reference samples. With increasing film thickness, however, the uniformity becomes worse due to, as shown in Fig. 4.7, that small AuNPs merge into bigger ones. Nevertheless, compared to reference samples, the nano-roughened surface still results in better uniformity of AuNPs.

Statistical analysis on AuNPs diameter is shown in Fig. 4.8 (a) for the case of 1.4 nm deposition of gold, where the measured data is fitted with Gaussian lineshape. AuNPs on textured diamond have diameter of 9.11 ± 2.17 nm compared to that of 9.96 ± 2.94 nm on the reference
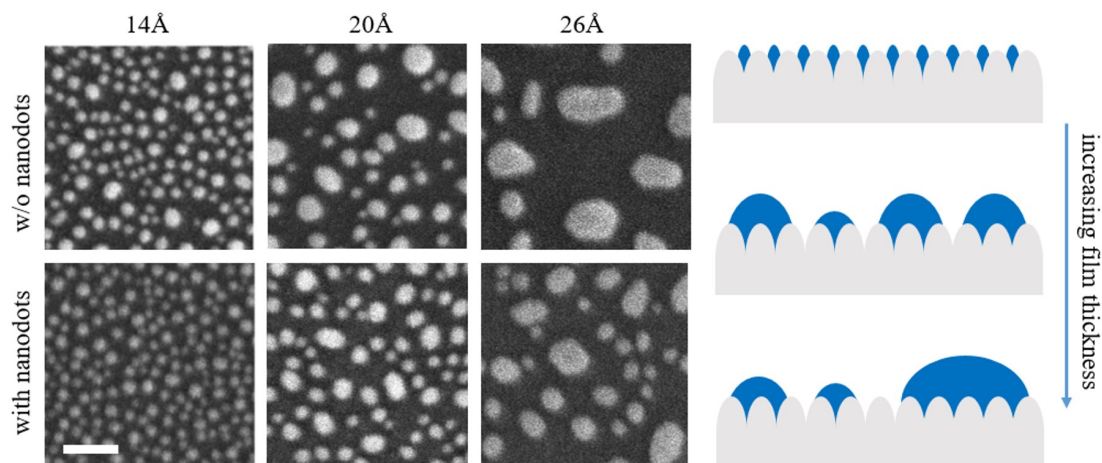
Figure 4.7 – A comparison between AuNPs dewetted on smooth and textured diamond surface (scalebar 50 nm). The deposited gold film was 1.4, 2, 2.6 nm thickness respectively. On surfaces with nanodots, AuNPs clearly show much better uniform distribution. With increasing film thickness, the average diameter of AuNPs grows and the distribution becomes less uniform, which is explained by the schematic in the right panel, *i.e.* small particles merge into bigger ones as the film thickness increases. This observation is consistent with the theory developed in Ref. [159] for solid-state dewetting on curved surface.
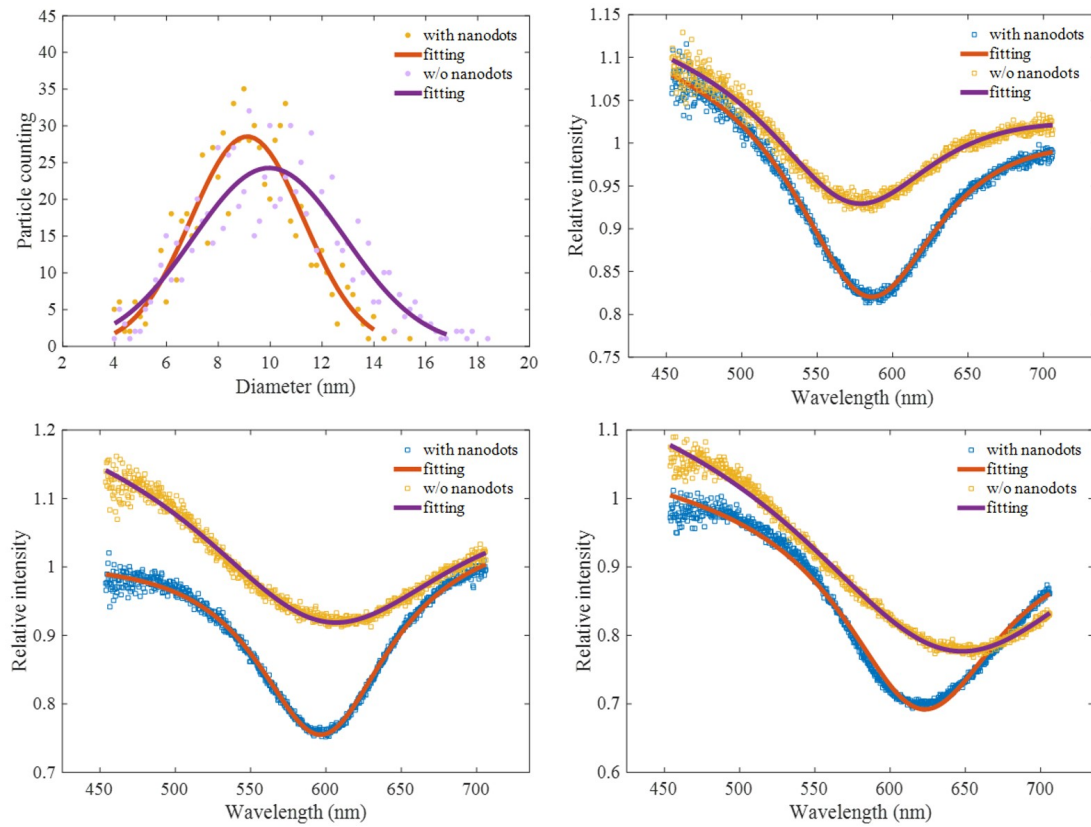
Figure 4.8 – (a) Diameter distribution of the AuNPs for 1.4 nm gold film dewetted on diamond surface with and without nanodots. (b,c,d) Transmission spectra of AuNPs-decorated diamond substrates with deposited gold film thickness of 1.4, 2, 2.6 nm respectively. Explanation for linewidth narrowing and blue/red shifting of center wavelength of extinction are found in the main text.

sample. Optical measurement of both samples were performed in the wavelength range from 450 nm to 700 nm, as shown in Fig. 4.8 (b). The relative intensity is the transmission through a AuNPs-decorated sample compared to the spectrum of a bare diamond sample, *i.e.* with no AuNPs on it. At wavelengths < 500 nm, the relative intensity of the transmitted light is larger than one, suggesting the presence of directional scattering [160]. Taking into consideration the closely packed distribution and smaller average spacing of AuNPs on textured surface, the red-shift of the center wavelength for extinction is consistent with the plasmon hybridization model [161], while the sharper diameter-distribution corresponds to narrower Lorentzian lineshape (120.7 nm linewidth for textured sample compared to 140.1 nm for smooth diamond surface). Similar observations are found for sample deposited with thicker gold film, with the difference that the center wavelength of extinction is blue shifted, as shown in Fig. 4.8 (c,d). This can be attributed to the smaller average diameter of AuNPs as plasmon hybridization no longer plays an important role with increasing particle spacing.
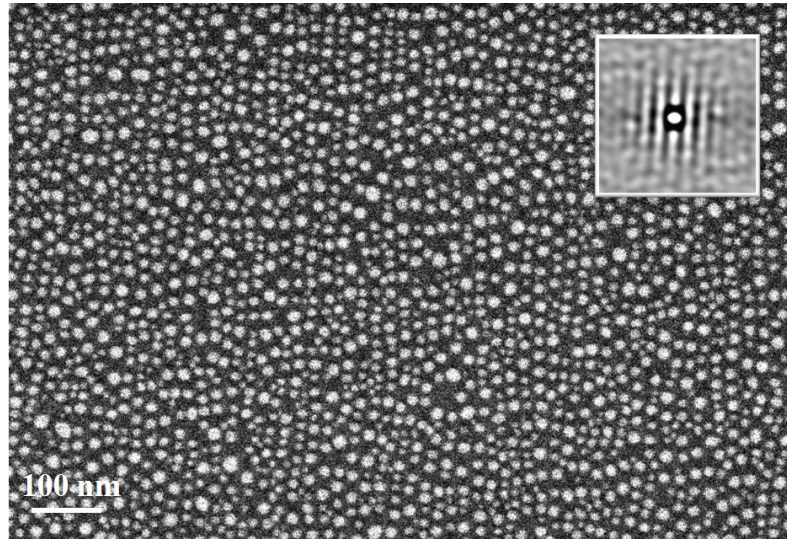
Figure 4.9 – Partially aligned AuNPs dewetted on diamond surface with nanoripples. Inset shows the short-range autocorrelation function calculated over the whole picture.

4.2.2 AuNPs on Nanoripples

Not surprisingly, if nanodots can assist solid-state dewetting into a better uniform distribution, nanoripples should be able to align the AuNPs along certain directions. This is shown in Fig. 4.9. However, since the ripple patterns are not perfectly ordered in long-range and the ripple amplitude is not large enough to completely confine the dewetted particles, we only achieve good alignment in small areas. The overall ACF (auto-correlation function) is shown in the inset of Fig. 4.9, and clearly only short-range order exists.

In our experiment 700 eV is the maximum acceleration energy achievable by the IBE tool. For higher energy ions, ripples with larger amplitudes can self-organize and it can be expected that nanowires can be fabricated directly in a bottom-up way without any lithography processing.

5 Fabrication of Free-Standing Photonic Structures in Bulk Diamond

The well-established semiconductor industry built on Silicon and GaAs (or III-V compound in general) heavily relies on thin film and wafer-bonding technologies, yet for diamond both are challenging. We briefly explain the reason for this in the next section and summarize several possible ways to fabricate integrated diamond photonic devices. As scalable production of high-quality single crystal diamond thin films is currently not feasible, we demonstrate angled reactive ion etching assisted by Faraday cage for the fabrication of free-standing structures in bulk diamond, with a novel design for reproducible Faraday cages. The intrinsic limitation of this approach on scalability due to etch-gradient (c.f. section 5.3) is discussed before closing this chapter.

5.1 Fabrication of Diamond Photonic Structures

We explain in this section why thin films, which established technologies are good at dealing with, are difficult to obtain from single crystal diamond (SCD). In fact, even when a SCD thin film is made successfully, the quality is usually not satisfying due to fabrication non-idealities. This motivated the community to move to SCD processing technologies that do not require thin films. We summarize briefly demonstrated fabrication methods starting from bulk diamond substrates, before diving into angled reactive ion etching which we chose to fabricate suspended photonic devices.

5.1.1 Diamond Thin Films

To understand the difficulty in obtaining single-crystal diamond thin film, basic knowledge of diamond growth is indispensable. We have briefly mentioned in Chap. 2 that the availability of high-quality, reproducible diamond substrate has only become possible recently via MPCVD growth. More specifically, depending on the substrate type, there are homo- and hetero-epitaxial growth of diamond, with only the former, at the present day, resulting in diamond single-crystals with well-controlled impurity level and low dislocation density [162]. The
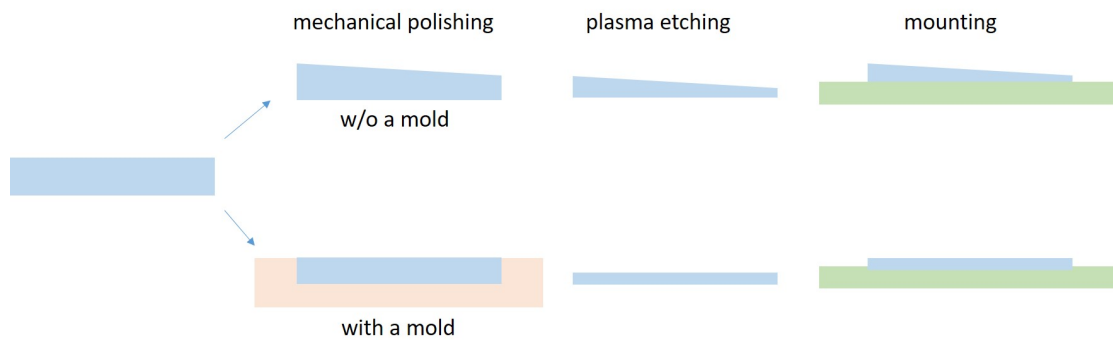
Figure 5.1 – Process flow for fabricating diamond-on-insulator via mechanical polishing. Without using a mold, the mechanically polished substrate usually has a wedge, which cannot be eliminated in the subsequent etching steps. The anisotropy of polycrystalline diamond can effectively stop the polishing of single crystal diamond, therefore if the polycrystalline diamond mold can be made uniform, the resulting single crystal diamond substrate could have improved quality.
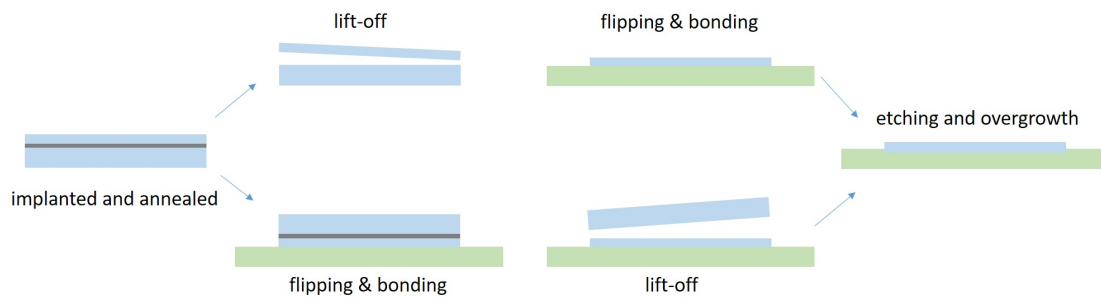
Figure 5.2 – Process flow for fabricating diamond-on-insulator via implantation. Flipping of a thin membrane is difficult and risky, but bonding is relatively easy as the thin film can deform elastically to adhere to the substrate. On the other hand, flipping of a bulk substrate is straightforward, but bonding it onto a carrier wafer can be challenging. In both cases etching is usually carried out to remove implantation induced damages.

homoepitaxial growth starts from a seed diamond substrate, typically (but not necessarily [163]) HPHT-grown and fine-polished. After growth the resulting crystal is laser-sliced to obtain the CVD layer [1], which is subsequently polished to a smooth and flat surface. From here on, two methods have been investigated to fabricate thin films.

The straightforward way is mechanical polishing, which can be employed to reduce the

---

[1]While laser-slicing is the conventional way to cut diamond, recently a new lift-off approach based on epitaxial lateral overgrowth has been demonstrated convenient [164].
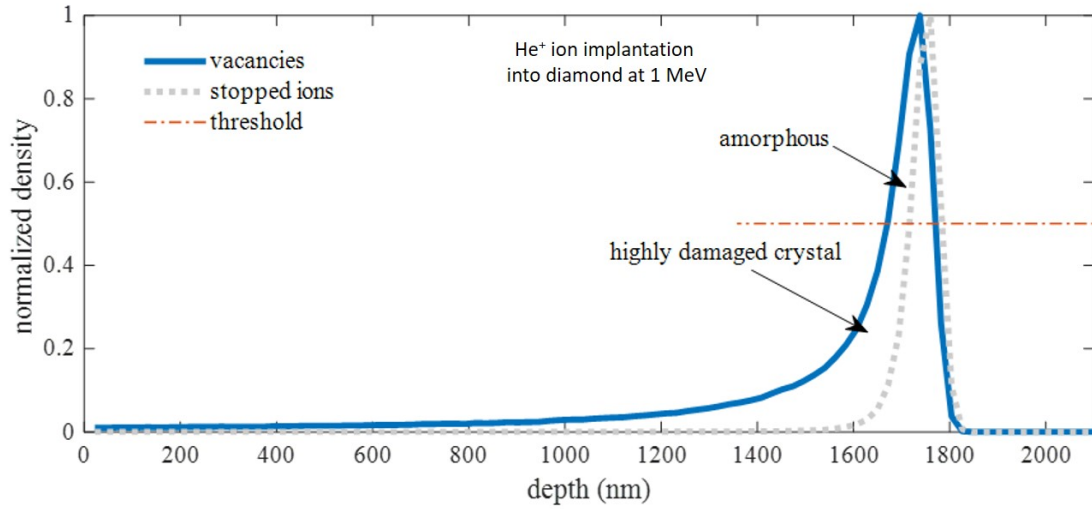
Figure 5.3 – SRIM simulation of He$^+$ ions implantation into diamond at 1 MeV acceleration energy. The distribution of vacancies created by energetic ions and the stopped ions are plotted against depth. Above a certain damage threshold, the diamond becomes amorphous carbon and can be etched electrochemically, while a layer of highly damaged crystal diamond remains in the diamond film and cannot be recovered completely back to pristine diamond lattice.

thickness of the substrate down to ∼ 5 μm [165, 166, 167] if the dimension is not too large [2] (less than a few millimeters), following which RIE (reactive ion etch) can be applied to further thin it down to a few hundred of nanometers [168, 169]. This approach has been demonstrated successful in fabricating on-chip diamond resonators with record-high optical quality factor (1E6) [3] [169]. Nevertheless, apart from the limited lateral dimension achievable, the uniformity of film thickness cannot be guaranteed both in polishing [167, 171] and in etching [172] steps [4]. To counter these problems, it has been proposed to use a polycrystalline diamond (PCD) mold for assisting thin-film polishing which results in less wedging (as explained in Fig. 5.1), and thickness variation due to non-uniform etching of the mold may be improved by rotating the sample during processing [173]. Although improvement has been demonstrated [174] with this method, its scalability is questionable as increasingly large diamond substrates would always require a larger PCD mold, yet the uniformity and flatness of such molds are challenging to guarantee.

On the other hand, ion slicing [175] can produce a layer with uniform thickness [176] from

---

[2]The thickness achievable from mechanical polishing depends highly on the crystal quality and substrate dimension. As the risk of fracturing is high, this approach cannot guarantee yield for making ultra-thin membranes with large dimensions.

[3]The highest reported optical quality factor from single crystal diamond resonator is 2.4E7 in Ref. [170] but the cavity is a fine-polished sphere instead of an integrated on-chip device.

[4]In Ref. [167] the authors demonstrated a method to reduce the wedge: placing the substrate at an inclined angle during RIE.
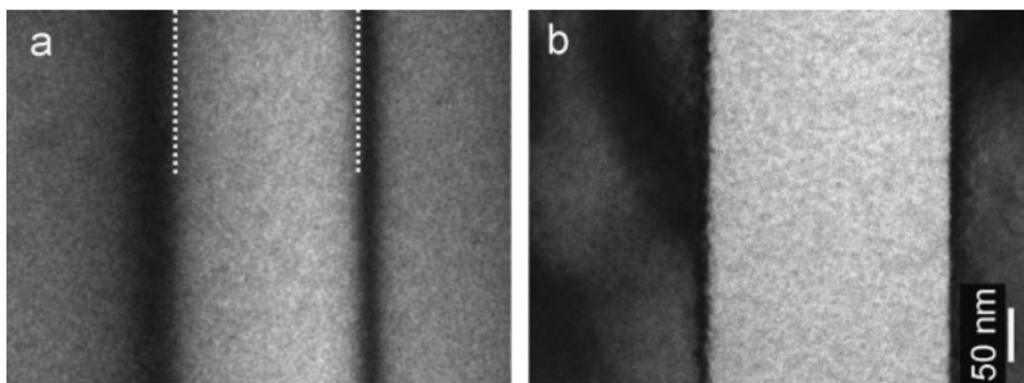
Figure 5.4 – Transmission electron microscopy (TEM) characterization of diamond after implantation (a) and after subsequent annealing at 1260 °C (b). The light-colored region corresponds to amorphous carbon and the interface between amorphous carbon and diamond shrinks after annealing. Reprinted from Ref. [178] with permission from Wiley publishing.

hundreds [177] to thousands [178] of nanometers. In this approach, accelerated ions travel in the substrate until they lost the kinetic energy due to interaction with the target material and are stopped at a well-defined depth, which depends on the acceleration energy and ion species, and this depth can be simulated in SRIM package. When damage accumulated in the implant layer reaches a threshold (on the order of 1E22 vacancies per cm^3 [178, 179]), it becomes amorphous and is etch-able electrochemically [180], facilitating lift-off of the material there-above, as shown in Fig. 5.2. However, from simulation we can readily observe (Fig. 5.3) that in the case of implantation with high energy (1 MeV), the released thin film has a significant part that is not amorphous but nevertheless highly damaged. A high-temperature (> 1000°C) annealing step is commonly carried out before the lift-off, which helps restore the crystallinity, and sharpens the diamond–amorphous carbon interface to $\leq 10\ nm$ width, as shown in Fig. 5.4. Ref. [181] further reported residual damage after annealing (2 hrs at 950 °C) by observing the damage-related Raman peak position, indicating that the whole layer which ions traveled through is of compromised quality. For comparison, a scanning transmission electron microscopy characterization was carried out very recently on a 60 keV H^+ ion implanted diamond sample [177], and the crystallinity of the top layer seemed preserved, in spite of its thickness being only ~ 250 nm. Overgrowth with a slow rate [182] can be performed though to eventually achieve a smooth thin film with desired thickness for device fabrication, and in Ref. [183] the authors reported comparable crystallinity between regrown and seed diamond, demonstrating overgrowth as an efficient approach for obtaining high-quality SCD films. Another advantage of this fabrication technique is the resulting ultra-smooth surface as shown in Ref. [184]: the initial substrate was with roughness about 4 nm, and after lift-off the interface had roughness about 0.6 nm.

While both above-mentioned routes can lead us to diamond thin films, with the latter more promising for scalable fabrication, subsequent handling of the resulting freestanding mem-
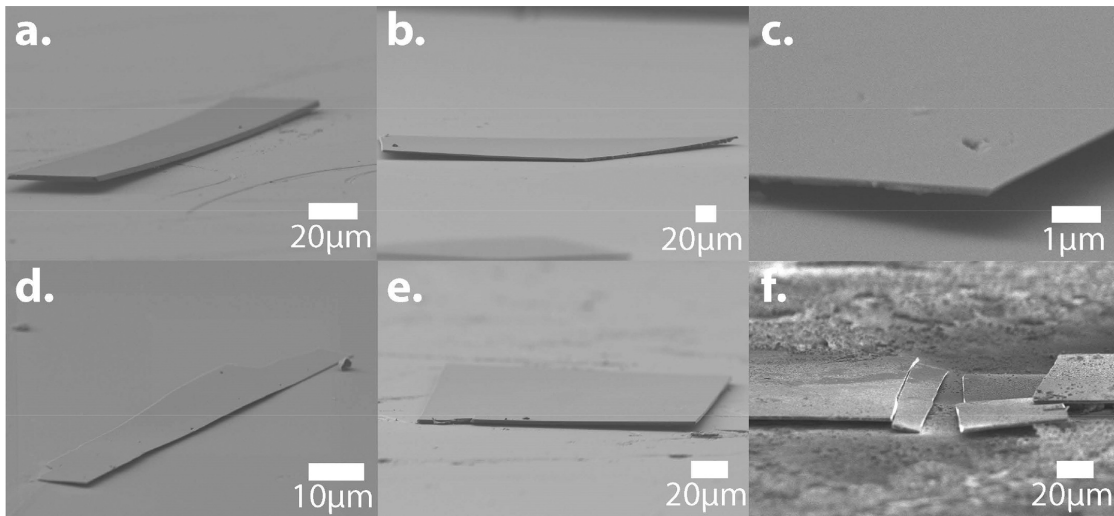
Figure 5.5 – Thin films of single crystal diamond fabricated by implantation and lift-off, the induced strain in the material causing curling. The dimension is limited and the handling is difficult. A shattered film is shown in (f). Reprinted from Ref. [185] with permission from Elsevier.

brane can be troublesome during its transfer to a carrier substrate for further processing. An SEM picture of a shattered film can be found in Fig. 5.5 for example, where one can see how delicate it is in manipulating the thin diamond [5], and thus this fabrication method is highly unlikely to scale up. A possible workaround to avoid this hassle is to bond the top layer after ion implantation on a carrier substrate before electrochemical releasing [186], and with recent progress in diamond-on-silicon hydrophilic bonding [187, 188, 189] and surface activated bonding [190, 191, 192], this seems a rather promising way to realize a diamond-on-insulator (DOI) platform in the future. The uncertainty remains in the feasibility of bonding diamond onto a low refractive-index material to facilitate wave-guiding: for example, direct bonding between diamond and fused silica was observed more than two decades ago [193], but systematic study of the bonding strength and its resistance to temperature-change remains absent in literature.

5.1.2 Fabrication in Bulk Substrate

To circumvent the difficulties in diamond thin film fabrication, a few processing techniques have been developed for structuring free-standing devices directly from bulk substrates. A brief overview of these method is given below, with angled-etch approach explored in more detail in the forthcoming section.

---

[5]Diamond is hard but not tough: hardness indicates the resistance of a material against localized plastic deformation induced by, for instance, mechanical indentation, while toughness is the ability of a material to plastically deform without fracturing.
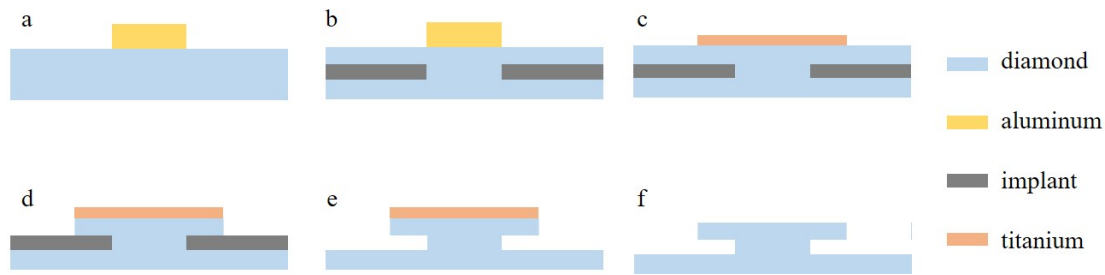
Figure 5.6 – Process flow for fabricating suspended structures via masked implantation and electrochemical undercut. Note that aluminum and titanium can be replaced by any other materials as long as they serve the purpose of stopping implants and masking diamond in plasma etching, respectively. (a) define a mask for stopping implants; (b) implantation; (c) define device pattern; (d) pattern transfer; (e) electrochemical etch of amorphous carbon; (f) mask stripping.

An early attempt towards free-standing diamond device dates back to 2007 [194], where selective implantation was carried out to amorphize partially the diamond sub-surface. This process flow is illustrated in Fig. 5.6. Similar to the ion slicing method for thin film fabrication, the resulting suspended device would have a bottom layer with compromised crystallinity, which can deteriorate device performance by, for example, optical absorption. Conceptually, it is possible to remove this layer by covering the device from top and side via sputtering a protective film before annealing it in oxygen, but whether the bottom-side surface smoothness can be preserved remains unknown. The necessity of backside etching also comes from device geometry. In Fig. 5.3 and 5.4, one can observe that the undercut of amorphous carbon could leave only 100 – 200 nm space below the device layer, which is not sufficiently wide for preventing light guided therein from leaking into substrate evanescently.
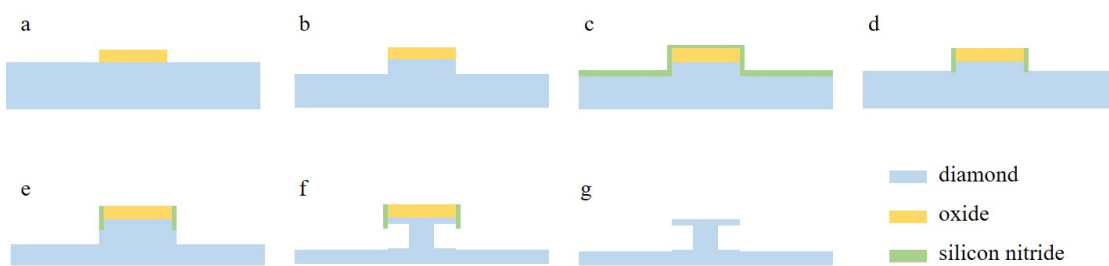
Figure 5.7 – Process flow for fabricating suspended structure via SCREAM process. The oxide and silicon nitride can be replaced by other materials as long as they serve the purpose of masking diamond in the etching steps. (a) define device pattern; (b) pattern transfer; (c) conformal deposition of masking material to protect the sidewall (ALD or PECVD); (d) vertical etch of conformal layer to expose part of the diamond; (e) vertical etching of the diamond; (f) quasi-isotropic etch of the diamond; (g) mask stripping.

Alternatively, undercut can be realized by a SCREAM (single-crystal reactive etching and metallization) -like process [195] first demonstrated in single crystal diamond by Barclay group [87]. As shown in Fig. 5.7, the final etching step removes (uncovered) diamond in all directions, achieving undercut and suspended structures. Free-standing photonic crystal cavities have also been demonstrated with this process flow [196, 88]. While this process flow has the advantage that it requires only standard equipment, an intrinsic limitation is that the etch-rate depends on the exposed geometry (etching happens quasi-isotropically) and crystal-plane (etch-rate on different planes differs), therefore restricting the design flexibility [88].

In contrast to the two approaches mentioned above, angled RIE is a simple and straightforward process as seen in Fig. 5.8. However, a well-defined etch angles do not come with standard RIE equipment. To define this angle, either reactive IBE [197] can be resorted to, or a Faraday cage could be of help. More details about this technique are explained in the next section.

5.2   Angled Reactive Ion Etch

Early demonstrations of Faraday-cage assisted RIE were studied back in 1980 [198]. It was not extensively used since then as SOI platform renders it unnecessary, at least for most photonic applications. The first report of this technique being applied to structuring single crystal diamond was published in 2012, authored by Lončar group at Harvard University [86]. Two years later the same group reported high-Q nanobeam and racetrack resonators fabricated with this method [199], solidly proving it a reliable way for device manufacturing. In literature this Faraday cage [200, 86, 199, 201, 202] was typically molded by hand from aluminum mesh resulting in a cage geometry that is not well-defined and accurately repeatable. This is not
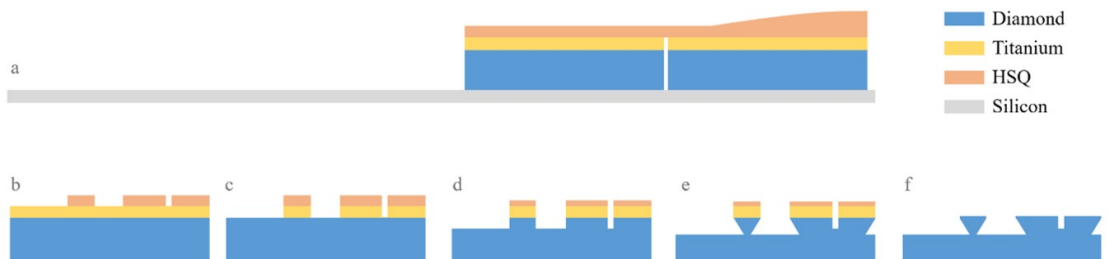
Figure 5.8 – Process flow for fabricating suspended structures via angled etch. Titanium can be replaced by other masking materials. The carrier wafer can be made of materials other than silicon, and is not drawn for steps b to f. (a) diamond substrates, aligned and touching each other, with titanium film deposited on top, are glued near the edge of a silicon carrier wafer for spin-coating of HSQ resist; (b) HSQ is exposed and developed; (c) pattern transferred from HSQ to titanium via Cl_2/BCl_3 chemistry RIE; (d) pattern transferred from titanium to diamond via O_2 chemistry RIE; (e) angled-etch in a Faraday cage with O_2 chemistry RIE; (f) hardmask removal.

ideal for subsequent etching as we explain shortly. We demonstrate in the following a new design route for preparing the Faraday-cage, which further facilitates this technique to become repeatable and standardizable.
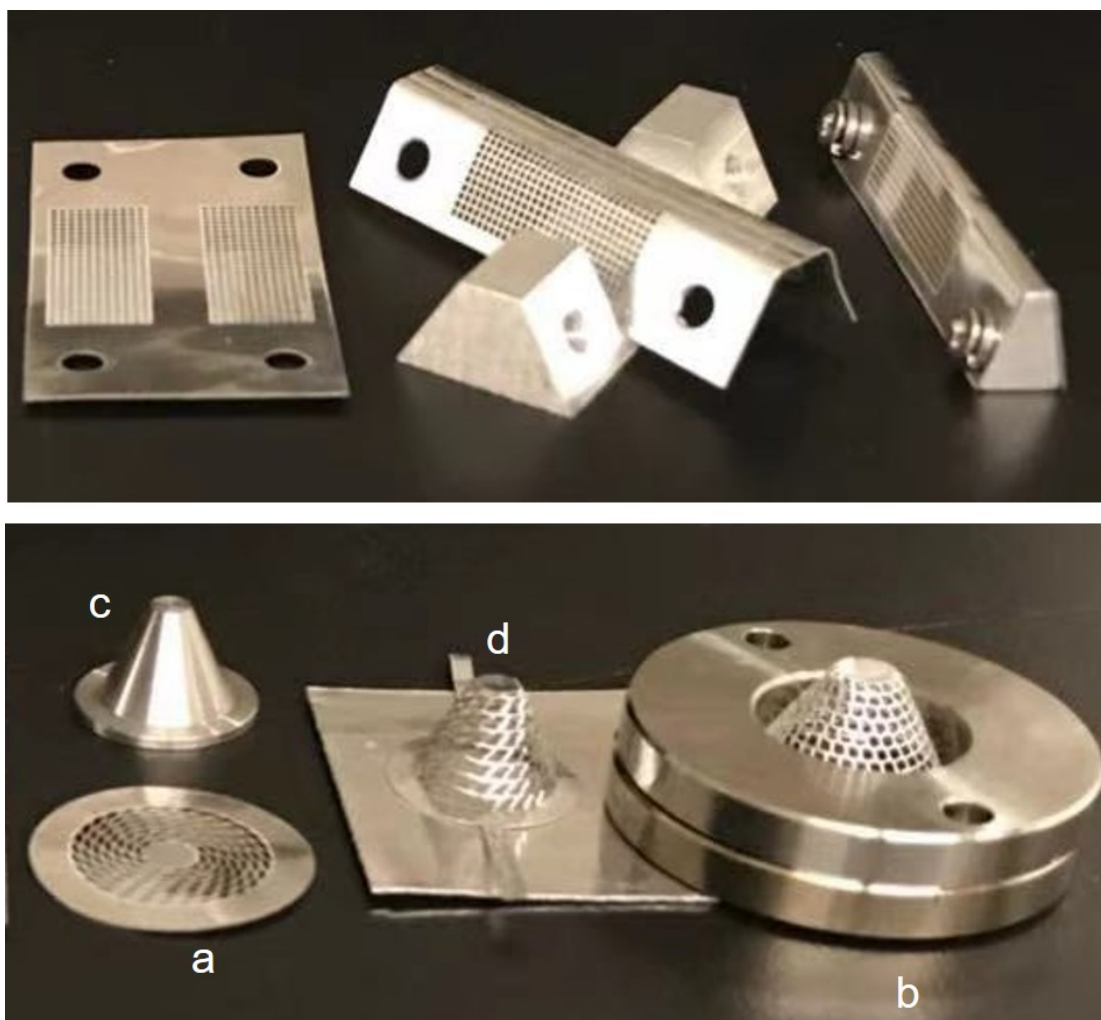
Figure 5.9 – Patterned aluminum foil and accessories for making Faraday cages. For the cone-like cage: first a pattern is written on an aluminum foil (a) via laser ablation, after which a pair of clamps (b) is used to hold the rim, so that one can use a mold (c) to extrude the foil into a 3D cage. Before sent into the plasma etcher, a diamond substrate is placed on another aluminum foil serving as the conducting base and the extruded cage is electrically connected to the base either with aluminum conductive tape or with screws if a tail (d) is available for fixing the cage onto the foil base at a distance from the cage center (otherwise the the screw may modify the electric field distribution and therefore introduce asymmetry for the etching). While the aspect ratio can be changed easily by varying the design parameters, a fundamental limit is set by the geometrical limitations as explained in Appendix B. Here all materials (pure aluminum and stainless steel) are compatible with ICP-RIE etcher without introducing contamination.

5.2.1 Reproducible and Symmetric Faraday Cage

From literature, *e.g.* Ref. [200], one can readily observe that a cage molded from planary mesh is highly asymmetric in terms of the distribution of openings. This is not only because of that it was hand-made, but more fundamentally restricted by topology. Consequently the etching is not azimuthally isotropic and it requires frequent rotation of the sample during angled RIE to produce a symmetric design. Another disadvantage of molded cage is the opening at top which leads to unwanted (and unnecessary) vertical etching of the hard mask. It was also observed that a stop on top of the cage [202] helps achieve a more acute etch-angle. Moreover, as the starting material is industrial aluminum mesh with standard specifications, the design flexibility (pitch, wire-thickness, *etc.*) is limited. These motivated us to come up with a new way to fabricate the Faraday cages.

We made two types of Faraday cages: triangle-shaped and cone-like. As shown in Fig. 5.9, both kinds are fabricated via laser ablation of a planary aluminum foil. The resulting mesh is then transformed into 3D. In this way we can choose the foil thickness and change the pitch and duty-cycle of the openings. By varying the design on the 2D foil, repeatable and standardizable Faraday cages can be made easily with a high degree of flexibility, and the resulting cage is highly symmetric, therefore no sample rotation was necessary in the subsequent etching steps.

5.2.2 Fabrication Results

The process flow is depicted schematically in Fig. 5.8. We use HSQ (XR-1541-006) for ebeam lithography and transfer the pattern into 200 nm of titanium which serves as the hardmask, via Cl_2/BCl_3 chemistry in an ICP-RIE (inductively coupled plasma reactive ion etching) etcher. The choice of titanium is due to its high etch selectivity against diamond and that it does not produce redeposition. The titanium pattern is then transferred into the diamond substrate via O_2 plasma etching. At this stage we mount the diamond at the center of a Faraday cage and continue using O_2 plasma etching to undercut the structure. Eventually the titanium mask and possibly residual HSQ resist are removed in dilute HF solution.

While the process flow seems straightforward, there are a few cautions to be aware of, in order to successfully fabricate suspended structures:

(I) as diamond substrates are rather small (3mm by 3mm in our case), after spin-coating of photoresist or HSQ, the uniformity of the coated film is usually not satisfactory due to the formation of edge-bead. This is the reason in step (a) of Fig. 5.8, we mounted two (or more) substrates, aligned and touching each other, near the edge of the carrier wafer: in this way the edge-bead forms only on the outer-most chip and the HSQ thickness is uniform for the chips towards the center. An extreme case of non-uniform coating is shown in Fig. 5.10 (a), where half of the HSQ was completely removed, while the remaining part shows thicknesses ranging from near-zero to a few hundred nano-meters.

(II) in fabricating nanobeam photonic crystals, the holes have critical dimension < 100 nm,

and they are developed slower than larger openings. With HSQ insufficiently developed, the pattern transfer from HSQ to the titanium hard mask would be incomplete. Consequently, small features (critical dimension < 100 *nm*) as shown in Fig. 5.10 (b) were not transferred to diamond successfully.

(III) shown in Fig. 5.10 (c) is a single-clamped racetrack cavity undercut partially, with the released part showing strain-related bending. The fabrication of this sample started directly from a mechanically polished substrate, and the resulted stressed subsurface layer is believed to be the cause of the bending. In another attempt in fabricating the same structures, the substrate was first polished by IBE and then deep-etched by > 5 μm via cycled O_2 and Cl_2 RIE. The resulted surface remains smooth and the device fabricated was free from bending.

(IV) accurate timing of the undercutting process is important for obtaining suspended structures. A negative example is shown in Fig. 5.10 (d) where one of the resonators was over-etched and charged during SEM observation, and consequently it was flipped and
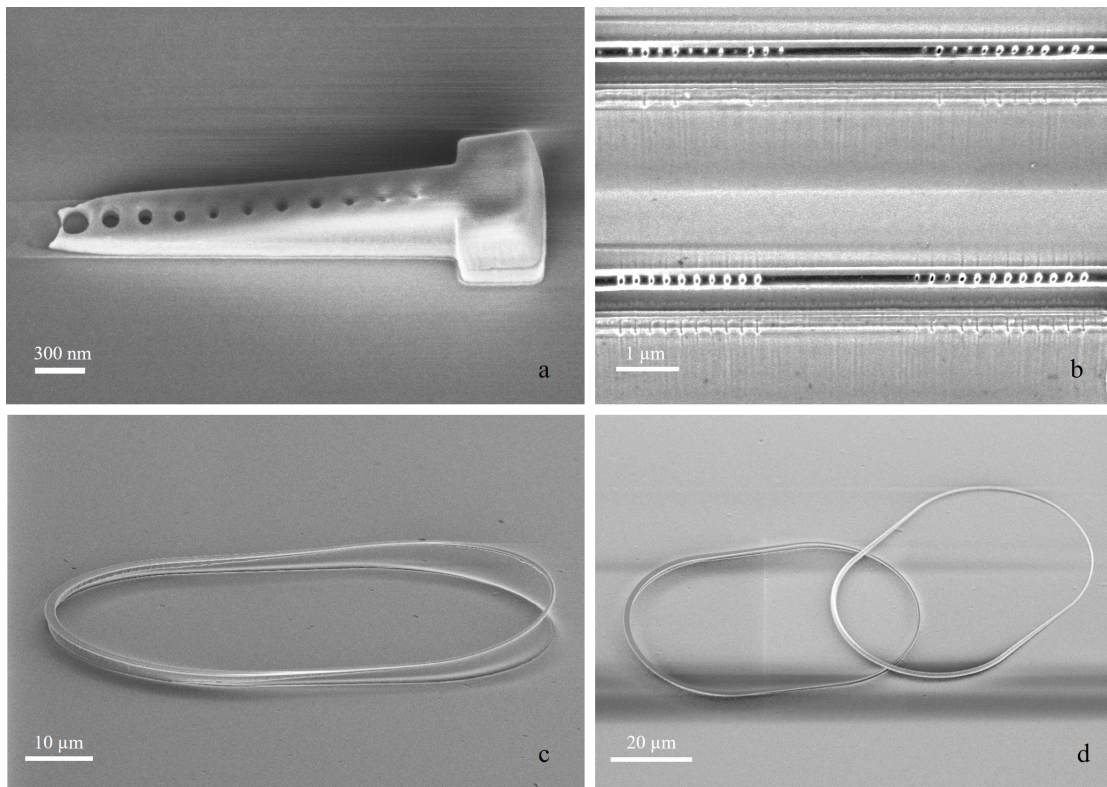
Figure 5.10 – (a) An extreme case of non-uniform coating of HSQ, leading to partial survival of the hardmask. (b) HSQ not developed enough and small holes are not etched into diamond. (c) Mechanical polishing induced stress remains in the top layer of diamond substrate (a few microns thick) and without removing this layer the resulted structure bends. (d) A racetrack cavity is over-etched (detached from the substrate) and flipped by electrostatic force during SEM observation.
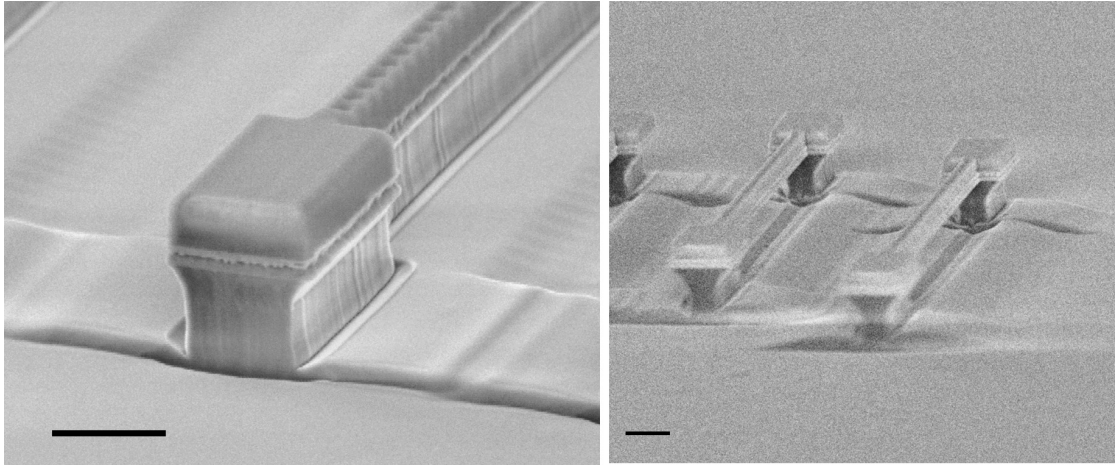
Figure 5.11 – Undercut of a nanobeam, halfway-etched (left) and fully-suspended (right). Material stack: HSQ, titanium, diamond. Scalebar 1 micron.

displaced by electrostatic force.

In Fig. 5.11 we show the undercut of a diamond nanobeam using triangular shape Faraday cage. The vertical etch for pattern transfer takes about 10 – 15 min and the undercut takes about 15 – 20 min to finish for a nanobeam that is a few hundred nanometers wide. In Fig. 5.12 we show the fabrication results of various structures.

Smoothening of sidewall after undercutting the diamond structure is possible by ICP-RIE with Ar/Cl$_2$ chemistry at a relatively high (30 mtorr) chamber pressure, as shown Fig. 5.13. This choice of processing condition is due to the known effect of high chamber pressure in producing inverted tapering profile [203]. The titanium layer is stripped in this step and the sidewall roughness can be improved. As Ar/Cl$_2$ chemistry etches diamond isotropically [204], including this processing step requires dimension compensation during layout drawing in order to faithfully produce the design.

5.2.3 Optical Characterization

The cavity shown in Fig. 5.12 (b) was probed by dimpled fiber tapers [6] as shown in Fig. 5.14. A tunable laser was used for frequency sweeping over 30 nm and the transmission spectrum is recorded. A FSR (free spectral range) of 4 nm was measured consistent with the cavity geometry, with quality factor about 2'700, as shown in Fig. 5.15. The limited q-factor can be due to surface roughness, scattering at mechanical support, material absorption, and over-coupling (the fiber was in touch with the cavity during measurement).

---

[6]The fabrication of dimpled fiber is detailed in Appendix C.
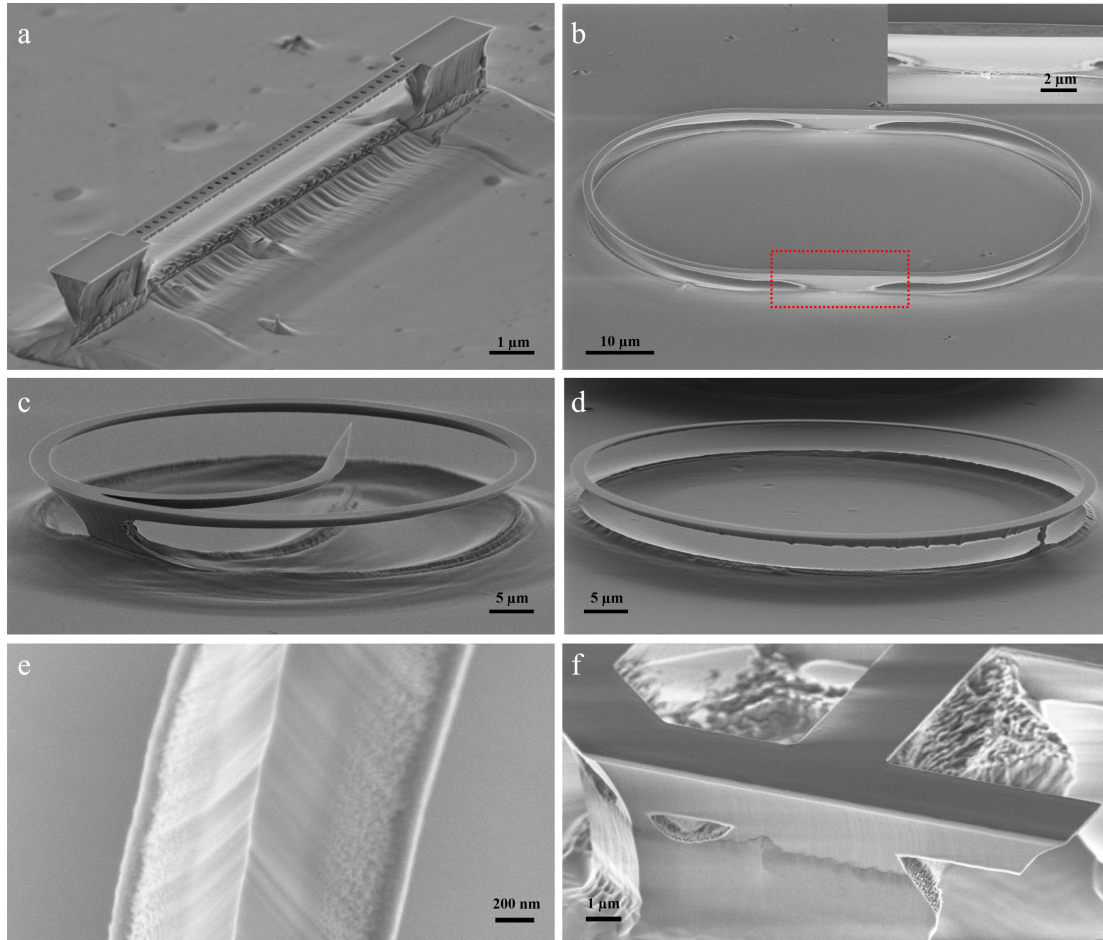
Figure 5.12 – (a) Nanobeam cavity with design wavelength at 637 nm. (b) Racetrack cavity with tapered support region shown in the inset. (c) Ring resonator with a tail. (d) Asymmetric ring with a single support. Severe roughness was observed on the angled sidewall, which is suspected to originate from titanium mask erosion. (e) Bottom view of a flipped ring, with titanium mask still on diamond surface. On the sidewall, roughness can be observed close to titanium mask, and it is clear that some diamond immediately under the Ti mask was etched away, possibly due to reflected oxygen ions during RIE. (f) Smooth sidewalls can be observed in most runs.

5.3 Limitations

While Faraday cages can be used for assisting angled-etch in prototyping, its scalability is intrinsically limited, not only by its finite volume, but also due to etch-gradient originating from non-uniformity of electrical field distribution even in the case of a highly symmetric cage. This phenomenon has been studied in Ref. [200] via FEM simulation, and here we show in Fig. 5.16 an experimental observation. For the case of triangular Faraday cages, only a row of structures lying in the middle of the diamond substrate have symmetric undercutting. The

non-uniform etching for a cone-like Faraday cage is more severe as (azimuthally) symmetric etching only takes place in the very center of the cage, as reported in Ref. [205].

Nevertheless, we note that it is not angled-etch that is not scalable. Recall that we used broad beam of Ar^+ ions to polish the substrate in Chap. 3, which is a wafer-scale process thanks to the uniformity of the ion beam. If the ion source can be replaced by oxygen, angled-etch of diamond can be carried out on a large scale without using Faraday cages, such as that demonstrated in Ref. [197].
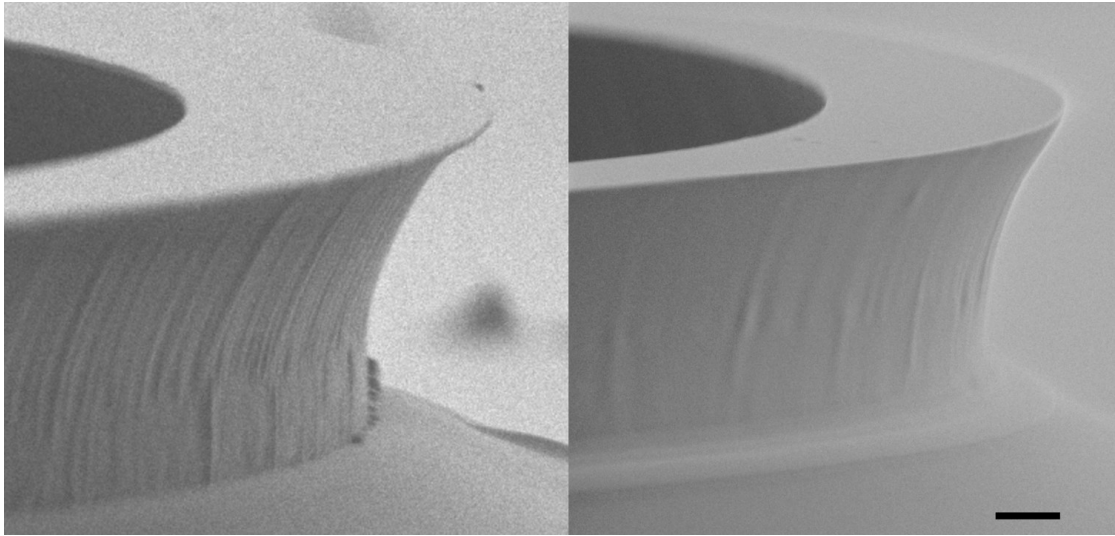
Figure 5.13 – ICP-RIE with Ar/Cl$_2$ chemistry at 30 mtorr chamber pressure was able to smoothen the sidewall of diamond structures. Note that the titanium layer was also removed and the final structure dimensions are less controlled. Scalebar 1 micron.
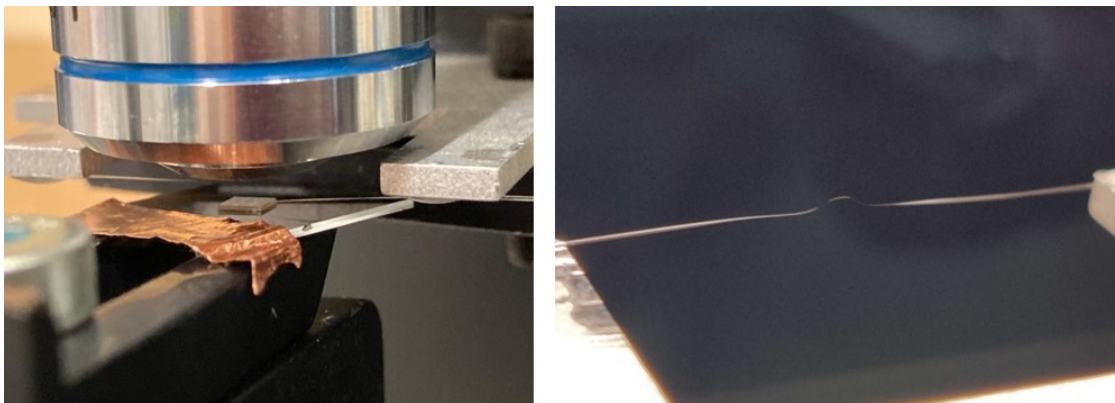
Figure 5.14 – Left: sample under microscope and cavities thereon evanescently coupled to tapered fiber, which is positioned with a piezo-actuator. Right: dimpled fiber taper used for probing individual cavities.
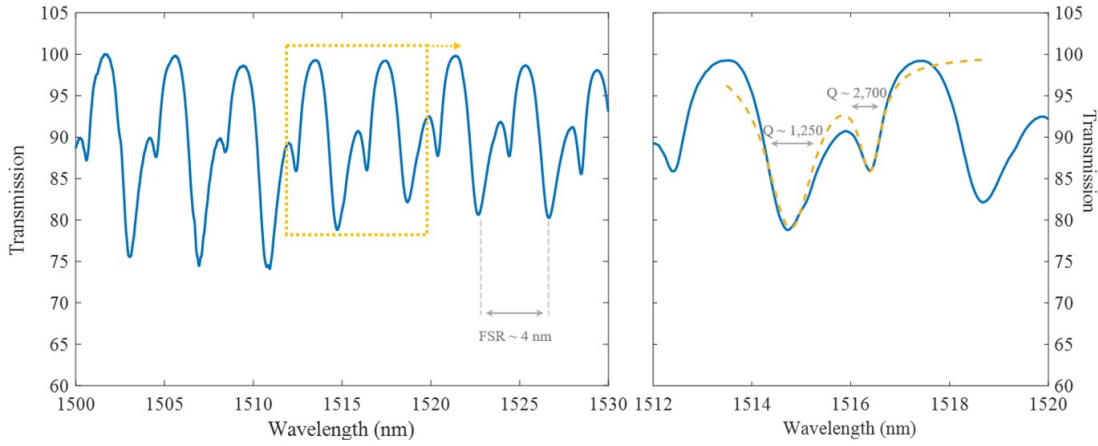
Figure 5.15 – Transmission spectrum for a racetrack cavity. Free spectral range of 4 *nm* was consistent with the cavity geometry and the best quality-factor measured was about 2'700.
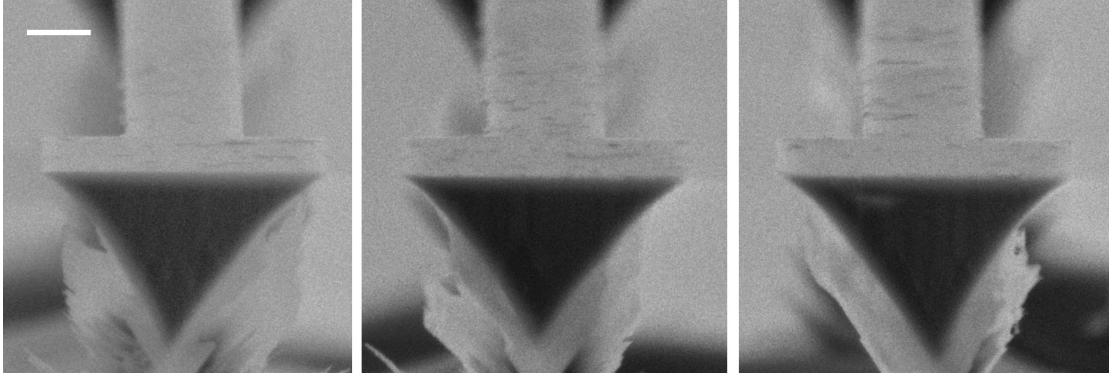
Figure 5.16 – Asymmetric undercut of nanobeams. The left and right images correspond to structures close to substrate edges, and the center image corresponds to a beam in the middle of the substrate. Scalebar 300 *nm*.

5.4 Design of Directional Couplers

While angled-etch has been proven versatile in demonstrating high-brightness single photon sources [206], quantum nonlinear optics [207], quantum memories [43, 46], *etc.*, it is difficult to interface individual photonic structures due to their triangular cross-sections. In this section we show that in principle a directional coupler is possible to be realized for facilitating integrated circuits.

As shown in Fig. 5.17, a typical directional coupler consists of two waveguides close to each other. Lightwaves guided in one waveguide can evanescently couple to the other. When only one port is excited, depending on the coupling strength and propagation distance, the light can transfer to another waveguide partially or completely, in the former case the coupler
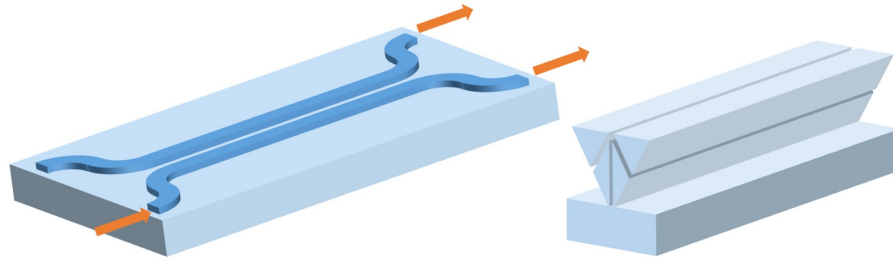
Figure 5.17 – Left: a directional coupler composed of two waveguides close to each other where light can transfer from one waveguide to another. In the case of two suspended waveguides with triangular cross-sections, the coupling would be negligible. Right: when an auxiliary structure is in-between as shown above, the coupling between triangular waveguides can be enhanced.

works as a power splitter, an essential component in photonic circuits. In the following we consider suspended waveguides fabricated by angled etch. Supposing two stripes of hardmask are patterned, as shown in Fig. 5.18, on diamond surface close to each other with gap g and thickness t, if angled-etch from all directions takes place (with a cone-like Faraday cage, or with reactive RIE with sample rotation), there would be no material sandwiched between the resulting two waveguides. In contrast, if angled-etch happens only from the sides as illustrated in Fig. 5.18, provided that the etching is timed accurately, one could expect to obtain structures shown in Fig. 5.17 (right), where the diamond material in-between the waveguides could modify the mode field distribution, leading to enhanced evanescent coupling.
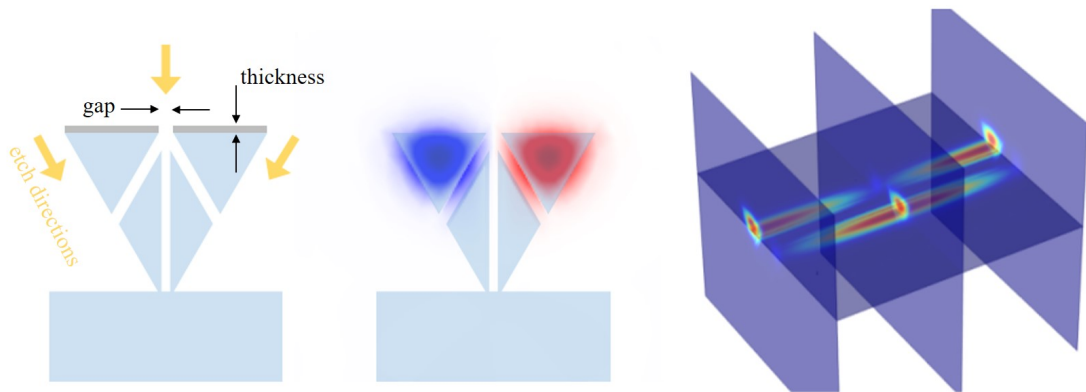
Figure 5.18 – Fabrication scheme of directional couplers and COMSOL simulation of mode distribution and mode beating along the propagation. The suspended waveguides need to be far away from the bulk substrate to avoid mode leaking into the bulk. In the right panel the propagation direction has a different scale than the cross-section plane as the beating length is much longer than the waveguide width. The unit of dimensions is omitted here as both the angled-etch process and Maxwell's equations scale linearly.
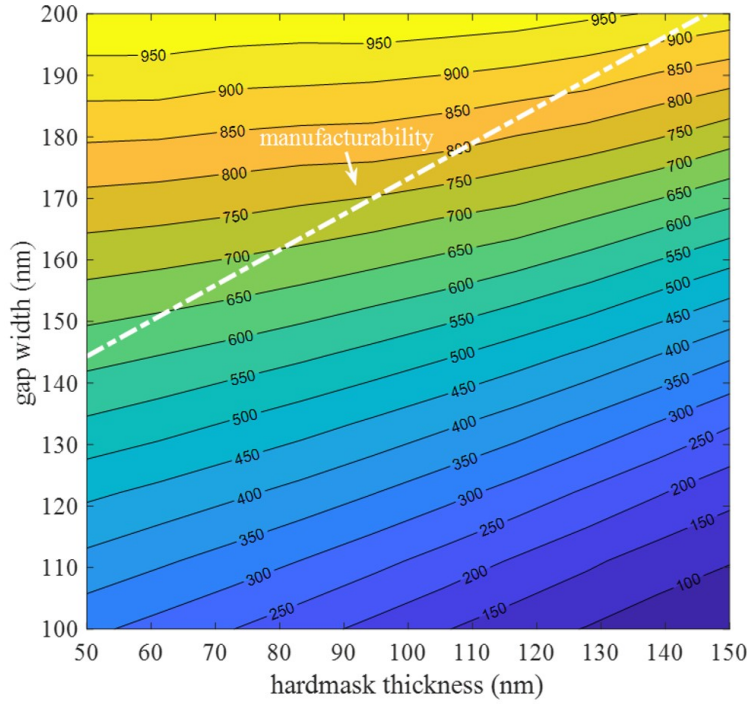
Figure 5.19 – Simulated half-beating length (unit: μm) depending on hardmask thickness and gap width for 1500 nm operating wavelength. The white dashed line corresponds to 100 nm inclined tunnel width in fabricated structures, beneath which the coupler is considered infeasible to fabricate.

We simulate in COMSOL the possible modes supported by the cross-section geometry shown in Fig. 5.18, and the anti-symmetric mode distribution is showcased. In our simulation where the etch-angle φ is fixed to 30 degrees with respect to substrate normal, the field distribution is well isolated from the substrate and we can safely assume the simulation results with a finite substrate size reliable (in our simulation the substrate width is taken as the same with the waveguides). Like conventional rectangular cross-section waveguides, the anti-symmetric mode shown above has a sibling symmetric mode with no phase difference across the symmetry plane, and a superposition of the two modes at 0 or π phase difference results in power flow (or mode excitation) in only one of the waveguides. As these two modes have different mode indices, the relative phase between them changes with propagation. Consequently, if only one waveguide port is excited, the field distribution transfers from one waveguide to another during propagation, and vice versa. The distance of propagation that it takes for the light to completely couple to the other waveguide and then to couple back is referred to as the beating length, and in Fig. 5.18 we show the simulated field distribution over the beating length when one of the ports is excited.

In Fig. 5.19 we plot the half-beating length against hardmask thickness and gap width, based

on simulations in COMSOL for 1500 nm operating wavelength [7]. A thicker hardmask results in shorter beating length as the inclined tunnel shown in Fig. 5.18 reduces, leading to stronger coupling. Denoting the tunnel width by w, we have $w = g\cos\varphi - t\sin\varphi$. This width cannot be infinitely small as the etch-rate is aspect-ratio dependent during fabrication. As can be seen from Chap. 5 and from Ref. [200, 199], 100 nm gap is possible to etch through, and we draw this line in Fig. 5.19 to indicate the manufacturability [8]. It is clear that even at this scale, hundreds of microns propagation is required for the power flow to completely transfer to another waveguide (*N.B.,* coupler with a quarter of the beating length works as a 50-50 power splitter). For comparison, we note that in Ref. [166] a directional coupler fabricated on DOI platform with rectangular cross-section and 420 nm gap has a (full) beating length about 350 μm when working at 1550 nm, which further accents the advantages of DOI platform.

---

[7]For simplicity we assume the hardmask has high selectivity against diamond, and its width and thickness do not change during fabrication. In reality this approximation can be compensated by layout design.

[8]An attempt to fabricate these devices with < 80 nm inclined gap was not successful, and we did not try to fabricate devices with a larger gap.

6 Fabrication and Characterization of Color Centers

The core ingredient that makes diamond a quantum photonics material is the color centers hosted therein. For synthetic substrates, they can be either incorporated *in situ*, *i.e.* during growth, or fabricated afterwards with laser, ion, or electron irradiation, with each of these methods having its pros and cons. In this chapter we first summarize the commonly employed methods to deliberately introduce color centers into diamond, following which the characterization results of implanted and CVD-grown color centers are presented. At cryogenic temperature, we observed photoluminescence spectra from ensemble SiVs in bulk substrate that, to our knowledge, have not been reported in literature, and we discuss about the difficulties in explaining the observations with established models.

6.1 A Survey on Color Center Fabrication

While a color center can be as simple as a vacancy in the carbon lattice (GR1 center [16]), most of them contain at least one atom other than carbon. Naturally, this requires doping either during growth or by implantation [1]. Below, an overview of common techniques for fabricating color centers is given, while it is to be noted that for different applications with various color centers, specific treatment, for instance isotopic engineering [210], can be expected for optimizing device performance. This is a vast topic and will not be covered in this chapter, and excellent review articles [211, 212] can be found in literature.

6.1.1 *In-situ* Growth

MPCVD growth of diamond typically involves at least gas phase CH_4 and H_2, while N_2 additive is also commonly employed as it has been found to improve the crystal quality and deposition rate [204, 213, 214, 215]. Usually the resulting diamond layer is not purely composed of carbon, and both Hydrogen [216] and Nitrogen [213] related defects can be present. Similarly,

---

[1]Diamond has a very densely packed lattice structure and doping by diffusion is extremely difficult, possible though [208, 209] for elements with small atomic size. However this is insufficient for producing varies color centers.

other materials in the CVD chamber can also be etched by the plasma and subsequently incorporated into the diamond layer. For example with the presence of nickel, NE8 centers have been observed in as-grown diamond [28, 217]. This is also true for the fabrication of group-IV related defects such as SiV, SnV and GeV centers [218, 219, 42]. By deliberately tuning the reaction chemistry and conditions [220], the concentration of resulting color centers can be controlled.

Color centers created by CVD growth show several advantages: a) they can be preferentially oriented [221], which is important for various applications such as quantum metrology [222]; b) high-quality color centers can be obtained, an example being record-long inhomogeneous spin-dephasing time ($T_2^* \approx 1.5$ ms) and Hahn-echo spin-coherence time ($T_2 \approx 2.4$ ms) very recently found for NV^- center in a phosphorus-doped CVD diamond [223], leading to better sensitivity in magnetic sensing; c) in the particular approach of *delta doping*, foreign atoms can be introduced into the diamond at a defined depth [224], and in combination with electron irradiation which we discuss later, positional control in 3D has been demonstrated [225] (Fig. 6.1).

In general, nevertheless, the impurities incorporated during CVD growth present random and relatively inhomogeneous distribution. Consequently, it can be more favorable to resort to ion implantation, laser- or electron- irradiation for device fabrication.

Similar to CVD doping, HPHT growth of diamond also incorporate impurities *in situ*. The foreign elements usually come from the environment (*e.g.* nitrogen) or from the solvent-catalyst (*e.g.* nickel) used to dissolve carbon, and at least at the present day, it is not feasible to have this process under precise control. Like the case in CVD growth, preferentially aligned NV centers have also been observed in HPHT grown diamond [226]. However quantitative engineering of color centers using this method has not been demonstrated to date.

6.1.2   Ion Implantation

Ion implantation is widely used in semiconductor manufacturing for introducing foreign atoms into host materials [227]. As described in Sec 5.1.1, depending on the kinetic energy, the accelerated ions gradually slow down and stop in the diamond at a depth that can be estimated by Monte Carlo simulation [126]. The energy transferred from energetic ions to target materials can distort the pristine sp^3 carbon crystal lattice structure, resulting in vacancies and carbon self-interstitials. On the other hand, the stopped ions either replace native carbon in the lattice forming substitutional impurities, or reside in an interstitial position. Right after implantation, the crystalline structure is usually heavily damaged, with GR1 signal generally observable indicating the creation of vacancies. To restore the crystallinity, post-implantation annealing [228] at high temperature (typically ranging from 800 to 1200 degrees Celsius) is commonly carried out, which also serves another purpose — to mobilize vacancies. The latter is especially important in forming impurity-vacancy complexes such as NV and SiV centers. It has also been found that HPHT annealing is able to narrow the emission linewidth of NV^- ensembles
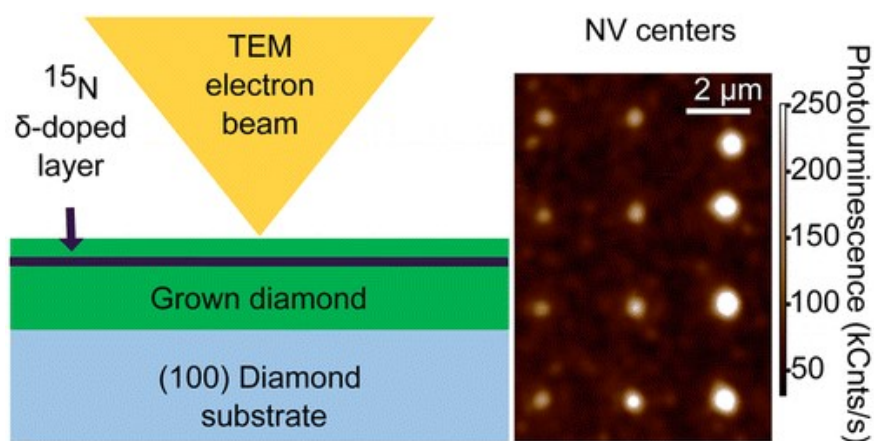
Figure 6.1 – By controlling gas supply during CVD growth, vertical positioning of impurities in grown diamond layer can be achieved by δ–doping. On the other hand, focused electron irradiation can be used for creating vacancies at defined horizontal position. The combination of the two techniques enables 3D positioning of NV centers. Reprinted from Ref. [225] with permission from ACS (the American Chemical Society).

[229] fabricated by implantation, which can be important for improving device performance.

The prominent advantage of ion implantation for creating color centers is the positional control. The incident position of impinging ions on the diamond surface can be controlled at nanometer precision, achieved by using focused ion beam [230], masks with nano-holes [231], or pierced AFM tips [232]. As already seen in Fig. 5.3, the depth distribution of the stopped ions is a function of their initial kinetic energy: higher implantation energies result in wider distribution thus less accurate positioning. This also holds true for lateral straggling. For example, nitrogen implanted with 2.5 keV acceleration energy can lead to 10 nm accuracy in three dimensions, while for 10 keV it is about 30 nm [233] (Fig. 6.2). As a result, direct high-energy ion implantation for precise positioning of color centers deep into the substrate is not possible. This can nevertheless be circumvented by low-energy implantation followed by overgrowth [233, 234, 235]. Quantitative control of defect density can also be achieved by tuning the implantation dose, while careful calibration is typically required to precisely control the outcome, as the conversion yield varies with experimental conditions [230, 236]. Electron and laser irradiation have been proved useful complementary techniques for improving the conversion yield, as will be discussed in the next subsections.

A caveat regarding ion implantation in single crystal materials is the channeling effects, which occur when ions travel along specific directions with respect to the crystal orientation, and has been shown to result in much extended stopped depths compared to Monte Carlo simulations [237]. While this can be easily avoided by aligning the crystal at a different angle, some disadvantages of ion implantation intrinsically limit its use for color center engineering. For example, a recent study [238] implanting ^{15}N into diamond with *in situ* nitrogen impurities
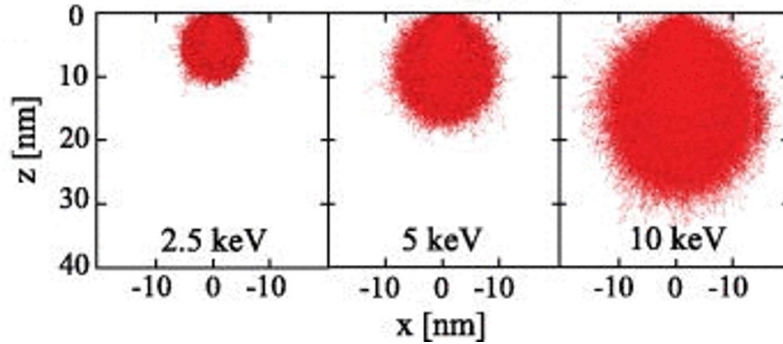
Figure 6.2 – The straggling range of implanted ions depends on their kinetic energy. SRIM simulation shows, that ^{15}N ions with 2.5 keV energy can be positioned into diamond substrates with 10 nm accuracy, while for 10 keV energy ions it becomes about 30 nm. Consequently, accurate positioning of deep color centers by ion implantation has to be accompanied by subsequent overgrowth. Reprinted from Ref. [233] with permission of AIP publications.

demonstrated that implantation-made NV$^-$ centers have drastically compromised optical coherence compared to their native counterpart, possibly owing to local lattice damage caused by implantation. SiV$^-$ centers on the other hand, have decent optical coherence when fabricated by implantation and annealing, both in bulk and in nanostructured diamond [239, 240]. This difference is due to the intrinsic atomic structures of various color centers and therefore depending on the final application, different technologies should be employed in order to achieve optimal device performance. Also to be noted is that ion implantation has so far remained elusive for creating certain defects, such as NE8 centers [241, 242], probably due to their more complex structures.

Implantation could also create impurity-vacancy complex in the absence of post-annealing: creation of NV$^-$ centers for instance, has been observed after swift heavy ion implantation [243]. It was suggested that electronic excitation and thermal spike were the responsible mechanisms, but further investigations are required to better understand this process.

6.1.3 Electron and Laser Irradiation

For a substrate with native impurities from growth, electron irradiation can be employed as an alternative method to create vacancies [121, 244], as it causes less lattice damage and is more accessible [2]. This approach has been demonstrated to increase the yield of SiV$^-$ [230] and NV$^-$ [244] centers following ion implantation, indicating that the conversion from implanted impurity to impurity-vacancy complex is bottlenecked by the amount of vacancies available. Similar to ion implantation, focused electron irradiation can be leveraged for fabricating color centers at designated positions [225]. Furthermore, electrons with MeV energy can travel

---

[2]The threshold for accelerated electrons displacing a carbon atom in the diamond lattice is about 150 – 170 keV [230, 245], which can be achieved in transmission electron microscopy facilities.

through diamonds of millimeter thickness and are therefore suitable for material modification of bulk substrates. In literature it has also been reported that electron irradiation with energy below the threshold for vacancy creation can promote the formation of NV$^-$ centers in a nitrogen-implanted sample [245], possibly due to electronic excitation related process.

Like electron irradiation and ion implantation, a pulsed laser can deliver the energy needed for color center formation as well. Rapid progress in this field has been made in recent years, showing great promise in terms of flexibility, quality and conversion yield [246, 247, 248, 249, 250]. Irradiating diamond substrates with intense laser pulse can create vacancies, evidenced by characteristic photoluminescence attributed to GR1 centers [248]. If native impurities such as nitrogen are present, NV$^-$ centers could form after annealing, and good optical coherence was observed [248]. It was also found that thermal annealing can be replaced by laser irradiation itself [249], in which case a first intense pulse is applied to create vacancies and a pulse train with lower energy follows to anneal diamond at the focus spot. A distinct advantage of this method is that one can observe the photoluminescence signal from the focus spot in real time, and only stop the laser annealing when the onset of NV$^-$ formation is observed. An impressive yield of 96% for creating single NV$^-$ centers was reported [249] with this approach. Furthermore, this method can be adopted easily to fabricate 3D arrays of color centers [250], showing much greater flexibility over other techniques.

Interestingly, a laser pulse is also capable of introducing foreign atoms into diamond subsurface. In 2013, Liu et al [247] demonstrated that femtosecond laser pulses are able to ionize molecules in air, resulting in free electrons which can be subsequently accelerated by following pulses towards the diamond surface. Vacancies can be created by these electrons and photoluminescence from NV$^-$ centers were observed after annealing. However, the starting material in this study was type Ib diamond which contains abundant nitrogen, and it was not clear if any nitrogen from air was implanted into the diamond. The same group reported later in 2019 the formation of SiV$^-$ centers with a similar method [246], with silicon nanoballs coated on a high-purity diamond substrate. This result unambiguously demonstrated that Si ions were accelerated by the laser pulse and incorporated into diamond. Despite the simplicity of this method, the laser pulses also damage the diamond surface via ablation, therefore its use for device fabrication is limited.

6.1.4 Charge State Control

Control over the charge state of color centers is of vital importance for any applications as physical properties thereof vary with not only chemical composition but also the charges. For example, NV centers exhibit ODMR (optically detected magnetic resonance) [251] only when negatively charged [222] and have been therefore extensively studied for magnetic sensing. In the case of SiV centers, spin coherence time of neutrally charged SiV^0 largely exceeds that of negatively charged SiV$^-$ [252], due to that total spin of 1/2 makes the latter prone to phonon-mediated, dynamic Jahn-Teller-like orbital relaxation [253]. Usually for the same

chemical composition such as NV and SiV complexes, defects with different charge states can co-exist, with a certain ratio between their concentration. This ratio can be modified by, for example, doping, in which case the Fermi level of diamond is altered, leading to preferential formation of a certain charge state. In 2016, Doi et al showed that in phosphorus-doped CVD diamond, steady state population of NV^- above 99% can be achieved under 593 nm illumination, leading to enhanced luminescence and improved magnetic sensing [254]. In boron-doped CVD diamond, more than 80% SiVs have neutral charge as the Fermi level was pinned to make SiV^0 have the lowest formation energy [252]. Doping by implantation instead of CVD growth manifests similar effects [255].

Without resorting to doping, annealing in dark was reported to convert SiV from neutral to negative charge state [256]. HPHT annealing at 8 GPa and 2000 °C was reported to increase the NV^-/NV^0 ratio by a factor of 5, but this is accompanied with an overall decrease in the NV count [229]. Further understanding on the interplay between color centers and donors/acceptors during annealing is required to have this process under control. For color centers distributed close to the surface (typically within hundreds of nanometers), the chemical termination of diamond surface may as well affect the charge state [255, 257, 258]. Beside these abovementioned passive engineering methods, active control of the charge state has been demonstrated by optical [259, 260] and electrical means [261].

6.2   SiV Centers Fabricated by Ion Implantation

To fabricate color centers, we acquired a high-purity CVD diamond substrate from Lake-Diamond SA. The as-received sample showed a sharp Raman peak at 1332 cm^{-1} and no photoluminescence (PL), indicating good crystalline quality and low impurity level.

The substrate was sent to Helmholtz-Zentrum Dresden Rossendorf (HZDR) for the implantation of Si^+ ions with a total dose of 4E13 cm^{-2}. To create a uniform SiV layer of about 200 nm thick immediately beneath the surface, 1.79E13 cm^{-2}, 1.29E13 cm^{-2} and 0.92E13 cm^{-2} of ions were implanted at 400, 289 and 200 keV acceleration energy, respectively, based on SRIM simulations (Fig. 6.3). The choice of implantation parameters is guided by the long-term plan for device fabrication with a layer of active medium whose thickness is comparable to the waveguide.

Another substrate, also acquired from LakeDiamond SA, that is HPHT grown and with very weak PL signal from NV^- was sent to Surrey University for a low-dose (nominally 1E9 cm^{-2}) implantation of Si ions, in order to create single color centers that can be optically addressed separately. This condition gives in average 10 silicon atoms in one square-micron, and taking into consideration the conversion yield well below 0.05 [230], we expect to have single SiV centers in an imaging voxel (about 1.5 μm deep and 400 nm wide) using a confocal microscope (Renishaw).

Both samples were annealed in high-vacuum at 1200 °C after implantation to mobilize vacan-
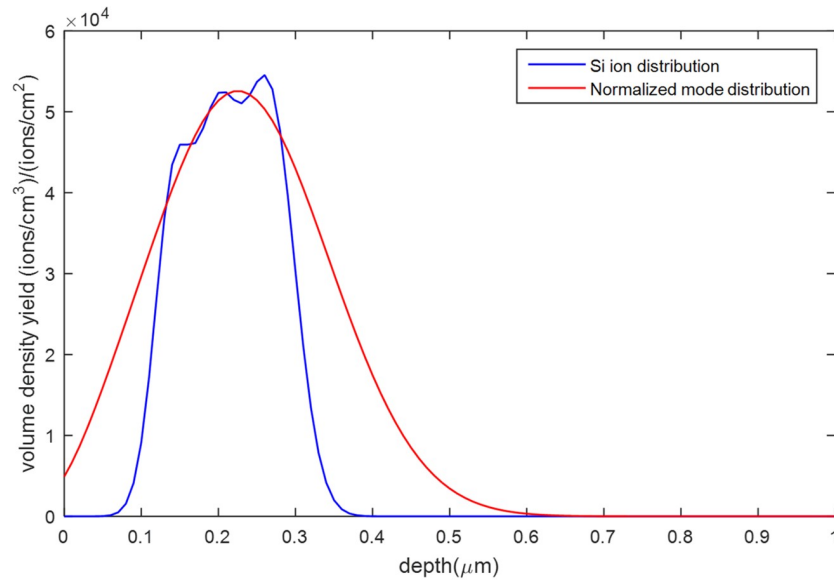
Figure 6.3 – Three successive implantations with 400 keV energy at dose of 1.79E13 cm^{-2} , with 290 keV at 1.29E13 cm^{-2} , and with 200 keV at 0.92E13 cm^{-2} . This recipe gives a reasonable overlapping (> 50%) between mode distribution and gain medium, with only three times of implanting.

cies, which are then trapped by silicon atoms, forming SiV color centers. This high-temperature treatment also allows the less damaged layer to recover its crystallinity. In Fig. 6.4 we show the PL spectrum of the sample with ensemble SiVs. While no PL was found prior to implantation,
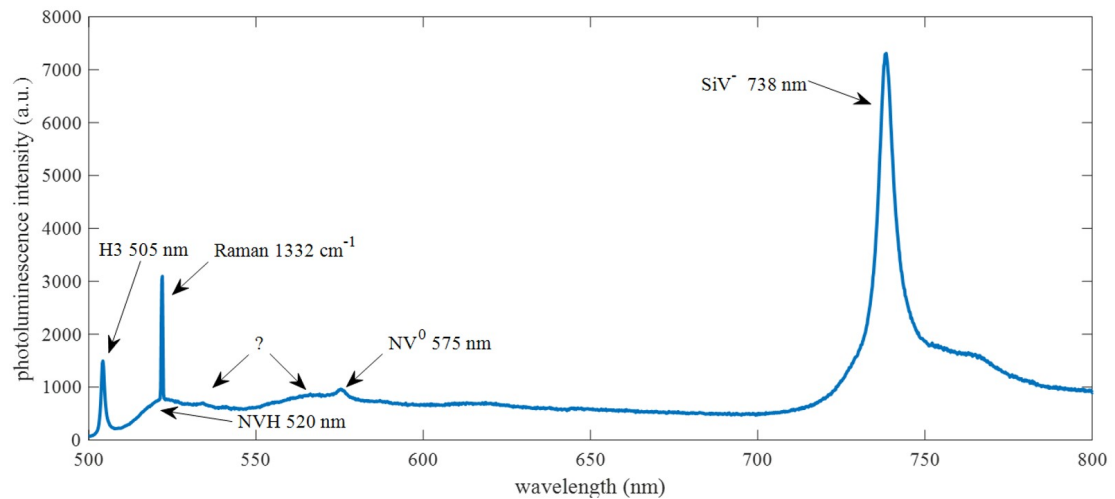
Figure 6.4 – Photoluminescence spectrum of ensemble SiVs created via ion implantation and high-temperature (1200°C) annealing. Pumping laser at 488 nm. Broad bands at 534 nm and 565 nm are of unclear origin.

we observe several nitrogen-related PL lines at 505 nm (H3 center), 520 nm (NVH complex [262, 263]), and 575 nm (NV^0) after implantation and annealing, indicating that native nitrogen impurities were present but they did not form NV complex before implantation. A weak band can be found around 534 nm whose position coincides with the Raman peak of nitrogen interstitial defects in diamond (1772 cm^{-1})[264], but the Raman signal should be much sharper and we cannot attribute this peak decisively. Another broad band around 565 nm is of unknown origin as well. No clear signal on the ZPL of NV$^-$ is found. The most prominent signal peaking at 738.6 nm is due to SiV$^-$ centers, with phonon sidebands extending above 800 nm.

6.3 Optical Characterization at Room Temperature

Apart from the abovementioned two samples, we also acquired a substrate from LakeDiamond SA that is CVD grown, with high brightness of PL signal from SiV$^-$ centers. Etching of quartz components in the growth chamber is believed to be the origin of their abundance. In this section we present data acquired from characterizing these samples and try to extract the emission and absorption cross-sections of SiV$^-$.

PL measurement was carried out with Renishaw confocal ramanscope using continuous-wave pump laser at 532 nm. The spectra were taken at increasing pump power and the acquired data was fitted to

$$I = \frac{P}{P + P_{sat}} I_\infty \tag{6.1}$$

with I_∞ indicating the saturation count and P_{sat} the saturation power. This measurement was not possible for single defects due to insufficient collection efficiency of the setup (only at high pump power could we observe the PL, yet with low-power excitation, long-time acquisition was not feasible due to stage drifting). For the same reason, we could not perform HBT (Hanbury Brown-Twiss) measurement for verifying single photon emission. Instead,

Table 6.1 – Photoluminescence characterizations of SiV center at room temperature.

	PL peak (nm)	linewidth (nm)	saturation (1/s)	lifetime (ns)
CVD, ensemble	738.2	4.5	6E5	1.13
implantation, ensemble	738.6	5.5	5E4	0.35
implantation, single	738	3.88	\\$^\dagger$	\\$^\dagger$

Note: † The measurements were carried out using shared facilities whose collection efficiency was limited and we could not modify the setup. For saturation measurement, as only at maximum pump laser power can the PL signal from single SiV be observed, we could not calculate the saturation intensity. For measuring the excited state decay, the collection efficiency of the setup was not sufficient for locating the single defects.
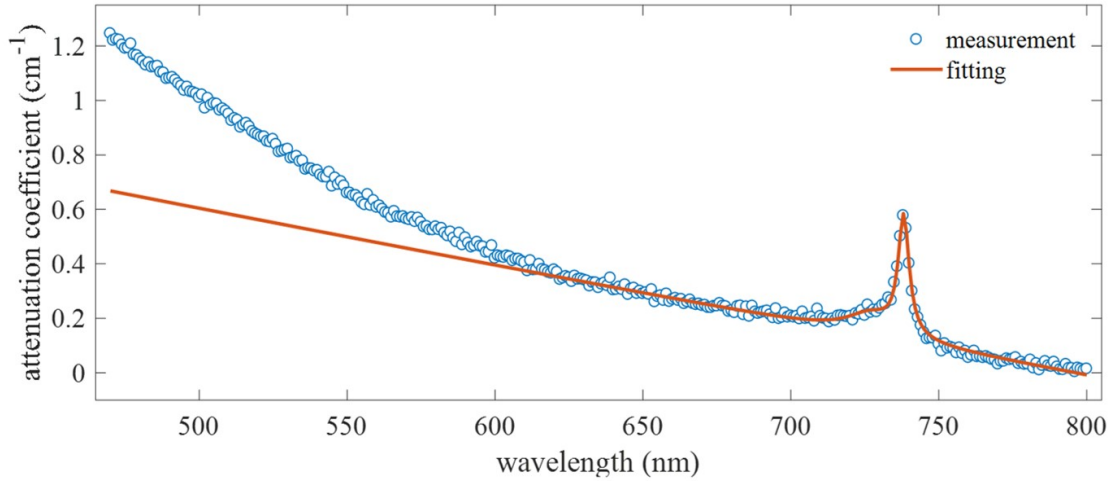
Figure 6.5 – Absorption spectrum of the diamond sample with ensemble SiVs grown by CVD, taken at 300K. The spectrum was fitted with a Lorentzian (for ZPL) and a Gaussian (for sideband), plus a linear background.

we measured multiple isolated SiV$^-$ sites and most of them show similar intensity (with few having doubled intensity), which is consistent with the fact that the substrate is (100) oriented and SiV$^-$ aligns with <111> directions, *i.e.* signal collected from all single SiV$^-$ centers should be of similar intensity.

In Table. 6.1 we list the PL characterization results, from which we can calculate the emission cross-section according to

$$\sigma = \frac{\beta\eta\lambda^2}{8\pi n^2\tau_{fl}\Delta\nu}$$

(6.2)

where β is the ZPL branching ratio, η quantum efficiency, λ wavelength, n refractive index, τ_{fl} fluorescence decay time, and $\Delta\nu$ linewidth. The quantum efficiency cannot be obtained from PL spectra and we take a conservative estimation by assuming $\eta = 0.05$. The calculated emission cross-section for implanted (CVD-grown) SiV ensemble is 1.35E-15 (5.1E-16) cm^2.

The short excited state lifetime of the SiVs in the implanted sample agrees with its broadened PL linewidth. The fast decay can be attributed to more non-radiative decay paths in a damaged crystal, or ionization of SiV$^-$ into SiV^0. It was reported that NV$^-$ centers decay at a much faster rate [265] if electrons tunnel to adjacent acceptors. In the case of a highly damaged crystal, some defects may also trap electrons, such as a neutral vacancy [266] which is abundant after implantation.

To quantify the emitter density, a commonly used method is to compare the PL intensity from an ensemble with that from a single emitter. However, since we were not able to measure the decay time of a single SiV$^-$ center, this approach is not applicable here, as $I \propto N/\tau$ and we do not have τ for single SiV$^-$.
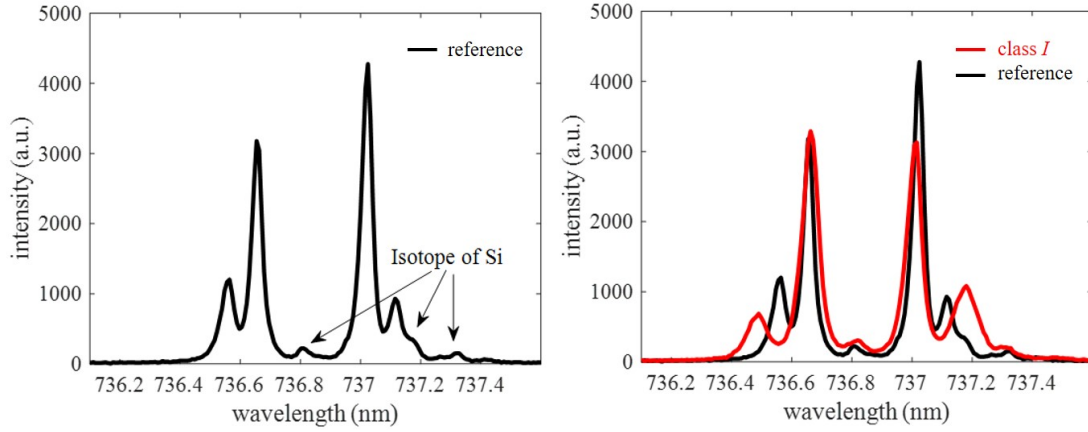
Figure 6.6 – *Class. I*: (left) PL spectrum from ensemble SiV⁻ that is similar to the PL from single color centers, except the broadened lines; (right) frequency shifting of transitions, but with no additional splitting.

Alternatively, one can estimate the SiV⁻ density from absorption spectrum taken at liquid nitrogen temperature [256]. We used a shared facility (Cary 500) which works only at room-temperature to measure the absorption spectrum of the CVD grown diamond, result shown in Fig. 6.5. To account for the difference between data acquired at 300K and at 77K, we assume a factor of 2.2 ($\text{Abs}_{77K} = 2.2 \times \text{Abs}_{300K}$) is reasonable based on the observation for temperature-dependent absorption in Ref. [267]. With this assumption, the density of SiV⁻ centers is estimated to be $\sim$ 6E15 cm⁻³. From $\alpha = N \cdot \sigma_{abs}$ where N is the density of SiV⁻ centers and α the attenuation coefficient at 738 nm, we immediately have $\sigma_{abs} \sim$ 8E-17 cm² at ZPL under room-temperature.

6.4 Photoluminescence at Cryogenic Temperature

The CVD grown sample with abundant ensemble SiV⁻ was further investigated at liquid Helium temperature. This setup is not confocal and the 100X objective focuses the 532 nm pump laser onto a $\sim$ 1 μm spot. The PL signal is collected through a fiber into a spectrometer (Andor Shamrock 750). Beside the typical four-line splitting of ZPL due to spin-orbital coupling, several types of PL spectra that, to our knowledge, were not reported in literature were recorded. In the following we present the data and contrast our observations to the theory of strain-induced electronic structure modification.

6.4.1 Anomalous Photoluminescence Spectra

The PL spectra from SiV-containing nanodiamond particles and diamond nanostructures are known to be sensitive to the defects' strain environment [268, 269], leading to highly inhomogeneous distribution of ZPL lines. In bulk substrates, this inhomogeneity manifests
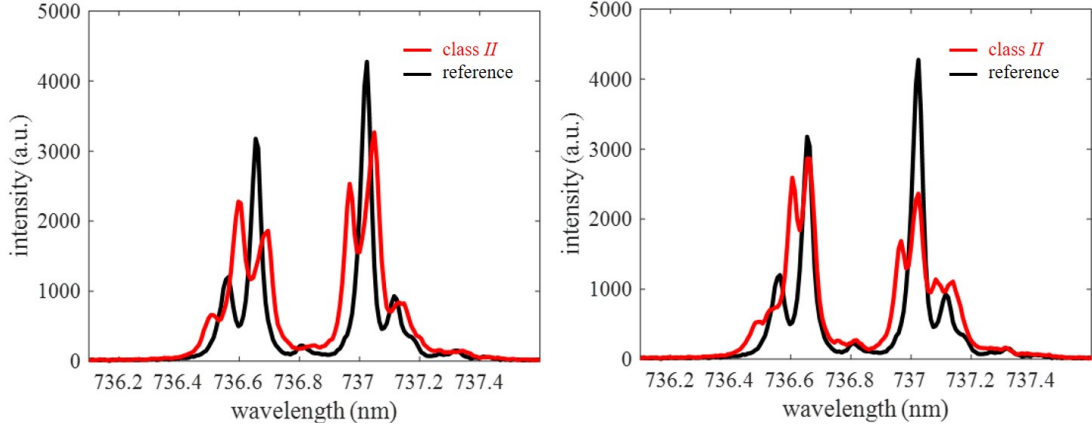
Figure 6.7 – *Class. II*: Clear line splitting for the two bright transitions (left) and for all four transitions (right).
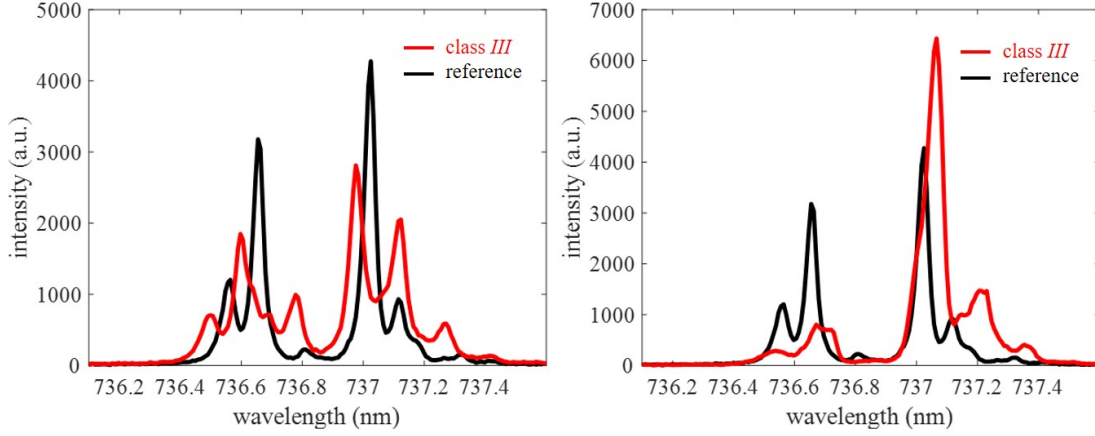
Figure 6.8 – *Class. III*: Complicated line splitting for the transitions A and B (left) or C and D (right) with at least five peaks identifiable.

itself as broadened transitions. However, in our sample, we observe not only broadening, but also frequency splitting of broadened lines. Typical observations recorded at different sites can be categorized into three classes and are presented in Fig. 6.6 – 6.8. The spectrum shown in Fig. 6.6 (left) is taken as a reference for visual guidance. All PL measurements were carried out at 4K on the same sample at randomly chosen sites.

6.4.2 Strain-field Modified Electronic Structure

Strain-fields are known to be able to modify the electronic structures of point defects [35, 270], leading to enlarged energy-level splitting. For SiV$^-$ centers, a schematic of this effect is shown in Fig. 6.9. With $\left|e_{x(y)}\right\rangle$ and $\left|\downarrow(\uparrow)\right\rangle$ denoting the orbital and spin eigenstates respectively, a
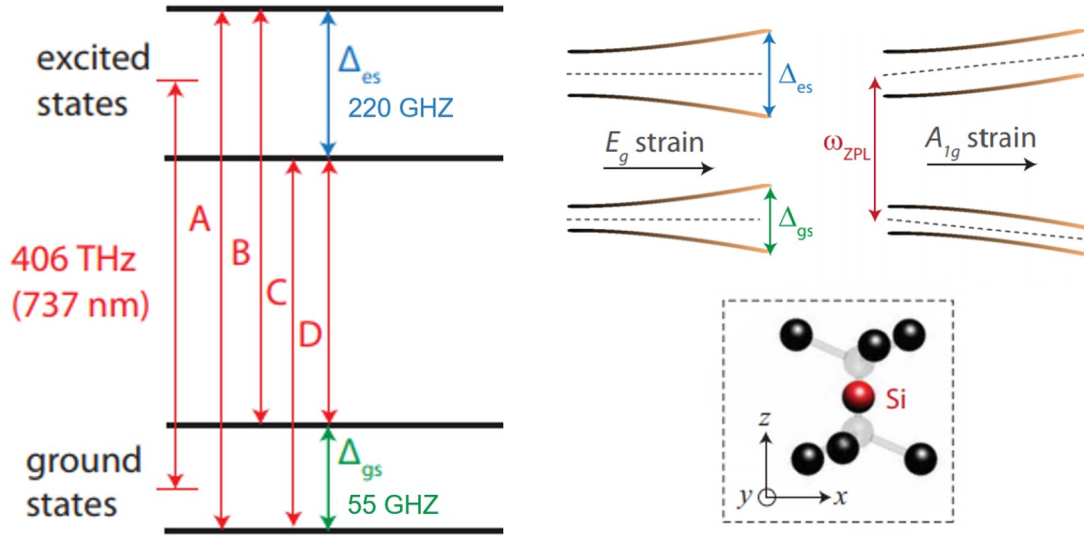
Figure 6.9 – Electronic structure of the SiV⁻ center and its dependency on strain field. The E_g (A_{1g}) symmetry related strain is defined in the main text. A, B, C, D transitions correspond to the four bright lines in reference spectrum in Fig. 6.6 – 6.8. Adapted from Ref. [35] with the permission of APS (the American Physical Society).

group-theoretic analysis reveals [35] that the strain Hamiltonian in $\{|e_x \downarrow\rangle, |e_x \uparrow\rangle, |e_y \downarrow\rangle, |e_y \uparrow\rangle\}$ basis can be expressed as

$$
\mathbb{H} = \begin{bmatrix}
\epsilon_{A_{1g}} - \epsilon_{E_{gx}} & 0 & \epsilon_{E_{gy}} - i\lambda_{SO}/2 & 0 \\
0 & \epsilon_{A_{1g}} - \epsilon_{E_{gx}} & 0 & \epsilon_{E_{gy}} + i\lambda_{SO}/2 \\
\epsilon_{E_{gy}} + i\lambda_{SO}/2 & 0 & \epsilon_{A_{1g}} + \epsilon_{E_{gx}} & 0 \\
0 & \epsilon_{E_{gy}} - i\lambda_{SO}/2 & 0 & \epsilon_{A_{1g}} + \epsilon_{E_{gx}}
\end{bmatrix},
$$

where λ_{SO} is the spin-orbital coupling strength within GS or ES manifold (from the reference spectrum in Fig. 6.6, we use $\lambda_{SO,gs} = 55$ GHz and $\lambda_{SO,es} = 220$ GHz for further analysis), and $\epsilon_{A_{1g}(E_{gx}, E_{gy})}$ refers to the strain associated with $A_{1g}(E_{gx}, E_{gy})$ symmetry, defined as $\epsilon_{A_{1g}} = t_\perp(\epsilon_{xx} + \epsilon_{yy}) + t_\parallel \epsilon_{zz}$, $\epsilon_{E_{gx}} = d(\epsilon_{xx} - \epsilon_{yy}) + f\epsilon_{zx}$, $\epsilon_{E_{gy}} = -2d\epsilon_{xy} + f\epsilon_{yz}$, with $t_{\perp(\parallel)}, d, f$ being strain-susceptibility parameters and ϵ_{ij} being strain components in the local Cartesian coordinate (c.f. Fig. 6.9), respectively. The Hamiltonian can be diagonalized to derive

$$\Omega_{ZPL} = \Omega_{ZPL}^0 + (t_{\parallel,es} - t_{\parallel,gs})\epsilon_{zz} + (t_{\perp,es} - t_{\perp,gs})(\epsilon_{xx} + \epsilon_{yy}), \tag{6.3}$$

$$\Delta_{gs} = \sqrt{\lambda_{SO,gs}^2 + 4[d_{gs}(\epsilon_{xx} - \epsilon_{yy}) + f_{gs}\epsilon_{yz}]^2 + 4(-2d_{gs}\epsilon_{xy} + f_{gs}\epsilon_{zx})^2}, \tag{6.4}$$

$$\Delta_{es} = \sqrt{\lambda_{SO,es}^2 + 4[d_{es}(\epsilon_{xx} - \epsilon_{yy}) + f_{es}\epsilon_{yz}]^2 + 4(-2d_{es}\epsilon_{xy} + f_{es}\epsilon_{zx})^2}, \tag{6.5}$$

where Ω_{ZPL}^0 denotes the base ZPL transition frequency. Consequently, we can express the frequencies of four transition lines separately as

$$\Omega_A = \Omega_{ZPL} + (\Delta_{es} + \Delta_{gs})/2, \quad \Omega_B = \Omega_{ZPL} + (\Delta_{es} - \Delta_{gs})/2,$$
$$\Omega_C = \Omega_{ZPL} - (\Delta_{es} - \Delta_{gs})/2, \quad \Omega_D = \Omega_{ZPL} - (\Delta_{es} + \Delta_{gs})/2.$$

If the SiVs all align along the same direction, the spectra of *Class. I* can be easily explained by a strain-field modified electronic structure, since we have 6 variables (ϵ_{ij}) and only 3 independent equations 6.3 – 6.5. However, the crystal we characterized was grown on (100) plane and no preferential alignment should exist [271]. In fact, no polarization preference was found during PL measurement, consistent with the theoretical prediction. In principle, as the SiVs should align with any one of the four <111> directions with same probability, a random strain field should always induce complicated splitting features due to lack of symmetry. In fact, according to the structure of diamond lattice, only when the strain field is along one of the <100> directions should one observe no additional splitting. Such a field with amplitude 0.001 in the unit cell (Fig. 2.1) and SiV local (Fig. 6.9) coordinates can be expressed as

$$S_{001} = \begin{bmatrix} 0.001 & 0 & 0 \\ 0 & 0 & 0 \\ 0 & 0 & 0 \end{bmatrix}, S_{001}^{local} = \begin{bmatrix} 0.1670 & -0.1670 & 0.4716 \\ -0.1670 & 0.1670 & -0.4716 \\ 0.4716 & -0.4716 & 1.3322 \end{bmatrix} \cdot 0.001,$$

respectively, with $S_{001}^{local} = R_{011}^T(35.3°) \cdot R_{100}^T(45°) \cdot S_{001} \cdot R_{100}(45°) \cdot R_{011}(35.3°)$ where R matrices

$$R_{100}(45°) = \begin{bmatrix} cos(45°) & -sin(45°) & \\ sin(45°) & cos(45°) & \\ & & 1 \end{bmatrix},$$

$$R_{011}(35.3°) = \begin{bmatrix} 1 & 1 - cos(35.3°) & sin(35.3°) \\ 1 - cos(35.3°) & 1 & -sin(35.3°) \\ -sin(35.3°) & sin(35.3°) & cos(35.3°) \end{bmatrix},$$

represent rotations in 3D. With strain susceptibilities determined in Ref. [35] being $d_{gs} = 1.3$, $d_{es} = 1.8$, $f_{gs} = -1.7$, $f_{es} = -3.4$, $t_{\parallel,es} - t_{\parallel,gs} = -1.7$, $t_{\perp,es} - t_{\perp,gs} = 0.078$ (dimension – PHZ per strain), we can calculate $\Delta\Omega_{ZPL} = -1.0834$ GHz, $\Delta_{gs} = 1.6095$ GHz and $\Delta_{es} = 3.3147$ GHz. In Fig. 6.6 the GS splitting almost doubled, and if strain field were the cause for enlarged splitting, the above calculation suggests that a strong red shifting of ZPL should have been observed. Such inconsistency implies that there should be other mechanisms that are affecting the electronic structures of ensemble SiVs. Besides, if we assume the strain field is random, then statistically we should observe more often complicated splitting features resembling those in *Class. III* spectra. Again this is opposite to our observations where *Class. I* spectra were more frequently encountered. Further spectroscopic techniques such as photoluminescence excitation spectroscopy and pump-probe detection might be of help in better clarifying the origin of these anomalous spectra.
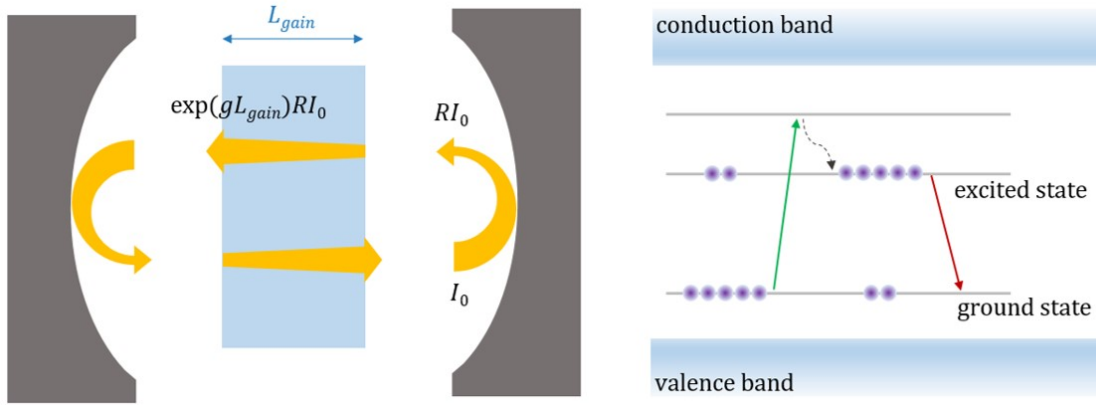
Figure 6.10 – Left: symmetric FP cavity with mirror reflectivity R and gain coefficient g. With $exp(gL_{gain})R > 1$, intracavity circulating light would be amplified in each round-trip. Right: at room-temperature, the spin-orbit splitting of ES (excited state) and GS (ground state) manifolds of SiVs is narrower than their homogeneous broadening, resulting in one ES and one GS level. Under optical pump, the electrons are excited to an energy level above ES and relax to ES via non-radiative channels, followed by radiative decay (emission of a photon at ZPL) to GS.

6.5   Possibility on Lasing

Heterogeneous integration [272, 273] of active media is currently the prevailing technology for integrating source components on a silicon photonics circuit, not only because the indirect bandgap of silicon results in low emission efficiency, but also due to the hetero-integration approach provides more diverse choices on wavelength. The various color centers held in diamond could potentially provide similar possibilities, and early works [274, 275, 276, 277, 278, 279] have demonstrated diamond lasers with H3 centers being the active media feasible. If they can be realized, integrated color center lasers would further enable fully functional diamond PIC for sensing and quantum information applications. Nevertheless, recent attempts towards a diamond laser [29, 280] with NV$^-$ centers have not been successful[3], with photo-ionization being a possible obstacle [280]. For SiV$^-$ centers, photo-ionization has also been observed [282], but it has been shown [283] that a 532 nm pump laser can help circumvent this problem. In the following we discuss about the possibilities in realizing a SiV$^-$ laser based on the data we obtained from the aforementioned sample.

6.5.1   Threshold Conditions for Three-level Lasing

The working principle of lasers is explained in numerous textbooks [284, 285, 286]. In the following we follow Ref. [285] to model the lasing condition.

---

[3]A preprint claiming NV$^-$ lasing was published on arxiv in March 2021 [281].

The essential components for lasing are a cavity which provides coherent feedback and a gain medium which enables amplification of the light [4]. As shown in Fig. 6.10, photons circulate inside the cavity, where loss mechanisms such as non-unity reflection efficiency attenuate the intensity, and gain medium, *i.e.* diamond with SiV$^-$ centers in our case, provides coherent amplification due to stimulated emission along the propagation of the light. SiV$^-$ centers have energy levels residing in the bandgap of diamond [289, 290]. Under equilibrium, the electrons mainly possess the ground state following Boltzmann distribution, and resonant photons (frequency matching the transition between ground and excited states) passing through such SiV$^-$ centers would manifest net absorption. A pump source such as a non-resonant laser has to be employed to prepare the electrons into the excited state via the dynamics shown in Fig. 6.10, resulting in population inversion of electrons. Resonant light passing through such a medium would experience net gain via stimulated emission, with its amplitude growing coherently.

In theory, as long as the gain can be made larger than the loss within a cavity round-trip, lasing is possible. In experiment, nonetheless, several conditions needs to be taken into consideration. With a given gain medium, the maximum gain coefficient theoretically achievable is set by the density of the emitters as $g_{max} = N_t \cdot \sigma_{em}$, where σ_{em} is the emission cross-section, and N_t the total density of emitters. This maximum value, however, is never reached in practice as only the emitters with electrons pumped up to the excited state can emit photons. The actual gain coefficient is determined by the pumping condition and can be derived following rate equations [285] as [5]

$$g = \frac{P - \Gamma}{P + \Gamma} g_{max},$$
(6.6)

where P is the pumping rate from the ground to the excited state, and $\Gamma \equiv 1/\tau$ the decay rate of the reverse process. On lasing threshold, the gain coefficient is equal to the unit-length overall loss

$$g = \mathscr{L}/(qL_{gain})$$
(6.7)

with $\mathscr{L} \equiv -\sum_i lnR_i$ where R_i represents individual loss mechanisms such as transmission, reflection, scattering and absorption loss *etc.*, and L_{gain} the length of the gain medium as indicated in Fig. 6.10, q a pumping scheme dependent factor, accounting for single- or double-pass pumping ($q = 1$ or 2, respectively). For 3-level lasers, the threshold power density for lasing is given by $P_{th} = \hbar\omega P\Gamma N_t/(P+\Gamma)$ [285] with $\hbar\omega$ being the photon energy of the pumping source (assuming a monochromatic laser is used for optical pumping). In combination with Eq. 6.6 we have then

$$P_{th} = \frac{\hbar\omega\Gamma}{2}[N_t + \frac{\mathscr{L}}{q\sigma_{em}L_{gain}}],$$
(6.8)

where all physical quantities except $\mathscr{L}$ in Eq. 6.8 can be measured or estimated from our previous characterizations, and $\mathscr{L}$ depends on the cavity design which we discuss in the next

---

[4]Cavityless lasers have also been demonstrated where coherent feedback is provided other than by a cavity [287, 288]. These mechanisms are, nevertheless, not suitable for our current case.

[5]In Ref. [285] the equation is derived assuming same degeneracy of the excited and ground states, which coincides with the case of SiV$^-$ centers, as shown in Fig. 6.9.
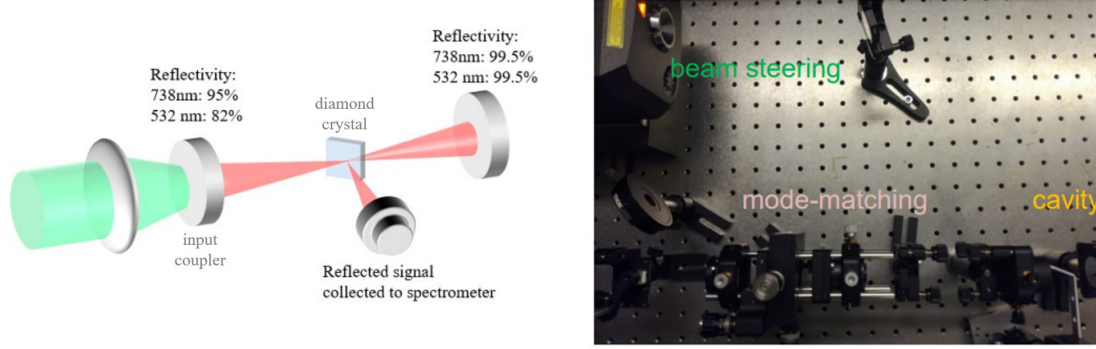
Figure 6.11 – Fabry–Pérot cavity with bulk optics. The input coupler is partially reflective to allow build-up of both pump laser and SiV$^-$ emission. In the right panel we show an example setup we built with a cavity length slightly less than 50 mm.

sub-section. Note that this expression is the power density required to be absorbed by the SiV$^-$ centers, which is different from the actual power of the source by a factor of absorption efficiency, and we have assumed that a pumping photon has unit probability in relaxing nonradiatively to the excited state.

6.5.2   Fabry–Pérot Cavity with Bulk Optics

In section 6.3 we estimated the ZPL emission and absorption cross-section for SiVs in the CVD sample to be 5.1E-16 cm^2 and 8E-17 cm^2 respectively, and the density of SiVs to be ~ 6E15 cm^{-3}. From Fig. 6.5 we also have the absorption coefficient of 532 nm pump for our 1 mm thick CVD sample about 0.8 cm^{-1}. If we assume that no other mechanisms (*e.g.* ionization [282], photobleaching/blinking [291], laser-induced etching of diamond [292], *etc.*) are prohibiting lasing transition, we can estimate the laser threshold with a given cavity and pumping scheme. In the following, we consider a Fabry–Pérot (FP) cavity with the diamond plate place at the mode waist with Brewster angle configuration, as sketched in Fig. 6.11. The choice of this arrangement is due to that after polishing of the CVD sample, a wedge about 10 arc min was estimated from the distance between laser beams reflected from the two polished surfaces, with which a normal-incidence pumping scheme would accompany significant loss (>35% solely due to Fresnel reflection) in a single round-trip in the cavity.

To facilitate lasing, the cavity design should allow tight focus of the pumping laser. For the fundamental cavity Gaussian mode (TEM$_{00}$), the mode waist and the beam radius on the coupler in a symmetric FP cavity are expressed as [285]

$$
\begin{aligned}
w_{waist} &= (\lambda L/2\pi)^{1/2}[(1+g)/(1-g)]^{1/4}, & (6.9) \\
w_{coupler} &= (\lambda L/\pi)^{1/2}[1-g^2]^{-1/4}, & (6.10)
\end{aligned}
$$
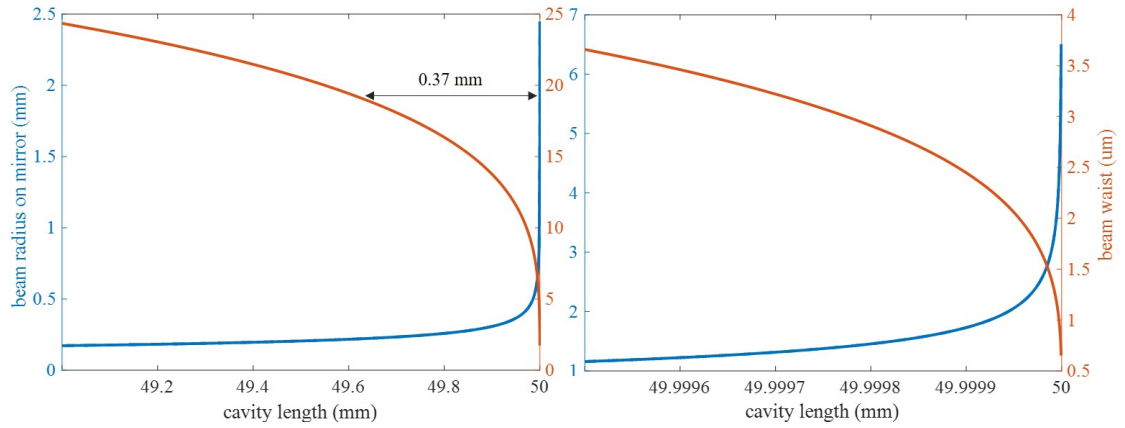
Figure 6.12 – TEM_{00} mode waist and beam radius on the mirror depend on the cavity length. The cavity consists of two concave mirrors with radius curvature 25 mm. For a diamond (n=2.4) plate placed at Brewster angle, the effective cavity length for orthogonal transverse directions has a difference $d\sqrt{1+n^2}(1/n^2 - 1/n^4)$ where d is the plate thickness [293]. In our case this is 0.37 mm as indicated on the left panel, leading to a minimum achievable spot size on one transverse direction to be about 20 μm. On the right, one can see that when the cavity length approaches the limit, the beam radius on the mirror becomes comparable to the optics aperture.

where $g = 1 - L/R$, with L and R being the cavity length and the radius curvature [6] of mirrors, respectively. For the laser cavity to be stable, *i.e.* the intracavity light is not scattered out within a few round-trips, $|g| < 1$ is required [285]. While in theory the mode waist can be made infinitely small if the cavity length is tuned infinitely accurate towards $g \to -1$ ($L \to 2R$), in practice this is infeasible both due to that the limited positioning accuracy and that the beam radius on the coupler would become comparable or even larger than the aperture (commonly used optics have a diameter from 12 mm to 50.8 mm) as shown in Fig. 6.12. Furthermore, with the diamond plate placed at Brewster angle, the effective cavity-length difference caused by astigmatism gives rise to ellipticity of the cavity mode profile, limiting the achievable spot size (Fig. 6.12). Consequently, a doubly-resonant cavity design would be favored for easing the requirement on pump power, where build-up of both the pump laser and the SiV^- emission are permitted.

On resonance, *i.e.* for wavelength λ with $m \cdot \lambda = 2L_\lambda$ where m could be any non-zero integer and L_λ is wavelength-dependent due to dispersion of light in the gain medium and at optical surfaces, the build-up factor in the abovementioned scheme is expressed as $\Sigma = \left| t_1/(1 - r_1 r_2 t_{gain}^2) \right|^2$ with t_1 (t_{gain}) being the amplitude transmissivity of the input-coupler (gain medium), and $r_{1(2)}$ the amplitude reflectivity of the input-coupler (the second mirror). If we assume no scattering loss, the build-up factor would be a function of three

---

[6]L is the length of optical path with non-unity refractive index taken into consideration wherever applicable, and R is positive (negative) for concave (convex) mirror.

Table 6.2 – Summary of parameters for calculating the lasing threshold

Parameter	Value	Source
N_t	6E15 cm^{-3}	Sec 6.3
σ_{em}	5.1E-16 cm^2	Sec 6.3
$g_{max} = N_t\sigma_{em}$	3.06 cm^{-1}	Table 6.2
P	1.67 $\Gamma \approx$ 1.478 GHz	Table 6.1, Eq. 6.7
$g = g_{max}(P-\Gamma)/(P+\Gamma)$	0.7679 cm^{-1}	Table 6.2
$\hbar\omega$	3.7338e-19 J	photon energy at 532 nm
$P_{th} = \hbar\omega\Gamma(N_t + g/\sigma_{em})/2$	1.24 MW/cm^{-3}	Eq. 6.7, Eq. 6.8, Table 6.2
α (738nm)	0.585 cm^{-1}	Fig. 6.5
α (532nm)	0.8 cm^{-1}	Fig. 6.5
R_1 (738 nm)[†]	0.95	Sec. 6.5.2
R_1 (532 nm)[†]	0.82	Sec. 6.5.2
R_2 (532 nm and 738 nm)[†]	0.995	Sec. 6.5.2

Note: [†] We assume the mirrors are lossless, *i.e.* $R + T = 1$. In experiment this is never true, but in the calculation of the threshold, this contribution is counted by assuming a large Θ.

variables $(r1, r2, \Theta)$ with Θ indicating the offset of the diamond plate relative to the ideal Brewster angle (which is never possible for two wavelengths because of dispersion), and the optimal combination can be found with numerical optimization. In practice, however, the availability of optics has to be taken into consideration. In our case, a custom input-coupler was ordered from Laseroptik GmbH with highly (partially) reflective coating for 738 nm (532 nm) with reflectivity 95% (82%), and a standard Thorlabs concave mirror with high-reflection dielectric coating ($\sim$ 99.5% for both wavelengths) was used as the second mirror. In the following we assume misalignment $\Theta = 4°$ which is unlikely to happen but can be seen as a lumped lossy channel accounting for loss mechanisms that have been so far neglected, such as scattering and non-perfect mirrors. The round trip loss $\mathscr{L}$ is then $-ln(R_1 R_2 T_{gain}^2)$ where $R_i = r_i^2$ represents the reflection of the mirrors, and $T_{gain} = t_{gain}^2$ the transmission through the sample.

For SiV$^-$ emission wavelength, we consider the loss and gain in the gain medium separately, *i.e.*, the transmissivity through gain medium is determined by reflection loss and absorption, without taking into consideration the re-emission. In Table. 6.2 we recall the parameters estimated in previous sections which are needed in the following estimation. In calculating $\mathscr{L}$, we
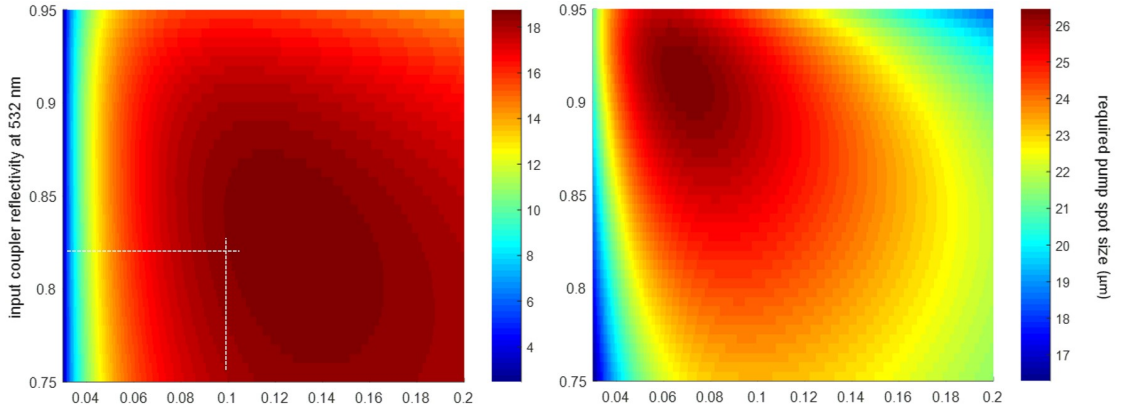
Figure 6.13 – Required pump focus in the case of $\Theta = 6°$ (left), *i.e.* corresponding to more loss in the cavity, and of $\Theta = 4°$ (right). The reflectivity at 532 nm for the input coupler was chosen to be ~ 0.82 because in the higher loss scenario this choice gives a less stringent requirement on focus tightness (sample thickness 1 mm), while with lower cavity loss, the difference on the focus spot between 0.82 and 0.92 reflectivity is only about 1 μm.

have $t_{gain} = t_{b1} t_{b2} exp(-\alpha_{738} L_{gain} \Gamma/(P+\Gamma)/2)$ where t_{bi} is the transmission coefficient of the ith interface (function of Θ, calculated from Fresnel equation [294]), and with $gqL_{gain} = \mathscr{L}$ we can solve for $P \sim 1.67\,\Gamma$ when $\Theta = 4°$. Note that here the attenuation coefficient due to absorption is $\alpha\Gamma/(P+\Gamma)/2$, where electron population inversion is taken into consideration, and the factor of $1/2$ accounts for the square-root relation between the power and the field amplitude. Then P_{th} is estimated by Eq. 6.8 to be ~ 1.24 MW/cm^{-3}. With this cavity configuration and a 1 mm thick diamond plate, about 5.6% power can be absorbed by SiV$^-$ centers in a round-trip [7], therefore 22 MW/cm^{-3} intracavity power density is required.

A 5W continuous-wave 532 nm laser is available to us for pumping, and the abovementioned cavity gives a build-up factor ~ 8.5 for the pump wavelength. If perfect mode-matching can be achieved, *i.e.* if all power can be coupled to the cavity mode, we would need to focus the pump laser to $\sim 25\,\mu m$ waist (since the diamond thickness is smaller than the Rayleigh length of the TEM$_{00}$ cavity mode, we can consider the laser-pumped volume as a cylinder of ~ 1 mm length) to achieve the threshold power density, with a mm-size spot on the end mirrors, much smaller than the aperture. In Fig. 6.13 we plot also the required pump focus spot to achieve the estimated power density threshold as a function of sample thickness and input-coupler reflectivity at 532 nm. It can be seen that the choice of 0.82 reflectivity at pump wavelength allows larger focus in a more lossy cavity, and further thinning down the sample does not bring significant advantage. To conclude, at least in theory, if all assumptions we have made so far hold true, it should be possible to make diamond lase with SiV centers.

---

[7]The absorption efficiency through the sample alone is $\eta = 1 - exp(-\alpha_{532} L_{gain} \Gamma/(P+\Gamma))$ but by taking into consideration the finite transmission at the diamond-air interface and the reflection loss at the mirror, for a round-trip in a FP cavity the total absorption efficiency is $t_{b1}^2 \eta(1 + (1-\eta) t_{b2}^4 r_2^2)$ where r_2 is the reflection coefficient for 532 nm at the second mirror.

LA1027-A   LA 1131-A   AL1225-A   sample   LB1761-A   BB1-E02P

customized input coupler
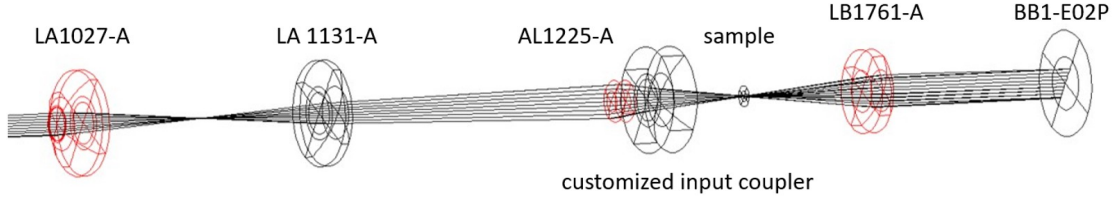
Figure 6.14 – Ray-tracing of the cavity performed in Winlens Basic. The optics LA1027-A, LA 1131-A, AL1225-A, LB1761-A, BB1-E02P are from Thorlabs, and the customized input coupler is with a planar surface and a concave surface of curvature radius 25 mm (UV Fused silica). Spherical optics and planar surfaces introduce aberration into the system and therefore reduce coupling efficiency.

To assess the mode-matching quality, we tried to align the pump laser and the cavity without placing the diamond plate inside, in which case the theoretical build-up factor is calculated to be ~19. Given the cavity length about 5 cm, we can calculate the resonance linewidth to be ~ 100 MHz, and spectrally aligning the pump laser (Verdi, 50 MHz linewidth according to specification) to the cavity resonance would require nm resolution positioning [8]. In our attempt to align the pump laser to the cavity, however, bright laser spot on the second mirror was easily observed, due to that spherical aberration was introduced to the system by the optics we employed (spherical lens, plano-concave input coupler), resulting in mode matching between the pump laser and high-order cavity modes. This phenomenon has been discussed in detail in Ref. [295], where mode-matching to high-order cavity modes caused severe resonance broadening. For the purpose of lasing, it is more important to know about the actual build-up factor, which, however, was not measured with this configuration as the second mirror we used is not back-side polished. To measure this quantity, the second mirror was replaced by a convex lens and a back-side polished plano mirror (~ 99.5% reflection for both wavelengths) [9]. The transmission from the output-coupler can then be monitored and compared to the pump intensity, and the best build-up we measured was around 10, as mode-matching optics are arranged to give best coupling only into the TEM_{00} mode (Fig. 6.14). To approach the theoretical prediction, a few options can be chosen for optimizing mode-matching: employing aspheric optics to reduce aberration, using deformable mirrors or spatial light modulators to pre-correct the wavefront of the pump laser, replacing plano-concave mirror with a special anaclastic design as demonstrated in Ref. [295], or simply use a pump laser with higher power.

If near-ideal mode matching can be achieved, as we have briefly mentioned above, the spectral

---

[8] Here we only consider mode matching between a pump laser with Gaussian profile and the TEM_{00} mode of the cavity with 25 mm radius curvature concave mirrors.

[9] The standard plano-concave mirror from Thorlabs which is highly reflective for our interested wavelength is not back-side polished, and limited by the budget a customized output-coupler was not ordered. This replacement does not affect the mode-waist calculation, as mathematically they are nearly equivalent expect for the scattering and additional spherical aberration at the convex lens surface, which are negligible to the system in the current case. FSR also changes with cavity length.

alignment between pump laser and cavity resonance would become critical for maximum delivery of the pump power, yet this is extremely challenging to realize via mechanical positioning as nm accuracy would be required. An alternative way to achieve this is by thermo-optic tuning, since diamond has low dn/dT coefficient about 1E-5, and a commercial Peltier module with tuning accuracy ∼ 0.05 K is sufficient to tune the cavity resonance with 50 MHz accuracy.

6.5.3 Integrated Nanobeam Cavities

The abovementioned substrate was cut and polished into smaller pieces and one of them was sent to Lončar group at Harvard University, for the fabrication of high-Q nanobeam cavities [10], with a design resonance at 737 nm. The fabricated cavities are shown in Fig. 6.15. When the pump laser is aligned with the cavity center, we could observe scattered light from the notches on the waveguide ends. The PL spectra were investigated at temperature from 4K to 80K, however we could not confirm any cavity resonance due to two reasons: (a) the inhomogeneous frequency splitting described in section 6.4.1 prevented us from assigning any additional peak to a cavity resonance, unless a resonance is observed far away from the four-line transitions, which we did not observe; (b) the setup we used is not confocal and the collected PL signal is from both the cavity and the substrate down to a certain depth, resulting in compromised SNR (signal-to-noise ratio) [11].

This nanobeam cavity is designed to have a ∼ $0.5(\lambda/n)^3$ mode volume [43] and ∼ 10,000 q-factor (corresponding to ∼ 20 cm^{-1} loss which is much higher than the gain coefficient of our sample at 300K). As we could not characterize the emission and absorption cross-sections at cryogenic temperature, we observe the temperature-dependent behaviors of SiV$^-$ absorption and emission reported in Ref. [297, 267], and assume a six(three)-fold increase in emission(absorption) at ZPL. With these assumptions, the estimated threshold power for lasing should be about ∼ 3 mW if 10-fold enhancement of absorption and emission due to Purcell effect is present ($\sigma_{em}^{4K} = 10 \times 6 \times \sigma_{em}^{300K}, \sigma_{abs}^{4K} = 10 \times 3 \times \sigma_{abs}^{300K}$), with the cavity geometry estimated to have a cross-section area 1.1E-9 cm^2, and cavity length 3E-4 cm. We note that in Ref. [296] a similar nanobeam cavity design with ∼ $1.8(\lambda/n)^3$ mode volume already gives a Purcell factor better than 26, and the absence of lasing transition in our sample up to 15 mW pump power is not identifiable without more sophisticated characterization apparatus. It is also possible that the cavity resonance is not on emitter transitions, and a confocal setup with the capability to tune the cavity resonance via, for example, gas condensation, would be helpful in determining the possible reasons concretely.

Overall, diamond laser with SiV centers is, if assumptions made above hold true, possible in theory, and both bulk cavity and integrated cavity are potential technological routes towards its realization. Further study in this direction would strongly benefit from more comprehen-

---

[10]Special acknowledgment to Cleaven Chia for taking care of the fabrication during the difficult times of COVID-19.

[11]In fact, as can be seen in Ref. [296], if the cavity resonance is not on the emitter transition frequency, even confocal setup does not give very high SNR.
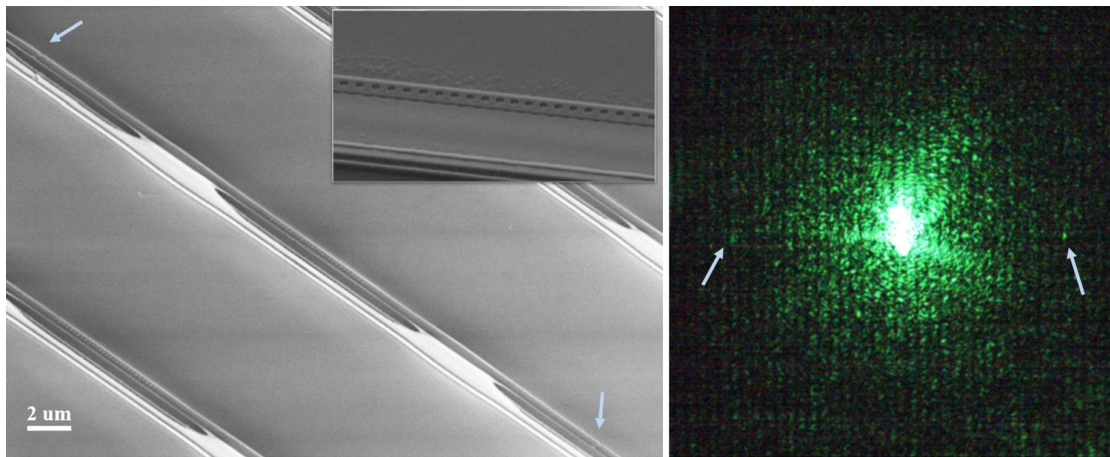
Figure 6.15 – Left: SEM observation of the fabricated nanobeam cavities, with two arrows pointing to small notches that scatter light. Right: optical image when 532 nm pump laser is focused onto the cavity center, with light scattered by notches visible as bright spots.

sive material characterizations at room and cryogenic temperatures, and from experimental techniques allowing near-ideal spatial and spectral alignment between pump laser and cavity resonance.

7 Conclusion and Outlook

In this thesis we first demonstrated using broad inert ion beam for smoothening single crystal diamond whose surface is damaged due to mechanical polishing, with resultant sub-nm roughness which is indispensable for large-scale integration of photonics devices such as waveguides and superconductive nanowire detectors. The process developed, unlike conventional polishing schemes, does not exert high mechanical pressure onto the surface and is therefore suitable for polishing large or thin substrates. Since the damage during this process only happens on the very surface of diamond and is easily removed by annealing or O_2 plasma treatment, it is expected to be widely applicable to quantum photonics device fabrication where mechanically induced sub-surface damage leads to adverse effects on color centers.

Following this, we explored the possibility to leverage ion-beam induced self-organization for the maskless nanostructuring of diamond surfaces. Aligned ripples with periodicity below 20 nm were observed on the ion beam treated surface and the amplitudes and the wavelengths are tunable depending on the incidence angle and acceleration energy of impinging ions. Templated dewetting of gold films with thickness below the ripple amplitude height was observed to lead to the formation of aligned nanoparticles, and further experiments in this direction have the potential to eventually enable a lithography-free approach for structuring diamond at the nanometer scale.

On device level, free-standing optical resonators were fabricated directly from a SCD bulk substrate, with the help of highly symmetric miniaturized Faraday cages. The design and fabrication method of such Faraday cages provide improved flexibility in angled-etch approach compared to early demonstrations, and allows this process technique to become repeatable. In addition, smoothing of inversely tapered side-walls was shown feasible with adequate processing conditions, which further improves device quality fabricated using this method.

Eventually, we characterized color centers incorporated in situ during CVD growth and fabricated by ion implantation and annealing. The collected data suggest that a SiV laser, in principle, should be possible, as long as a cavity with sufficient build-up can be realized or a strong optical pumping is available. In addition, at cryogenic temperature, we observed

anomalous photoluminescence from ensemble SiVs that was, to our knowledge, not reported in literature. This implies possibly unknown mechanism that may be explored for quantum applications involving color centers.

At the time this thesis being written, all components that are required for linear optics quantum information processing [80] and Boson sampling [298] (*i.e.* single photon source, waveguide, power splitter, modulator[1], and single photon detector), have been demonstrated as stand-alone working devices in diamond (c.f. section 2.2.2 for details). While this is promising already, it still requires considerable efforts in material engineering and device performance optimization before an all-integrated diamond quantum photonics circuit may come into reality. In addition, despite the delightful progresses that have been achieved employing angled-etch, it is, as shown in section 5.4, very challenging to realize efficient waveguide coupling based on this technique given the intrinsic geometrical restrictions. It should be noted, nevertheless, that all devices demonstrated with angled-etch can be readily fabricated on a DOI platform, if needed. We further note that this thesis is part of the project funded by SNSF Grant No. 183717 and 157566, which aims at establishing a scalable diamond photonics platform for optoelectronics device integration. Along with the theses of Dr. Teodoro Graziosi and of Dr. Marcell Kiss, we have explored the possibilities in DOI, angled-etch, and SCREAM processes, and the lessons we learned lead us to the conclusion, that a DOI platform, if it can be realized, would be the most promising candidate for the scalable integration of diamond photonic devices.

We expect a few key technologies to be developed before a fully functional quantum photonics circuit in diamond can be realized: a) scalable high-quality substrate growth with different crystal orientations, controlled doping and isotopic engineering; b) diamond-insulator bonding compatible for subsequent processing; c) color center incorporation with well-controlled position and orientation; d) on-demand generation of single photons with low noise and their synchronization; e) efficient phase and intensity modulation on-chip; f) integrated single photon detection with sufficiently high efficiency.

Bearing in mind that all above-mentioned technologies pose a great challenge to overcome, heterogeneous integration (*i.e.* to integrate diamond components into photonic circuits built on another material) can be a much easier technical route to explore: it is true that large-scale screening (quality-check) and pick-and-place of diamond micro-chiplets [299] into carrier circuits may not be efficient, but this way the stringent requirements on material engineering would be largely relieved, and interfacing efficiency as an additional bottleneck can be relatively easy to tackle with through design optimization [300, 301].

Taking one step back, lest we forget that diamond is not necessarily the best candidate for quantum photonics: recent discoveries on room-temperature single photon emitters in silicon [302, 303, 304] and AlN (aluminum nitride) [305, 306] platforms have declared their similar

---

[1]Modulator has only been demonstrated for polycrystalline diamond-on-insulator platform [81] but the processing technique can be adopted for single crystal DOI platform straightforwardly.

(or perhaps even greater) potentials to become a prevailing material platform for quantum photonics.

Similar to color centers in diamond, implantation and subsequent annealing make it possible to incorporate point defects into silicon and AlN wafers with positional control. In addition, the processing of both materials is way more industry-friendly [307, 308] than that of diamond, and high-quality silicon-on-insulator and AlN-on-sapphire wafers are readily available commercially. For AlN, its transparency and high third order nonlinear susceptibility (comparable to silicon nitride [309]) facilitate low-loss resonator [310] and frequency comb generation [311] over a large bandwidth. The piezoelectric property of AlN further provides the possibility to realize dynamic tuning of the cavity resonance [312, 313] and potentially acoustic control of quantum spins via strain field. For silicon photonics platforms, beside the demonstrated and matured manufacturability, functionality and scalability, the G-center has shown promising properties such as electroluminescence [314] and ODMR [315], which closely resemble what made diamond color centers exceptionally attractive. If further study may demonstrate favorable properties of point defects (*e.g.* optically or electrically initializable spin states, long coherence time of spin qubit, efficient light-spin interface) in these materials, it can be expected that the well-established foundry-PDK (process design kit) ecosystem will not take too long to bring fully functional quantum photonics circuits into real life.

A Integration of adKS Equation by Finite Difference

The adKS equation has been employed in many works in the context of ion beam induced self-organization. By adjusting the parameters it can be readily reduced to undamped anisotropic (by setting $\gamma = 0$) or isotropic (by setting $\alpha = 0, \beta = 0$) KS equation, in which cases all following content still apply. With $h \equiv h(\boldsymbol{r} \equiv x \cdot \hat{e}_x + y \cdot \hat{e}_y, t)$ representing the surface profile, the equation in its continuous form, after rescaling, reads

$$\partial_t h = -(\gamma + \partial_x^2 + \alpha \partial_y^2 + \Delta^2)h + (\partial_x h)^2 + \beta(\partial_y h)^2 + \eta \tag{A.1}$$

where $\eta \equiv \eta(t)$ is time-dependent Gaussian noise. Two real numbers α and β quantify the anisotropy for the linear and non-linear terms, respectively.

To integrate this PDE, we first discretize the 2d space into a grid of points spaced by dx. The derivatives can then be expressed in terms of matrix,

$$\partial_x^2 \sim \frac{16(U+L)-(U^2+L^2)-30I}{12(dx)^2}, \tag{A.2}$$

$$\partial_y^2 \sim (\partial_x^2)^\dagger, \tag{A.3}$$

where $U_{ij} = \delta_{i+1,j}$, $L_{ij} = \delta_{i,j+1}$ with δ being the Kronecker delta, and I is identity matrix. Similarly, the nonlinear terms can be expressed as

$$(\partial_x h)^2 \sim \frac{(Uh-h)^2+(Uh-h)(h-Lh)+(h-Lh)^2}{3(dx)^2}, \tag{A.4}$$

$$(\partial_y h)^2 \sim \frac{(hL-h)^2+(hL-h)(h-hU)+(h-hU)^2}{3(dx)^2}. \tag{A.5}$$

From this point the equation can be straightforwardly integrated in MATLAB with matrix multiplication.

We have mentioned in the main text that the parameter γ is set arbitrarily as it cannot be calculated from first-principle derivation. To see how the choice of γ influences the time evolution of adKS equation, we expand h in the frequency domain $h(\boldsymbol{r}, t) = \sum_i \tilde{h}_i(t)$ with $\tilde{h}_i \equiv A_i(t)cos(\boldsymbol{k_i r}) + B_i(t)sin(\boldsymbol{k_i r})$. Supposing $A_i(t)$ and $B_i(t)$ are first-order differentiable,
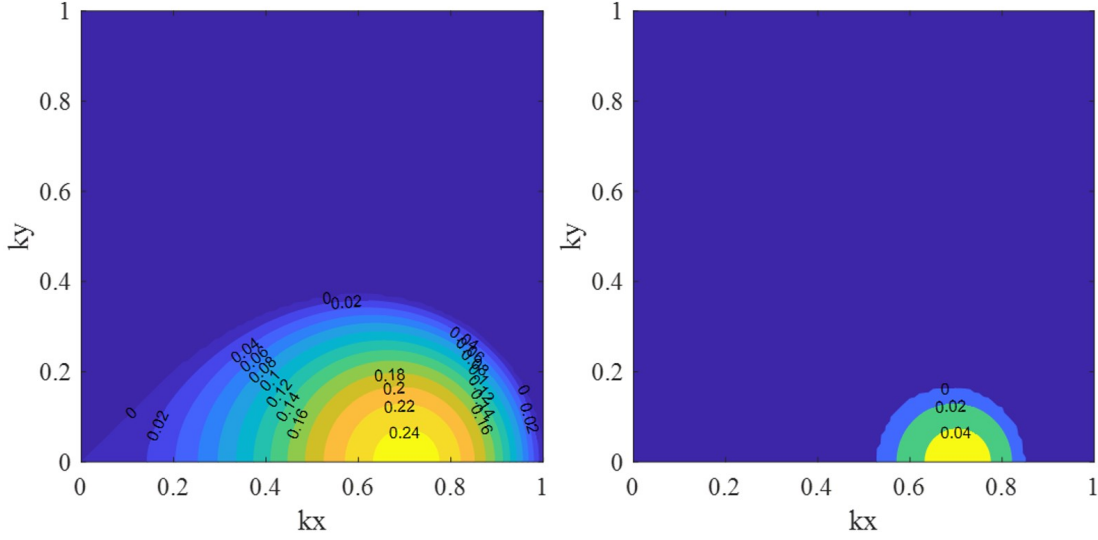
Figure A.1 – The growth rate in k-space with $\gamma = 0$ (left) and $\gamma = 2$ (right). In both cases we used $\alpha = 0.8$, which leads to the anisotropy of growth rate in k-space.

which is the case in continuous ion beam treatment neglecting noise, we have

$$
\begin{aligned}
\partial_t h &= \sum_i A'_i cos(\boldsymbol{k_i r}) + B'_i sin(\boldsymbol{k_i r}) \\
&= \sum_i (-\gamma + k_{ix}^2 + \alpha k_{iy}^2 - \boldsymbol{k_i}^4) \cdot \tilde{h}_i \\
&\quad + \left\{ \sum_i k_{ix} (A_i sin(\boldsymbol{k_i r}) - B_i cos(\boldsymbol{k_i r})) \right\}^2 \\
&\quad + \beta \left\{ \sum_i k_{iy} (A_i sin(\boldsymbol{k_i r}) - B_i cos(\boldsymbol{k_i r})) \right\}^2 + \eta.
\end{aligned}
\tag{A.6}
$$

As we integrate the equation from a flat-surface initial condition, before the amplitudes A_i, B_i reach certain level, only the linear term plays an important role. In this linear regime the amplitude grows exponentially as $e^{-\gamma + k_{ix}^2 + \alpha k_{iy}^2 - \boldsymbol{k_i}^4}$.

The expression $-\gamma + k_{ix}^2 + \alpha k_{iy}^2 - \boldsymbol{k_i}^4$ is often called growth rate in literature, and in the figure below we plot the growth rate in the frequency space, assuming $\alpha = 0.8$. When there is no damping, *i.e.* $\gamma = 0$, growth happens over a larger frequency space. In contrast, if we set $\gamma = 2$, only in a very small frequency range can the ripples grow. In a numerical simulation , if γ is set too high, the resulting image would have very well defined parallel ripples with a sinusoid height profile. For this reason we have set $\gamma = 1$ in the main text to reproduce a less regular surface feature.

B Faraday Cage from 2D to 3D

We have seen that a 2D pattern can be extruded into 3D in Chap. 5. Here we explain the design and the limitations on aspect ratio. As shown in the figure below, white spaces inside the layout are to be removed, leaving a metal (in our case, aluminum) foil on the rim and in the center, and metal wires between them.

After writing the pattern, the structured foil is clamped by the two round parts shown in the figure below, following which we use the cone-shaped part to extrude the foil into a volume. As pure-aluminum is soft, the wires colored black will be straightened, while the wires colored red only levels up vertically. Consequently, the angle of the sidewall is defined by the length of the black wires and the spacing between red wires. If we denote the spacing by s and the length of black wire by b, the maximum achievable angle of the sidewall (relative to plane of the rim/top) is then $\theta = arccos(s/b)$. As the length of black wires is fundamentally limited by its finite thickness and the finite spacing, the cage cannot be arbitrarily vertical, and given fixed wire thickness, the less the spacing is, the lower the limit is on the aspect ratio.
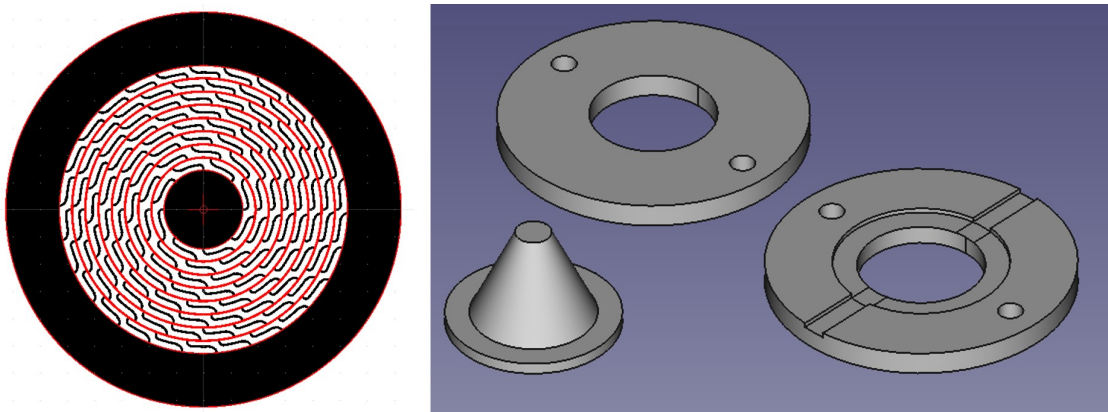
Figure B.1 – 2D layout of a Faraday cage (left) and auxiliary tools for extruding it into 3D (right).

C Fabrication of Dimpled Fiber Tapers

Dimpled tapered fibers are convenient for probing photonic cavities integrated on-chip. To fabricate them reproducibly with well-defined curvature, the setup can grow in complexity as demonstrated in [316]. Here we provide a method for fabricating dimpled fiber with a standard heating-and-pulling setup, as explained in Fig. C.2. This method does not guarantee yield but can be readily implemented with existing tools. The procedure is:

(a) Pulling the fiber while heating, a tapered region results;
(b) Squeezing the tapered region with the heat turned off;
(c) A curl is formed from step b and heating makes it a dimple;
(d) Pulling the fiber again, this time with the heat off, to tension the dimpled taper.

To achieve a very thin taper ($< 1~\mu$m) the fiber may easily break during fabrication. In this
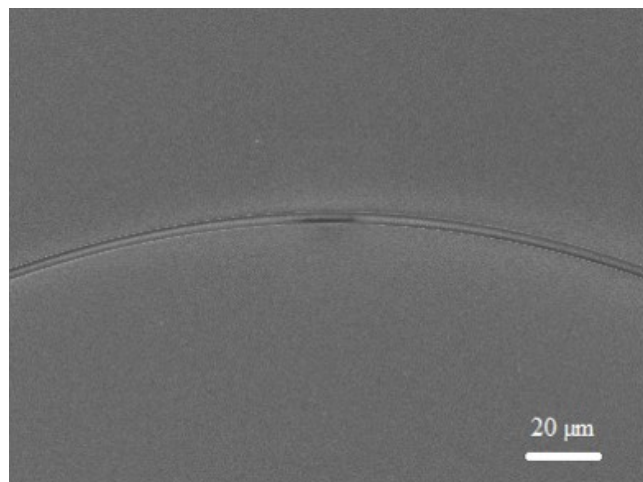
Figure C.1 – SEM picture of dimpled tapered-fiber.
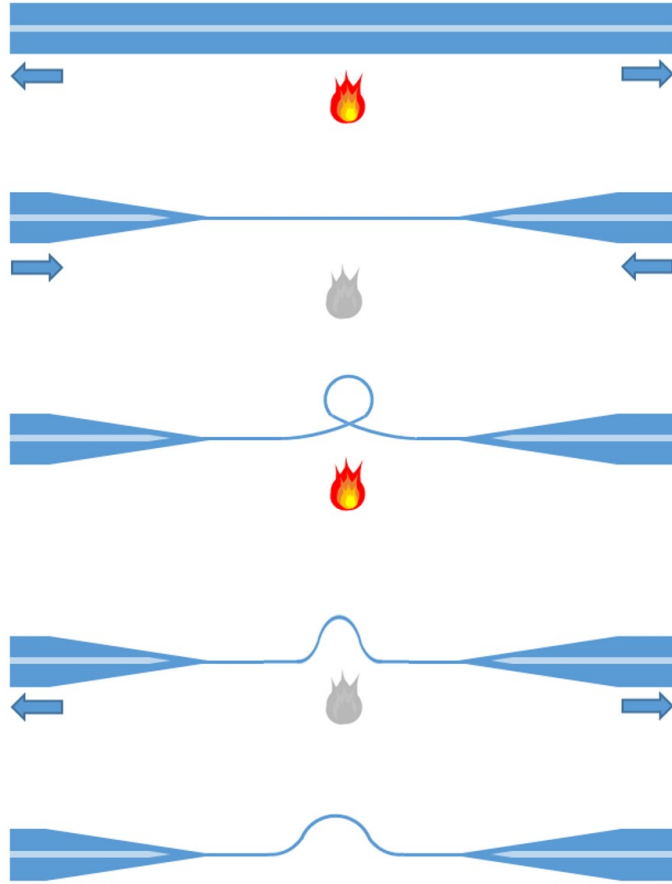
Figure C.2 – The protocol for dimpled tapered-fiber fabrication. Arrows indicate the movement direction of clamps. Grey-scale colored fire corresponds to off-state.

case BHF can be used to further thin the dimpled fiber. The etch-rate of this process is about 70 nm/min for a standard single-mode telecom fiber, and we have successfully fabricated dimpled fibers with diameter < 700 nm.

Bibliography

[1] Yana Fedortchouk. A new approach to understanding diamond surface features based on a review of experimental and natural diamond studies. *Earth-science reviews*, 193:45–65, 2019.

[2] Jagdish Narayan, Siddharth Gupta, Anagh Bhaumik, Ritesh Sachan, Filippo Cellini, and Elisa Riedo. Q-carbon harder than diamond. *Mrs Communications*, 8(2):428–436, 2018.

[3] Quan Huang, Dongli Yu, Bo Xu, Wentao Hu, Yanming Ma, Yanbin Wang, Zhisheng Zhao, Bin Wen, Julong He, Zhongyuan Liu, et al. Nanotwinned diamond with unprecedented hardness and stability. *Nature*, 510(7504):250–253, 2014.

[4] Yongjun Tian, Bo Xu, Dongli Yu, Yanming Ma, Yanbin Wang, Yingbing Jiang, Wentao Hu, Chengchun Tang, Yufei Gao, Kun Luo, et al. Ultrahard nanotwinned cubic boron nitride. *Nature*, 493(7432):385–388, 2013.

[5] PJ Lu, N Yao, JF So, GE Harlow, JF Lu, GF Wang, and PM Chaikin. The earliest use of corundum and diamond, in prehistoric china. *Archaeometry*, 47(1):1–12, 2005.

[6] J. Healey and P. Elder. *Natural History*. Penguin classics. Penguin Books Limited, 2004.

[7] RS Sussmann, CSJ Pickles, JR Brandon, CJH Wort, SE Coe, A Wasenczuk, CN Dodge, AC Beale, AJ Krehan, P Dore, et al. Cvd diamond windows for infrared synchrotron applications. *Il Nuovo Cimento D*, 20(4):503–525, 1998.

[8] Elliot Snider, Nathan Dasenbrock-Gammon, Raymond McBride, Mathew Debessai, Hiranya Vindana, Kevin Vencatasamy, Keith V Lawler, Ashkan Salamat, and Ranga P Dias. Room-temperature superconductivity in a carbonaceous sulfur hydride. *Nature*, 586(7829):373–377, 2020.

[9] Christian Kurtsiefer, Sonja Mayer, Patrick Zarda, and Harald Weinfurter. Stable solid-state source of single photons. *Physical review letters*, 85(2):290, 2000.

[10] Alexios Beveratos, Rosa Brouri, Thierry Gacoin, André Villing, Jean-Philippe Poizat, and Philippe Grangier. Single photon quantum cryptography. *Physical review letters*, 89(18):187901, 2002.

[11] Markus M Hoffmann, R Shane Addleman, and John L Fulton. Short-pathlength, high-pressure flow cell for static and time-resolved infrared spectroscopy suitable for super-critical fluid solutions including hydrothermal systems. *Review of Scientific instruments*, 71(3):1552–1556, 2000.

[12] Stephan Handschuh-Wang, Tao Wang, Lifei Zhu, Yang Xu, Lei Huang, Tiansheng Gan, Yongbing Tang, and Xuechang Zhou. Corrosion-resistant functional diamond coatings for reliable interfacing of liquid metals with solid metals. *ACS Applied Materials & Interfaces*, 12(36):40891–40900, 2020.

[13] Chaker Fares, Fan Ren, Marko J Tadjer, Jeffrey Woodward, Michael A Mastro, Boris N Feigelson, Charles R Eddy Jr, and SJ Pearton. Band offset determination for amorphous al2o3 deposited on bulk aln and atomic-layer epitaxial aln on sapphire. *Applied Physics Letters*, 117(18):182103, 2020.

[14] Carsten Schinke, P Christian Peest, Jan Schmidt, Rolf Brendel, Karsten Bothe, Malte R Vogt, Ingo Kröger, Stefan Winter, Alfred Schirmacher, Siew Lim, et al. Uncertainty analysis for the coefficient of band-to-band absorption of crystalline silicon. *AIP Advances*, 5(6):067168, 2015.

[15] Alexander M Zaitsev. *Optical properties of diamond: a data handbook.* Springer Science & Business Media, 2013.

[16] Shova Subedi, Vladimir Fedorov, Sergey Mirov, and Matthew Markham. Laser spectroscopic and saturation properties of gr1 centers in synthetic diamond. In *Solid State Lasers XXIX: Technology and Devices*, volume 11259, page 1125928. International Society for Optics and Photonics, 2020.

[17] Shreya Nad, Amanda Charris, and Jes Asmussen. MPACVD growth of single crystalline diamond substrates with pcd rimless and expanding surfaces. *Applied Physics Letters*, 109(16):162103, 2016.

[18] Satoshi Koizumi, Hitoshi Umezawa, Julien Pernot, and Mariko Suzuki. Diamond wafer technologies for semiconductor device applications. In *Power Electronics Device Applications of Diamond Semiconductors*, pages 1–97. Elsevier, 2018.

[19] Sichen Mi, Marcell Kiss, Teodoro Graziosi, and Niels Quack. Integrated photonic devices in single crystal diamond. *Journal of Physics: Photonics*, 2(4):042001, 2020.

[20] Igor Aharonovich, Andrew D Greentree, and Steven Prawer. Diamond photonics. *Nature Photonics*, 5(7):397–405, 2011.

[21] Carlo Bradac, Weibo Gao, Jacopo Forneris, Matthew E Trusheim, and Igor Aharonovich. Quantum nanophotonics with group iv defects in diamond. *Nature Communications*, 10(1):1–13, 2019.

[22] Francesco Lenzini, Nico Gruhler, Nicolai Walter, and Wolfram HP Pernice. Diamond as a platform for integrated quantum photonics. *Advanced Quantum Technologies*, 1(3):1800061, 2018.

[23] Steven Prawer and Igor Aharonovich. *Quantum information processing with diamond: Principles and applications*. Elsevier, 2014.

[24] Yuzhou Wu, Fedor Jelezko, Martin B Plenio, and Tanja Weil. Diamond quantum devices in biology. *Angewandte Chemie International Edition*, 55(23):6586–6598, 2016.

[25] Tim Schröder, Sara L Mouradian, Jiabao Zheng, Matthew E Trusheim, Michael Walsh, Edward H Chen, Luozhou Li, Igal Bayn, and Dirk Englund. Quantum nanophotonics in diamond. *JOSA B*, 33(4):B65–B83, 2016.

[26] Edlyn V Levine, Matthew J Turner, Pauli Kehayias, Connor A Hart, Nicholas Langellier, Raisa Trubko, David R Glenn, Roger R Fu, and Ronald L Walsworth. Principles and techniques of the quantum diamond microscope. *Nanophotonics*, 8(11):1945–1973, 2019.

[27] Anna Maria Ferrari, Simone Salustro, Francesco Silvio Gentile, William C Mackrodt, and Roberto Dovesi. Substitutional nitrogen in diamond: A quantum mechanical investigation of the electronic and spectroscopic properties. *Carbon*, 134:354–365, 2018.

[28] Stefania Castelletto, Andrew Edmonds, Torsten Gaebel, and James Rabeau. Production of multiple diamond-based single-photon sources. *Ieee Journal of Selected Topics in Quantum Electronics*, 18(6):1792–1798, 2012.

[29] Shova D Subedi, Vladimir V Fedorov, Jeremy Peppers, Dmitry V Martyshkin, Sergey B Mirov, Linbo Shao, and Marko Loncar. Laser spectroscopic characterization of negatively charged nitrogen-vacancy (nv-) centers in diamond. *Optical Materials Express*, 9(5):2076–2087, 2019.

[30] Peng Ji, R Balili, Jonathan Beaumariage, Shouvik Mukherjee, D Snoke, and MV Gurudev Dutt. Multiple-photon excitation of nitrogen vacancy centers in diamond. *Physical Review B*, 97(13):134112, 2018.

[31] Bartholomeus Machielse, Stefan Bogdanovic, Srujan Meesala, Scarlett Gauthier, Michael J Burek, Graham Joe, Michelle Chalupnik, Young-Ik Sohn, Jeffrey Holzgrafe, Ruffin E Evans, et al. Quantum interference of electromechanically stabilized emitters in nanophotonic devices. *Physical Review X*, 9(3):031022, 2019.

[32] Smarak Maity, Linbo Shao, Young-Ik Sohn, Srujan Meesala, Bartholomeus Machielse, Edward Bielejec, Matthew Markham, and Marko Lončar. Spectral alignment of single-photon emitters in diamond using strain gradient. *Physical Review Applied*, 10(2):024050, 2018.

[33] Alp Sipahigil, Michael Lurie Goldman, Emre Togan, Yiwen Chu, Matthew Markham, Daniel J Twitchen, Alexander S Zibrov, Alexander Kubanek, and Mikhail D Lukin. Quantum interference of single photons from remote nitrogen-vacancy centers in diamond. *Physical review letters*, 108(14):143601, 2012.

[34] Young-Ik Sohn, Srujan Meesala, Benjamin Pingault, Haig A Atikian, Jeffrey Holzgrafe, Mustafa Gündoğan, Camille Stavrakas, Megan J Stanley, Alp Sipahigil, Joonhee Choi, et al. Controlling the coherence of a diamond spin qubit through its strain environment. *Nature communications*, 9(1):1–6, 2018.

[35] Srujan Meesala, Young-Ik Sohn, Benjamin Pingault, Linbo Shao, Haig A Atikian, Jeffrey Holzgrafe, Mustafa Gündoğan, Camille Stavrakas, Alp Sipahigil, Cleaven Chia, et al. Strain engineering of the silicon-vacancy center in diamond. *Physical Review B*, 97(20):205444, 2018.

[36] Stefan Hepp, Michael Jetter, Simone Luca Portalupi, and Peter Michler. Semiconductor quantum dots for integrated quantum photonics. *Advanced Quantum Technologies*, 2(9):1900020, 2019.

[37] DA Gangloff, Gabriel Ethier-Majcher, Constantin Lang, EV Denning, JH Bodey, DM Jackson, Edmund Clarke, Maxime Hugues, Claire Le Gall, and Mete Atatüre. Quantum interface of an electron and a nuclear ensemble. *Science*, 364(6435):62–66, 2019.

[38] CE Bradley, J Randall, MH Abobeih, RC Berrevoets, MJ Degen, MA Bakker, M Markham, DJ Twitchen, and TH Taminiau. A ten-qubit solid-state spin register with quantum memory up to one minute. *Physical Review X*, 9(3):031045, 2019.

[39] Simeon Bogdanov, MY Shalaginov, Alexandra Boltasseva, and Vladimir M Shalaev. Material platforms for integrated quantum photonics. *Optical Materials Express*, 7(1):111–132, 2017.

[40] Takayuki Iwasaki, Yoshiyuki Miyamoto, Takashi Taniguchi, Petr Siyushev, Mathias H Metsch, Fedor Jelezko, and Mutsuko Hatano. Tin-vacancy quantum emitters in diamond. *Physical review letters*, 119(25):253601, 2017.

[41] Alison E Rugar, Constantin Dory, Shuo Sun, and Jelena Vučković. Characterization of optical and spin properties of single tin-vacancy centers in diamond nanopillars. *Physical Review B*, 99(20):205417, 2019.

[42] Mika Tham Westerhausen, Aleksandra Trycz, Connor Stewart, Milad Nonahal, Blake Regan, Mehran Kianinia, and Igor Aharonovich. Controlled doping of gev and snv color centers in diamond using chemical vapor deposition. *ACS Applied Materials & Interfaces*, 2020.

[43] Mihir K Bhaskar, Ralf Riedinger, Bartholomeus Machielse, David S Levonian, Christian T Nguyen, Erik N Knall, Hongkun Park, Dirk Englund, Marko Lončar, Denis D Sukachev,

et al. Experimental demonstration of memory-enhanced quantum communication. *Nature*, 580(7801):60–64, 2020.

[44] MV Gurudev Dutt, L Childress, L Jiang, E Togan, J Maze, F Jelezko, AS Zibrov, PR Hemmer, and MD Lukin. Quantum register based on individual electronic and nuclear spin qubits in diamond. *Science*, 316(5829):1312–1316, 2007.

[45] Peter Christian Maurer, Georg Kucsko, Christian Latta, Liang Jiang, Norman Ying Yao, Steven D Bennett, Fernando Pastawski, David Hunger, Nicholas Chisholm, Matthew Markham, et al. Room-temperature quantum bit memory exceeding one second. *Science*, 336(6086):1283–1286, 2012.

[46] CT Nguyen, DD Sukachev, MK Bhaskar, B Machielse, DS Levonian, EN Knall, P Stroganov, C Chia, MJ Burek, R Riedinger, et al. An integrated nanophotonic quantum register based on silicon-vacancy spins in diamond. *Physical Review B*, 100(16):165428, 2019.

[47] Bing Chen, Shuo Li, Xianfei Hou, Feifei Zhou, Peng Qian, Feng Mei, Suotang Jia, Nanyang Xu, and Heng Shen. Digital quantum simulation of floquet topological phases with a solid-state quantum simulator. *arXiv preprint arXiv:2012.05495*, 2020.

[48] Kebiao Xu, Tianyu Xie, Zhaokai Li, Xiangkun Xu, Mengqi Wang, Xiangyu Ye, Fei Kong, Jianpei Geng, Changkui Duan, Fazhan Shi, et al. Experimental adiabatic quantum factorization under ambient conditions based on a solid-state single spin system. *Physical review letters*, 118(13):130504, 2017.

[49] Felix M Stürner, Andreas Brenneis, Thomas Buck, Julian Kassel, Robert Rölver, Tino Fuchs, Anton Savitsky, Dieter Suter, Jens Grimmel, Stefan Hengesbach, et al. Integrated and portable magnetometer based on nitrogen-vacancy ensembles in diamond. *arXiv preprint arXiv:2012.01053*, 2020.

[50] Brian B Zhou, Paul C Jerger, Kan-Heng Lee, Masaya Fukami, Fauzia Mujid, Jiwoong Park, and David D Awschalom. Spatiotemporal mapping of a photocurrent vortex in monolayer mos 2 using diamond quantum sensors. *Physical Review X*, 10(1):011003, 2020.

[51] John F Barry, Matthew J Turner, Jennifer M Schloss, David R Glenn, Yuyu Song, Mikhail D Lukin, Hongkun Park, and Ronald L Walsworth. Optical magnetic detection of single-neuron action potentials using quantum defects in diamond. *Proceedings of the National Academy of Sciences*, 113(49):14133–14138, 2016.

[52] Jeronimo R Maze, Paul L Stanwix, James S Hodges, Seungpyo Hong, Jacob M Taylor, Paola Cappellaro, Liang Jiang, MV Gurudev Dutt, Emre Togan, AS Zibrov, et al. Nanoscale magnetic sensing with an individual electronic spin in diamond. *Nature*, 455(7213):644–647, 2008.

[53] Julia Michl, Jakob Steiner, Andrej Denisenko, Bülau André, André Zimmermann, Kazuo Nakamura, Hitoshi Sumiya, Shinobu Onoda, Philipp Neumann, Junichi Isoya, et al.

Robust and accurate electric field sensing with solid state spin ensembles. *Nano letters*, 19(8):4904–4910, 2019.

[54] Bang Yang, Takuya Murooka, Kosuke Mizuno, Kwangsoo Kim, Hiromitsu Kato, Toshiharu Makino, Masahiko Ogura, Satoshi Yamasaki, Marek E Schmidt, Hiroshi Mizuta, et al. Vector electrometry in a wide-gap-semiconductor device using a spin-ensemble quantum sensor. *Physical Review Applied*, 14(4):044049, 2020.

[55] Kin On Ho, Man Yin Leung, Yiu Yung Pang, King Cho Wong, Ping Him Ng, and Sen Yang. In situ studies of stress environment in amorphous solids using negatively charged nitrogen vacancy (nv–) centers in nanodiamond. *ACS Applied Polymer Materials*, 2020.

[56] Kin On Ho, Man Yin Leung, Yaxin Jiang, Kin Pong Ao, Wei Zhang, King Yau Yip, Yiu Yung Pang, King Cho Wong, Swee K Goh, and Sen Yang. Probing local pressure environment in anvil cells with nitrogen-vacancy (n-v-) centers in diamond. *Physical Review Applied*, 13(2):024041, 2020.

[57] Georg Kucsko, Peter C Maurer, Norman Ying Yao, MICHAEL Kubo, Hyun Jong Noh, Po Kam Lo, Hongkun Park, and Mikhail D Lukin. Nanometre-scale thermometry in a living cell. *Nature*, 500(7460):54–58, 2013.

[58] Christian T Nguyen, Ruffin E Evans, Alp Sipahigil, Mihir K Bhaskar, Denis D Sukachev, Viatcheslav N Agafonov, Valery A Davydov, Liudmila F Kulikova, Fedor Jelezko, and Mikhail D Lukin. All-optical nanoscale thermometry with silicon-vacancy centers in diamond. *Applied Physics Letters*, 112(20):203102, 2018.

[59] Philipp Neumann, Ingmar Jakobi, Florian Dolde, Christian Burk, Rolf Reuter, Gerald Waldherr, Jan Honert, Thomas Wolf, Andreas Brunner, Jeong Hyun Shim, et al. High-precision nanoscale temperature sensing using single defects in diamond. *Nano letters*, 13(6):2738–2742, 2013.

[60] Sean Blakley, Xiaohan Liu, Ilya Fedotov, Ivan Cojocaru, Christapher Vincent, Masfer Alkahtani, Joe Becker, Michael Kieschnick, Tobias Lühman, Jan Meijer, et al. Fiber-optic quantum thermometry with germanium-vacancy centers in diamond. *ACS Photonics*, 6(7):1690–1693, 2019.

[61] Jing-Wei Fan, Ivan Cojocaru, Joe Becker, Ilya V Fedotov, Masfer Hassan A Alkahtani, Abdulrahman Alajlan, Sean Blakley, Mohammadreza Rezaee, Anna Lyamkina, Yuri N Palyanov, et al. Germanium-vacancy color center in diamond as a temperature sensor. *ACS Photonics*, 5(3):765–770, 2018.

[62] Vladimir V Soshenko, Stepan V Bolshedvorskii, Olga Rubinas, Vadim N Sorokin, Andrey N Smolyaninov, Vadim V Vorobyov, and Alexey V Akimov. Nuclear spin gyroscope based on the nv center in diamond. *arXiv preprint arXiv:2009.00916*, 2020.

[63] Yu-Lei Chen, Jun Tang, Hao Guo, Yan-Jie Gao, Yu-Song Liu, Zhen-Rong Shi, and Jun Liu. Wide-field planar magnetic imaging using spins in diamond. *IEEE Transactions on Nanotechnology*, 18:1156–1159, 2019.

[64] Gopalakrishnan Balasubramanian, IY Chan, Roman Kolesov, Mohannad Al-Hmoud, Julia Tisler, Chang Shin, Changdong Kim, Aleksander Wojcik, Philip R Hemmer, Anke Krueger, et al. Nanoscale imaging magnetometry with diamond spins under ambient conditions. *Nature*, 455(7213):648–651, 2008.

[65] David Le Sage, Koji Arai, David R Glenn, Stephen J DeVience, Linh M Pham, Lilah Rahn-Lee, Mikhail D Lukin, Amir Yacoby, Arash Komeili, and Ronald L Walsworth. Optical magnetic imaging of living cells. *Nature*, 496(7446):486–489, 2013.

[66] Margarita Lesik, Thomas Plisson, Loïc Toraille, Justine Renaud, Florent Occelli, Martin Schmidt, Olivier Salord, Anne Delobbe, Thierry Debuisschert, Loïc Rondin, et al. Magnetic measurements on micrometer-sized samples under high pressure using designed nv centers. *Science*, 366(6471):1359–1362, 2019.

[67] David R Glenn, Roger R Fu, Pauli Kehayias, David Le Sage, Eduardo A Lima, Benjamin P Weiss, and Ronald L Walsworth. Micrometer-scale magnetic imaging of geological samples using a quantum diamond microscope. *Geochemistry, Geophysics, Geosystems*, 18(8):3254–3267, 2017.

[68] P Kehayias, MJ Turner, R Trubko, JM Schloss, CA Hart, M Wesson, DR Glenn, and RL Walsworth. Imaging crystal stress in diamond using ensembles of nitrogen-vacancy centers. *Physical Review B*, 100(17):174103, 2019.

[69] S Hsieh, P Bhattacharyya, C Zu, T Mittiga, TJ Smart, F Machado, B Kobrin, TO Höhn, NZ Rui, Mehdi Kamrani, et al. Imaging stress and magnetism at high pressures using a nanoscale quantum sensor. *Science*, 366(6471):1349–1354, 2019.

[70] Christopher Foy, Lenan Zhang, Matthew E Trusheim, Kevin R Bagnall, Michael Walsh, Evelyn N Wang, and Dirk R Englund. Wide-field magnetic field and temperature imaging using nanoscale quantum sensors. *ACS applied materials & interfaces*, 12(23):26525–26533, 2020.

[71] Edward H Chen, Ophir Gaathon, Matthew E Trusheim, and Dirk Englund. Wide-field multispectral super-resolution imaging using spin-dependent fluorescence in nanodiamonds. *Nano letters*, 13(5):2073–2077, 2013.

[72] Kerem Bray, Leonard Cheung, Khondker Rufaka Hossain, Igor Aharonovich, Stella M Valenzuela, and Olga Shimoni. Versatile multicolor nanodiamond probes for intracellular imaging and targeted labeling. *Journal of Materials Chemistry B*, 6(19):3078–3084, 2018.

[73] Andrew M Edmonds, Connor A Hart, Matthew J Turner, Pierre-Olivier Colard, Jennifer M Schloss, Kevin Olsson, Raisa Trubko, Matthew L Markham, Adam Rathmill, Ben Horne-Smith, et al. Generation of nitrogen-vacancy ensembles in diamond for quantum sensors: Optimization and scalability of cvd processes. *arXiv preprint arXiv:2004.01746*, 2020.

[74] Linbo Shao, Mian Zhang, Matthew Markham, Andrew M Edmonds, and Marko Lončar. Diamond radio receiver: nitrogen-vacancy centers as fluorescent transducers of microwave signals. *Physical Review Applied*, 6(6):064008, 2016.

[75] M Chipaux, L Toraille, Ch Larat, L Morvan, S Pezzagna, J Meijer, and Th Debuisschert. Wide bandwidth instantaneous radio frequency spectrum analyzer based on nitrogen vacancy centers in diamond. *Applied Physics Letters*, 107(23):233502, 2015.

[76] Mayer Ludovic and Debuisschert Thierry. Nitrogen-vacancy centers in diamond for instantaneous spectral analysis in the radiofrequency domain up to 18 ghz. In *2018 International Topical Meeting on Microwave Photonics (MWP)*, pages 1–4. IEEE, 2018.

[77] Tom Delord, P Huillery, L Nicolas, and G Hétet. Spin-cooling of the motion of a trapped diamond. *Nature*, 580(7801):56–59, 2020.

[78] Igor Aharonovich, Dirk Englund, and Milos Toth. Solid-state single-photon emitters. *Nature Photonics*, 10(10):631–641, 2016.

[79] Gang Zhang, Yuan Cheng, Jyh-Pin Chou, and Adam Gali. Material platforms for defect qubits and single-photon emitters. *Applied Physics Reviews*, 7(3):031308, 2020.

[80] Emanuel Knill, Raymond Laflamme, and Gerald J Milburn. A scheme for efficient quantum computation with linear optics. *nature*, 409(6816):46–52, 2001.

[81] P Rath, S Ummethala, S Diewald, G Lewes-Malandrakis, D Brink, N Heidrich, C Nebel, and WHP Pernice. Diamond electro-optomechanical resonators integrated in nanophotonic circuits. *Applied Physics Letters*, 105(25):251102, 2014.

[82] Ph Tamarat, T Gaebel, JR Rabeau, M Khan, AD Greentree, H Wilson, LCL Hollenberg, S Prawer, P Hemmer, F Jelezko, et al. Stark shift control of single optical centers in diamond. *Physical review letters*, 97(8):083002, 2006.

[83] Hannes Bernien, Lilian Childress, Lucio Robledo, Matthew Markham, Daniel Twitchen, and Ronald Hanson. Two-photon quantum interference from separate nitrogen vacancy centers in diamond. *Physical Review Letters*, 108(4):043604, 2012.

[84] Hannes Bernien, Bas Hensen, Wolfgang Pfaff, Gerwin Koolstra, Machiel S Blok, Lucio Robledo, TH Taminiau, Matthew Markham, Daniel J Twitchen, Lilian Childress, et al. Heralded entanglement between solid-state qubits separated by three metres. *Nature*, 497(7447):86–90, 2013.

[85] Patrik Rath, Oliver Kahl, Simone Ferrari, Fabian Sproll, Georgia Lewes-Malandrakis, Dietmar Brink, Konstantin Ilin, Michael Siegel, Christoph Nebel, and Wolfram Pernice. Superconducting single-photon detectors integrated with diamond nanophotonic circuits. *Light: Science & Applications*, 4(10):e338–e338, 2015.

[86] Michael J Burek, Nathalie P De Leon, Brendan J Shields, Birgit JM Hausmann, Yiwen Chu, Qimin Quan, Alexander S Zibrov, Hongkun Park, Mikhail D Lukin, and Marko Loncar. Free-standing mechanical and photonic nanostructures in single-crystal diamond. *Nano letters*, 12(12):6084–6089, 2012.

[87] Behzad Khanaliloo, Matthew Mitchell, Aaron C Hryciw, and Paul E Barclay. High-q/v monolithic diamond microdisks fabricated with quasi-isotropic etching. *Nano letters*, 15(8):5131–5136, 2015.

[88] Constantin Dory, Dries Vercruysse, Ki Youl Yang, Neil V Sapra, Alison E Rugar, Shuo Sun, Daniil M Lukin, Alexander Y Piggott, Jingyuan L Zhang, Marina Radulaski, et al. Inverse-designed diamond photonics. *Nature communications*, 10(1):1–7, 2019.

[89] Simone Ferrari, Carsten Schuck, and Wolfram Pernice. Waveguide-integrated superconducting nanowire single-photon detectors. *Nanophotonics*, 7(11):1725–1758, 2018.

[90] Haig Avedis Atikian, Srujan Meesala, Michael John Burek, Young-Ik Sohn, Johan Israelian, Adarsh S Patri, Nigel Clarke, Alp Sipahigil, Ruffin Eley Evans, Denis Sukachev, et al. Novel fabrication of diamond nanophotonics coupled to single-photon detectors. *SPIE Newsroom*, 2017.

[91] Oliver Kahl, Simone Ferrari, Patrik Rath, Andreas Vetter, Christoph Nebel, and Wolfram HP Pernice. High efficiency on-chip single-photon detection for diamond nanophotonic circuits. *Journal of Lightwave Technology*, 34(2):249–255, 2016.

[92] Dibyendu Roy, Christopher M Wilson, and Ofer Firstenberg. Colloquium: Strongly interacting photons in one-dimensional continuum. *Reviews of Modern Physics*, 89(2):021001, 2017.

[93] Jeffrey Douglas Thompson, TG Tiecke, Nathalie Pulmones de Leon, J Feist, AV Akimov, M Gullans, Alexander S Zibrov, V Vuletić, and Mikhail D Lukin. Coupling a single trapped atom to a nanoscale optical cavity. *Science*, 340(6137):1202–1205, 2013.

[94] John F Barry, Jennifer M Schloss, Erik Bauch, Matthew J Turner, Connor A Hart, Linh M Pham, and Ronald L Walsworth. Sensitivity optimization for nv-diamond magnetometry. *Reviews of Modern Physics*, 92(1):015004, 2020.

[95] Francesco Casola, Toeno van der Sar, and Amir Yacoby. Probing condensed matter physics with magnetometry based on nitrogen-vacancy centres in diamond. *Nature Reviews Materials*, 3(1):1–13, 2018.

[96] Myeongwon Lee, Seong Jang, Woochan Jung, Yuhan Lee, Takashi Taniguchi, Kenji Watanabe, Ha-Reem Kim, Hong-Gyu Park, Gil-Ho Lee, and Donghun Lee. Mapping current profiles of point-contacted graphene devices using single-spin scanning magnetometer. *Applied Physics Letters*, 118(3):033101, 2021.

[97] Andrew Mark Edmonds, Connor A Hart, Matthew J Turner, Pierre-Olivier Colard, Jennifer M Schloss, Kevin Olsson, Raisa Trubko, Matthew L Markham, Adam Rathmill, Ben Horne-Smith, et al. Characterisation of cvd diamond with high concentrations of nitrogen for magnetic-field sensing applications. *Materials for Quantum Technology*, 2021.

[98] Sébastien Pezzagna and Jan Meijer. Quantum computer based on color centers in diamond. *Applied Physics Reviews*, 8(1):011308, 2021.

[99] Bing Chen, Shuo Li, Xianfei Hou, Feifei Ge, Feifei Zhou, Peng Qian, Feng Mei, Suotang Jia, Nanyang Xu, and Heng Shen. Digital quantum simulation of floquet topological phases with a solid-state quantum simulator. *Photonics Research*, 9(1):81–87, 2021.

[100] Ya Wang, Florian Dolde, Jacob Biamonte, Ryan Babbush, Ville Bergholm, Sen Yang, Ingmar Jakobi, Philipp Neumann, Alán Aspuru-Guzik, James D Whitfield, et al. Quantum simulation of helium hydride cation in a solid-state spin register. *ACS nano*, 9(8):7769–7774, 2015.

[101] Jonathan S Hodges, Norman Ying Yao, Dougal Maclaurin, C Rastogi, Mikhail D Lukin, and D Englund. Timekeeping with electron spin states in diamond. *Physical Review A*, 87(3):032118, 2013.

[102] M Kern, Jan Jeske, DWM Lau, AD Greentree, Fedor Jelezko, and J Twamley. Optical cryocooling of diamond. *Physical Review B*, 95(23):235306, 2017.

[103] Sichen Mi, Adrien Toros, Teodoro Graziosi, and Niels Quack. Non-contact polishing of single crystal diamond by ion beam etching. *Diamond and Related Materials*, 92:248–252, 2019.

[104] PK v Tien. Light waves in thin films and integrated optics. *Applied optics*, 10(11):2395–2413, 1971.

[105] AB Muchnikov, AL Vikharev, JE Butler, VV Chernov, VA Isaev, SA Bogdanov, AI Okhapkin, PA Yunin, and YN Drozdov. Homoepitaxial growth of cvd diamond after icp pretreatment. *physica status solidi (a)*, 212(11):2572–2577, 2015.

[106] Pierre-Nicolas Volpe, Pierre Muret, Franck Omnes, Jocelyn Achard, François Silva, Ovidiu Brinza, and Alix Gicquel. Defect analysis and excitons diffusion in undoped homoepitaxial diamond films after polishing and oxygen plasma etching. *Diamond and related materials*, 18(10):1205–1210, 2009.

[107] Junji Watanabe, Mutsumi Touge, and Takeshi Sakamoto. Ultraviolet-irradiated precision polishing of diamond and its related materials. *Diamond and related materials*, 39:14–19, 2013.

[108] K Yamamura, K Emori, R Sun, Y Ohkubo, K Endo, H Yamada, A Chayahara, and Y Mokuno. Damage-free highly efficient polishing of single-crystal diamond wafer by plasma-assisted polishing. *CIRP Annals*, 67(1):353–356, 2018.

[109] Nian Liu, Kohki Sugawara, Naoya Yoshitaka, Hideaki Yamada, Daisuke Takeuchi, Yuko Akabane, Kenichi Fujino, Kentaro Kawai, Kenta Arima, and Kazuya Yamamura. Damage-free highly efficient plasma-assisted polishing of a 20-mm square large mosaic single crystal diamond substrate. *Scientific Reports*, 10(1):1–7, 2020.

[110] Akihisa Kubota, Shuya Motoyama, and Mutsumi Touge. Development of an ultra-finishing technique for single-crystal diamond substrate utilizing an iron tool in h2o2 solution. *Diamond and Related Materials*, 64:177–183, 2016.

[111] Atsushi Hirata, Hitoshi Tokura, and Masanori Yoshikawa. Smoothing of chemically vapour deposited diamond films by ion beam irradiation. *Thin Solid Films*, 212(1-2):43–48, 1992.

[112] Jana Schmitt, Wim Nelissen, Ulrike Wallrabe, and Friedemann Völklein. Implementation of smooth nanocrystalline diamond microstructures by combining reactive ion etching and ion beam etching. *Diamond and Related Materials*, 79:164–172, 2017.

[113] Takashi Nagase, Hiroyuki Kato, SA Pahlovy, and Iwao Miyamoto. Nanosmoothing of single crystal diamond chips by 1 kev ar+ ion bombardment. *Journal of Vacuum Science & Technology B, Nanotechnology and Microelectronics: Materials, Processing, Measurement, and Phenomena*, 28(2):263–267, 2010.

[114] Timothy J Whetten, Angela A Armstead, Thomas A Grzybowski, and Arthur L Ruoff. Etching of diamond with argon and oxygen ion beams. *Journal of Vacuum Science & Technology A: Vacuum, Surfaces, and Films*, 2(2):477–480, 1984.

[115] F Frost, R Fechner, B Ziberi, J Völlner, D Flamm, and A Schindler. Large area smoothing of surfaces by ion bombardment: fundamentals and applications. *Journal of Physics: Condensed Matter*, 21(22):224026, 2009.

[116] Qiangmin Wei, Kun-Dar Li, Jie Lian, and Lumin Wang. Angular dependence of sputtering yield of amorphous and polycrystalline materials. *Journal of Physics D: Applied Physics*, 41(17):172002, 2008.

[117] Roger Smith and Keith Beardmore. Molecular dynamics studies of particle impacts with carbon-based materials. *Thin Solid Films*, 272(2):255–270, 1996.

[118] Charbel S Madi, Eitan Anzenberg, Karl F Ludwig Jr, and Michael J Aziz. Mass redistribution causes the structural richness of ion-irradiated surfaces. *Physical review letters*, 106(6):066101, 2011.

[119] Haig A Atikian, Amin Eftekharian, A Jafari Salim, Michael J Burek, Jennifer T Choy, A Hamed Majedi, and Marko Lončar. Superconducting nanowire single photon detector on diamond. *Applied Physics Letters*, 104(12):122602, 2014.

[120] Julia Heupel, Maximilian Pallmann, Jonathan Körber, Rolf Merz, Michael Kopnarski, Rainer Stöhr, Johann Peter Reithmaier, David Hunger, and Cyril Popov. Fabrication and characterization of single-crystal diamond membranes for quantum photonics with tunable microcavities. *Micromachines*, 11(12):1080, 2020.

[121] Maximilian Ruf, Mark IJspeert, Suzanne van Dam, Nick de Jong, Hans van den Berg, Guus Evers, and Ronald Hanson. Optically coherent nitrogen-vacancy centers in micrometer-thin etched diamond membranes. *Nano letters*, 19(6):3987–3992, 2019.

[122] Mutsumi Touge, Satoru Anan, Shogo Wada, Akihisa Kubota, Yoshitaka Nakanishi, and Junji Watanabe. Atomic-scale planarization of single crystal diamond substrates by ultraviolet rays assisted machining. In *Key Engineering Materials*, volume 447, pages 66–70. Trans Tech Publ, 2010.

[123] Akihisa Kubota, Sakae Fukuyama, Yuya Ichimori, and Mutsumi Touge. Surface smoothing of single-crystal diamond (100) substrate by polishing technique. *Diamond and related materials*, 24:59–62, 2012.

[124] T Trottenberg, A Spethmann, J Rutscher, and H Kersten. Non-electrostatic diagnostics for ion beams and sputter effects. *Plasma Physics and Controlled Fusion*, 54(12):124005, 2012.

[125] Yusaku Kawabata, Jun Taniguchi, and Iwao Miyamoto. XPS studies on damage evaluation of single-crystal diamond chips processed with ion beam etching and reactive ion beam assisted chemical etching. *Diamond and related materials*, 13(1):93–98, 2004.

[126] James F Ziegler, Matthias D Ziegler, and Jochen P Biersack. Srim–the stopping and range of ions in matter (2010). *Nuclear Instruments and Methods in Physics Research Section B: Beam Interactions with Materials and Atoms*, 268(11-12):1818–1823, 2010.

[127] Teodoro Graziosi, Sichen Mi, Marcell Kiss, and Niels Quack. Single crystal diamond micro-disk resonators by focused ion beam milling. *Apl Photonics*, 3(12):126101, 2018.

[128] Zongchen Liu, Haris Naeem Abbasi, Tian-Fei Zhu, Yan-Feng Wang, Jiao Fu, Feng Wen, Wei Wang, Shuwei Fan, Kaiyue Wang, and Hong-Xing Wang. Fabrication of micro lens array on diamond surface. *AIP Advances*, 9(12):125218, 2019.

[129] Wei Yuan, Li-Hua Li, Wing-Bun Lee, and Chang-Yuen Chan. Fabrication of microlens array and its application: a review. *Chinese Journal of Mechanical Engineering*, 31(1):16, 2018.

[130] Adrien Toros, Marcell Kristof Kiss, Teodoro Graziosi, Sichen Mi, R Berrazouane, M Naamoun, J Vukajlovic Plestina, P Gallo, and Niels Quack. Reactive ion etching

of single crystal diamond by inductively coupled plasma: State of the art and catalog of recipes. *Diamond and Related Materials*, (108):107839, 2020.

[131] Scott A Norris and Michael J Aziz. Ion-induced nanopatterning of silicon: Toward a predictive model. *Applied Physics Reviews*, 6(1):011311, 2019.

[132] Thomas Michael Mayer, David Price Adams, MJ Vasile, and KM Archuleta. Morphology evolution on diamond surfaces during ion sputtering. *Journal of Vacuum Science & Technology A: Vacuum, Surfaces, and Films*, 23(6):1579–1587, 2005.

[133] DP Adams, MJ Vasile, TM Mayer, and VC Hodges. Focused ion beam milling of diamond: effects of H_2O on yield, surface morphology and microstructure. *Journal of Vacuum Science & Technology B: Microelectronics and Nanometer Structures Processing, Measurement, and Phenomena*, 21(6):2334–2343, 2003.

[134] A Datta, Yuh-Renn Wu, and YL Wang. Real-time observation of ripple structure formation on a diamond surface under focused ion-beam bombardment. *Physical Review B*, 63(12):125407, 2001.

[135] K Takahiro, K Ozaki, K Kawatsura, S Nagata, S Yamamoto, K Narumi, and H Naramoto. Ion-induced self-organized ripple patterns on graphite and diamond surfaces. *Applied surface science*, 256(4):972–975, 2009.

[136] Takashi Nagase, Hiroyuki Kato, Shahjada A Pahlovy, and Iwao Miyamoto. Surface morphology analysis of natural single crystal diamond chips bombarded with ar+ ion beam. *Vacuum*, 84(12):1423–1426, 2010.

[137] SF Mahmud, SA Pahlovy, Yoshiko Sato, and Iwao Miyamoto. Facet and ripple formations on single crystal diamond tools machined by low energy oxygen ion beam. *Diamond and related materials*, 20(7):1056–1060, 2011.

[138] Daniel A Pearson and R Mark Bradley. Theory of terraced topographies produced by oblique-incidence ion bombardment of solid surfaces. *Journal of Physics: Condensed Matter*, 27(1):015010, 2014.

[139] Noriaki Toyoda, Buddhi Tilakaratne, Iram Saleem, and Wei-Kan Chu. Cluster beams, nano-ripples, and bio applications. *Applied Physics Reviews*, 6(2):020901, 2019.

[140] M Navez, D Chaperot, and C Sella. Microscopie electronique-etude de lattaque du verre par bombardement ionique. *Comptes Rendus Hebdomadaires Des Seances De L Academie Des Sciences*, 254(2):240, 1962.

[141] F Vasiliu, IA Teodorescu, and F Glodeanu. Sem investigations of iron surface ion erosion as a function of specimen temperature and incidence angle. *Journal of Materials Science*, 10(3):399–405, 1975.

[142] DJ Barber, FC Frank, M Moss, JW Steeds, and IST Tsong. Prediction of ion-bombarded surface topographies using frank's kinematic theory of crystal dissolution. *Journal of Materials Science*, 8(7):1030–1040, 1973.

[143] Sung I Park, A Marshall, RH Hammond, TH Geballe, and J Talvacchio. The role of ion-beam cleaning in the growth of strained-layer epitaxial thin transition metal films. *Journal of Materials Research*, 2(4):446–455, 1987.

[144] P Süle and K-H Heinig. The molecular dynamics simulation of ion-induced ripple growth. *The Journal of chemical physics*, 131(20):204704, 2009.

[145] Adrian Keller and Stefan Facsko. Ion-induced nanoscale ripple patterns on si surfaces: theory and experiment. *Materials*, 3(10):4811–4841, 2010.

[146] Scott A Norris, Juha Samela, Laura Bukonte, Marie Backman, Flyura Djurabekova, Kai Nordlund, Charbel S Madi, Michael P Brenner, and Michael J Aziz. Molecular dynamics of single-particle impacts predicts phase diagrams for large scale pattern formation. *Nature communications*, 2(1):1–6, 2011.

[147] Matt P Harrison and R Mark Bradley. Crater function approach to ion-induced nanoscale pattern formation: Craters for flat surfaces are insufficient. *Physical Review B*, 89(24):245401, 2014.

[148] R Mark Bradley and James ME Harper. Theory of ripple topography induced by ion bombardment. *Journal of Vacuum Science & Technology A: Vacuum, Surfaces, and Films*, 6(4):2390–2395, 1988.

[149] Sebastian Vogel and Stefan J Linz. How ripples turn into dots: Modeling ion-beam erosion under oblique incidence. *EPL (Europhysics Letters)*, 76(5):884, 2006.

[150] Rodolfo Cuerno and Albert-László Barabási. Dynamic scaling of ion-sputtered surfaces. *Physical review letters*, 74(23):4746, 1995.

[151] GI Sivashinsky. Nonlinear analysis of hydrodynamic instability in laminar flames—i. derivation of basic equations. *AcAau*, 4(11):1177–1206, 1977.

[152] Yoshiki Kuramoto and Toshio Tsuzuki. Persistent propagation of concentration waves in dissipative media far from thermal equilibrium. *Progress of theoretical physics*, 55(2):356–369, 1976.

[153] Stefan Facsko, Thomas Dekorsy, Clemens Koerdt, Cyril Trappe, Heinrich Kurz, Alexander Vogt, and Hans L Hartnagel. Formation of ordered nanoscale semiconductor dots by ion sputtering. *Science*, 285(5433):1551–1553, 1999.

[154] Stefan Facsko, Thomas Bobek, Arne Stahl, Heinrich Kurz, and Thomas Dekorsy. Dissipative continuum model for self-organized pattern formation during ion-beam erosion. *Physical Review B*, 69(15):153412, 2004.

[155] C Diddens and Stefan J Linz. Redeposition during ion-beam erosion can stabilize well-ordered nanostructures. *EPL (Europhysics Letters)*, 104(1):17010, 2013.

[156] Christian Diddens and Stefan J Linz. Continuum modeling of particle redeposition during ion-beam erosion. *The European Physical Journal B*, 88(7):190, 2015.

[157] Marco Altomare, Nhat Truong Nguyen, and Patrik Schmuki. Templated dewetting: designing entirely self-organized platforms for photocatalysis. *Chemical science*, 7(12):6865–6886, 2016.

[158] Jongpil Ye and Carl V Thompson. Templated solid-state dewetting to controllably produce complex patterns. *Advanced Materials*, 23(13):1567–1571, 2011.

[159] Wei Jiang, Yan Wang, David J Srolovitz, and Weizhu Bao. Solid-state dewetting on curved substrates. *Physical Review Materials*, 2(11):113401, 2018.

[160] Lukas Novotny and Niek Van Hulst. Antennas for light. *Nature photonics*, 5(2):83–90, 2011.

[161] Jorge Zuloaga, Emil Prodan, and Peter Nordlander. Quantum description of the plasmon resonances of a nanoparticle dimer. *Nano letters*, 9(2):887–891, 2009.

[162] Kimiyoshi Ichikawa, Kengo Kurone, Hideyuki Kodama, Kazuhiro Suzuki, and Atsuhito Sawabe. High crystalline quality heteroepitaxial diamond using grid-patterned nucleation and growth on ir. *Diamond and Related Materials*, 94:92–100, 2019.

[163] Yun Zhao, Yanzhao Guo, Liangzhen Lin, Yuting Zheng, Lifu Hei, Jinlong Liu, Junjun Wei, Liangxian Chen, and Chengming Li. Comparison of the quality of single-crystal diamonds grown on two types of seed substrates by mpcvd. *Journal of Crystal Growth*, 491:89–96, 2018.

[164] Matthias Schreck, Michael Mayr, Michael Weinl, Martin Fischer, and Stefan Gsell. Liftoff of single crystal diamond by epitaxial lateral overgrowth using sio2 masks. *Diamond and Related Materials*, 101:107606, 2020.

[165] Fei Gao, Zhihong Huang, Benjamin Feigel, Jürgen Van Erps, Hugo Thienpont, Raymond G Beausoleil, and Nathalie Vermeulen. Low-loss millimeter-length waveguides and grating couplers in single-crystal diamond. *Journal of Lightwave Technology*, 34(23):5576–5582, 2016.

[166] Fei Gao, Jürgen Van Erps, Zhihong Huang, Hugo Thienpont, Raymond G Beausoleil, and Nathalie Vermeulen. Directional coupler based on single-crystal diamond waveguides. *IEEE Journal of Selected Topics in Quantum Electronics*, 24(6):1–9, 2018.

[167] Fei Gao, Jürgen Van Erps, Zhihong Huang, Hugo Thienpont, Raymond G Beausoleil, and Nathalie Vermeulen. Down-scaling grating couplers and waveguides in single-crystal diamond for vis-uv operation. *Journal of Physics: Photonics*, 1(1):015003, 2018.

[168] Birgit JM Hausmann, Brendan Shields, Qimin Quan, Patrick Maletinsky, Murray Mc-Cutcheon, Jennifer T Choy, Tom M Babinec, Alexander Kubanek, Amir Yacoby, Mikhail D Lukin, et al. Integrated diamond networks for quantum nanophotonics. *Nano letters*, 12(3):1578–1582, 2012.

[169] BJM Hausmann, I Bulu, V Venkataraman, P Deotare, and Marko Lončar. Diamond nonlinear photonics. *Nature Photonics*, 8(5):369–374, 2014.

[170] VS Ilchenko, AM Bennett, P Santini, AA Savchenkov, AB Matsko, and L Maleki. Whispering gallery mode diamond resonator. *Optics letters*, 38(21):4320–4323, 2013.

[171] Pawel Latawiec, Vivek Venkataraman, Michael J Burek, Birgit JM Hausmann, Irfan Bulu, and Marko Lončar. On-chip diamond raman laser. *Optica*, 2(11):924–928, 2015.

[172] Michel Challier, Selda Sonusen, Arne Barfuss, Dominik Rohner, Daniel Riedel, Johannes Koelbl, Marc Ganzhorn, Patrick Appel, Patrick Maletinsky, and Elke Neu. Advanced fabrication of single-crystal diamond membranes for quantum technologies. *Micromachines*, 9(4):148, 2018.

[173] Ye Tao and Christian Degen. Facile fabrication of single-crystal-diamond nanostructures with ultrahigh aspect ratio. *Advanced Materials*, 25(29):3962–3967, 2013.

[174] Y Tao, Jens M Boss, BA Moores, and Christian L Degen. Single-crystal diamond nanomechanical resonators with quality factors exceeding one million. *Nature communications*, 5(1):1–8, 2014.

[175] NR Parikh, JD Hunn, E McGucken, ML Swanson, CW White, RA Rudder, DP Malta, JB Posthill, and RJ Markunas. Single-crystal diamond plate liftoff achieved by ion implantation and subsequent annealing. *Applied physics letters*, 61(26):3124–3126, 1992.

[176] Afaq Habib Piracha, Kumaravelu Ganesan, Desmond WM Lau, Alastair Stacey, Liam P McGuinness, Snjezana Tomljenovic-Hanic, and Steven Prawer. Scalable fabrication of high-quality, ultra-thin single crystal diamond membrane windows. *Nanoscale*, 8(12):6860–6865, 2016.

[177] JC Piñero, J de Vecchy, D Fernández, G Alba, J Widiez, L Di Cioccio, F Lloret, D Araujo, and J Pernot. Lattice performance during initial steps of the smart-cut™ process in semiconducting diamond: A stem study. *Applied Surface Science*, 528:146998, 2020.

[178] Barbara A Fairchild, Paolo Olivero, Sergey Rubanov, Andrew D Greentree, Felix Waldermann, Robert A Taylor, Ian Walmsley, Jason M Smith, Shane Huntington, Brant C Gibson, et al. Fabrication of ultrathin single-crystal diamond membranes. *Advanced Materials*, 20(24):4793–4798, 2008.

[179] Barbara A Fairchild, Sergey Rubanov, Desmond WM Lau, Marc Robinson, Irene Suarez-Martinez, Nigel Marks, Andrew D Greentree, Dougal McCulloch, and Steven Prawer.

Mechanism for the amorphisation of diamond. *Advanced Materials*, 24(15):2024–2029, 2012.

[180] Mike Marchywka, Pehr E Pehrsson, Steven C Binari, and Daniel Moses. Electrochemical patterning of amorphous carbon on diamond. *Journal of The Electrochemical Society*, 140(2):L19, 1993.

[181] Andrew P Magyar, Jonathan C Lee, Andi M Limarga, Igor Aharonovich, Fabian Rol, David R Clarke, Mengbing Huang, and Evelyn L Hu. Fabrication of thin, luminescent, single-crystal diamond membranes. *Applied Physics Letters*, 99(8):081913, 2011.

[182] H Okushi, H Watanabe, S Ri, S Yamanaka, and D Takeuchi. Device-grade homoepitaxial diamond film growth. *Journal of crystal growth*, 237:1269–1276, 2002.

[183] Igor Aharonovich, Jonathan C Lee, Andrew P Magyar, Bob B Buckley, Christopher G Yale, David D Awschalom, and Evelyn L Hu. Homoepitaxial growth of single crystal diamond membranes for quantum information processing. *Advanced materials*, 24(10):OP54–OP59, 2012.

[184] TN Tran Thi, Bruno Fernandez, David Eon, Etienne Gheeraert, Juergen Haertwig, T Lafford, A Perrat-Mabilon, C Peaucelle, P Olivero, and Etienne Bustarret. Ultra-smooth single crystal diamond surfaces resulting from implantation and lift-off processes. *physica status solidi (a)*, 208(9):2057–2061, 2011.

[185] Kerem Bray, Blake Regan, and Igor Aharonovich. Chapter five - diamond membranes for photonic devices. In Christoph E. Nebel, Igor Aharonovich, Norikazu Mizuochi, and Mutsuko Hatano, editors, *Diamond for Quantum Applications Part 2*, volume 104 of *Semiconductors and Semimetals*, pages 173–217. Elsevier, 2021.

[186] Marcell Kristof Kiss. Advanced diamond microfabrication for microoptics and photonics. Technical report, EPFL, 2019.

[187] Takashi Matsumae, Yuichi Kurashima, Hitoshi Umezawa, and Hideki Takagi. Direct bonding of Diamond and Si substrates at low temperatures under atmospheric conditions. In *2020 IEEE 70th Electronic Components and Technology Conference (ECTC)*, pages 1436–1441. IEEE, 2020.

[188] Takashi Matsumae, Yuichi Kurashima, Hideki Takagi, Hitoshi Umezawa, and Eiji Higurashi. Low-temperature direct bonding of diamond (100) substrate on si wafer under atmospheric conditions. *Scripta Materialia*, 191:52–55.

[189] Takashi Matsumae, Yuichi Kurashima, Hitoshi Umezawa, and Hideki Takagi. Hydrophilic direct bonding of diamond (111) substrate using treatment with h2so4/h2o2. *Japanese Journal of Applied Physics*, 59(SB):SBBA01, 2019.

[190] Jianbo Liang, Satoshi Masuya, Makoto Kasu, and Naoteru Shigekawa. Realization of direct bonding of single crystal diamond and si substrates. *Applied Physics Letters*, 110(11):111603, 2017.

[191] Jianbo Liang, Satoshi Masuya, Seongwoo Kim, Toshiyuki Oishi, Makoto Kasu, and Naoteru Shigekawa. Stability of diamond/si bonding interface during device fabrication process. *Applied Physics Express*, 12(1):016501, 2018.

[192] Jianbo Liang, Yan Zhou, Satoshi Masuya, Filip Gucmann, Manikant Singh, James Pomeroy, Seongwoo Kim, Martin Kuball, Makoto Kasu, and Naoteru Shigekawa. Annealing effect of surface-activated bonded diamond/si interface. *Diamond and Related Materials*, 93:187–192, 2019.

[193] Jan Haisma, Bert ACM Spierings, Udo KP Biermann, and Aart A van Gorkum. Diversity and feasibility of direct bonding: a survey of a dedicated optical technology. *Applied Optics*, 33(7):1154–1169, 1994.

[194] CF Wang, EL Hu, J Yang, and JE Butler. Fabrication of suspended single crystal diamond devices by electrochemical etch. *Journal of Vacuum Science & Technology B: Microelectronics and Nanometer Structures Processing, Measurement, and Phenomena*, 25(3):730–733, 2007.

[195] Kevin A Shaw, Z Lisa Zhang, and Noel C MacDonald. Scream i: a single mask, single-crystal silicon, reactive ion etching process for microelectromechanical structures. *Sensors and Actuators A: Physical*, 40(1):63–70, 1994.

[196] Noel H Wan, Sara Mouradian, and Dirk Englund. Two-dimensional photonic crystal slab nanocavities on bulk single-crystal diamond. *Applied Physics Letters*, 112(14):141102, 2018.

[197] Haig A Atikian, Pawel Latawiec, Michael J Burek, Young-Ik Sohn, Srujan Meesala, Normand Gravel, Ammar B Kouki, and Marko Lončar. Freestanding nanostructures via reactive ion beam angled etching. *APL Photonics*, 2(5):051301, 2017.

[198] GD Boyd, LA Coldren, and FG Storz. Directional reactive ion etching at oblique angles. *Applied Physics Letters*, 36(7):583–585, 1980.

[199] Michael J Burek, Yiwen Chu, Madelaine SZ Liddy, Parth Patel, Jake Rochman, Srujan Meesala, Wooyoung Hong, Qimin Quan, Mikhail D Lukin, and Marko Lončar. High quality-factor optical nanocavities in bulk single-crystal diamond. *Nature communications*, 5(1):1–7, 2014.

[200] Pawel Latawiec, Michael J Burek, Young-Ik Sohn, and Marko Lončar. Faraday cage angled-etching of nanostructures in bulk dielectrics. *Journal of Vacuum Science & Technology B, Nanotechnology and Microelectronics: Materials, Processing, Measurement, and Phenomena*, 34(4):041801, 2016.

[201] I Bayn, S Mouradian, L Li, JA Goldstein, T Schröder, J Zheng, EH Chen, O Gaathon, M Lu, A Stein, et al. Fabrication of triangular nanobeam waveguide networks in bulk diamond using single-crystal silicon hard masks. *Applied Physics Letters*, 105(21):211101, 2014.

[202] A Sobiesierski, S Shabbir, DM Beggs, S Thomas, R Taylor, AJ Bennett, and GP Gough. Faraday-cage-assisted etching of suspended gallium nitride nanostructures. *AIP Advances*.

[203] N Okada, K Nojima, N Ishibashi, K Nagatoshi, N Itagaki, R Inomoto, S Motoyama, T Kobayashi, and K Tadatomo. Formation of distinctive structures of gan by inductively-coupled-plasma and reactive ion etching under optimized chemical etching conditions. *AIP Advances*, 7(6):065111, 2017.

[204] I Friel, SL Clewes, HK Dhillon, N Perkins, DJ Twitchen, and GA Scarsbrook. Control of surface and bulk crystalline quality in single crystal diamond grown by chemical vapour deposition. *Diamond and Related Materials*, 18(5-8):808–815, 2009.

[205] Seong-Woo Jeon, Junghyun Lee, Hojoong Jung, Sang-Wook Han, Young-Wook Cho, Yong-Su Kim, Hyang-Tag Lim, Yanghee Kim, Matthias Niethammer, Weon Cheol Lim, et al. Bright nitrogen-vacancy centers in diamond inverted nanocones. *ACS Photonics*, 7(10):2739–2747, 2020.

[206] Michael J Burek, Charles Meuwly, Ruffin E Evans, Mihir K Bhaskar, Alp Sipahigil, Srujan Meesala, Bartholomeus Machielse, Denis D Sukachev, Christian T Nguyen, Jose L Pacheco, et al. Fiber-coupled diamond quantum nanophotonic interface. *Physical Review Applied*, 8(2):024026, 2017.

[207] Mihir K Bhaskar, Denis D Sukachev, Alp Sipahigil, Ruffin E Evans, Michael J Burek, Christian T Nguyen, Lachlan J Rogers, Petr Siyushev, Mathias H Metsch, Hongkun Park, et al. Quantum nonlinear optics with a germanium-vacancy color center in a nanoscale diamond waveguide. *Physical review letters*, 118(22):223603, 2017.

[208] Galina Popovici, RG Wilson, T Sung, MA Prelas, and S Khasawinah. Diffusion of boron, lithium, oxygen, hydrogen, and nitrogen in type iia natural diamond. *Journal of applied physics*, 77(10):5103–5106, 1995.

[209] Jung-Hun Seo, Henry Wu, Solomon Mikael, Hongyi Mi, James P Blanchard, Giri Venkataramanan, Weidong Zhou, Shaoqin Gong, Dane Morgan, and Zhenqiang Ma. Thermal diffusion boron doping of single-crystal natural diamond. *Journal of Applied Physics*, 119(20):205703, 2016.

[210] Gopalakrishnan Balasubramanian, Philipp Neumann, Daniel Twitchen, Matthew Markham, Roman Kolesov, Norikazu Mizuochi, Junichi Isoya, Jocelyn Achard, Johannes Beck, Julia Tissler, et al. Ultralong spin coherence time in isotopically engineered diamond. *Nature materials*, 8(5):383–387, 2009.

[211] Jonas Nils Becker and Elke Neu. The silicon vacancy center in diamond. 2020.

[212] J Achard, Vincent Jacques, and A Tallaire. Chemical vapour deposition diamond single crystals with nitrogen-vacancy centres: a review of material synthesis and technology

for quantum sensing applications. *Journal of Physics D: Applied Physics*, 53(31):313001, 2020.

[213] A Chayahara, Y Mokuno, Y Horino, Y Takasu, H Kato, H Yoshikawa, and N Fujimori. The effect of nitrogen addition during high-rate homoepitaxial growth of diamond by microwave plasma cvd. *Diamond and related materials*, 13(11-12):1954–1958, 2004.

[214] Gai Wu, Qijun Wang, Yanxue Wu, Xiang Sun, Jia Liao, Junheng Pan, Meihua Chen, Makoto Kasu, and Sheng Liu. Evolution of defects, morphologies and fundamental growth characteristics of cvd diamond films induced by nitrogen addition. *Materials Today Communications*, 25:101504, 2020.

[215] Y Su, HD Li, SH Cheng, Q Zhang, QL Wang, XY Lv, GT Zou, XQ Pei, and JG Xie. Effect of n2o on high-rate homoepitaxial growth of cvd single crystal diamonds. *Journal of crystal growth*, 351(1):51–55, 2012.

[216] N Mizuochi, H Watanabe, J Isoya, H Okushi, and S Yamasaki. Hydrogen-related defects in single crystalline cvd homoepitaxial diamond film studied by epr. *Diamond and related materials*, 13(4-8):765–768, 2004.

[217] JR Rabeau, YL Chin, S Prawer, F Jelezko, T Gaebel, and J Wrachtrup. Fabrication of single nickel-nitrogen defects in diamond by chemical vapor deposition. *Applied Physics Letters*, 86(13):131926, 2005.

[218] Kerem Bray, Dmitry Yu Fedyanin, Igor A Khramtsov, Maryna O Bilokur, Blake Regan, Milos Toth, and Igor Aharonovich. Electrical excitation and charge-state conversion of silicon vacancy color centers in single-crystal diamond membranes. *Applied Physics Letters*, 116(10):101103, 2020.

[219] Blake Regan, Sejeong Kim, Anh TH Ly, Aleksandra Trycz, Kerem Bray, Kumaravelu Ganesan, Milos Toth, and Igor Aharonovich. Photonic devices fabricated from (111)-oriented single crystal diamond. *InfoMat*, 2020.

[220] LC Hao, Y Shen, XD Yang, Y Bian, QQ Du, DY Liu, WK Zhao, JD Ye, K Tang, HP Wu, et al. Tailoring of nitrogen-vacancy colour centers in diamond epilayers by in situ sulfur and nitrogen anion engineering. *Journal of Physics D: Applied Physics*, 53(7):075107, 2019.

[221] Hitoshi Ishiwata, Makoto Nakajima, Kosuke Tahara, Hayato Ozawa, Takayuki Iwasaki, and Mutsuko Hatano. Perfectly aligned shallow ensemble nitrogen-vacancy centers in (111) diamond. *Applied Physics Letters*, 111(4):043103, 2017.

[222] Linh My Pham, N Bar-Gill, D Le Sage, C Belthangady, A Stacey, M Markham, DJ Twitchen, Mikhail D Lukin, and Ronald L Walsworth. Enhanced metrology using preferential orientation of nitrogen-vacancy centers in diamond. *Physical Review B*, 86(12):121202, 2012.

[223] ED Herbschleb, H Kato, Y Maruyama, T Danjo, T Makino, S Yamasaki, I Ohki, K Hayashi, H Morishita, M Fujiwara, et al. Ultra-long coherence times amongst room-temperature solid-state spins. *Nature communications*, 10(1):1–6, 2019.

[224] Jonathan C Lee, David O Bracher, Shanying Cui, Kenichi Ohno, Claire A McLellan, Xingyu Zhang, Paolo Andrich, Benjamin Alemán, Kasey J Russell, Andrew P Magyar, et al. Deterministic coupling of delta-doped nitrogen vacancy centers to a nanobeam photonic crystal cavity. *Applied Physics Letters*, 105(26):261101, 2014.

[225] Claire A McLellan, Bryan A Myers, Stephan Kraemer, Kenichi Ohno, David D Awschalom, and Ania C Bleszynski Jayich. Patterned formation of highly coherent nitrogen-vacancy centers using a focused electron irradiation technique. *Nano letters*, 16(4):2450–2454, 2016.

[226] AM Edmonds, UFS D'Haenens-Johansson, RJ Cruddace, ME Newton, K-MC Fu, C Santori, RG Beausoleil, DJ Twitchen, and ML Markham. Production of oriented nitrogen-vacancy color centers in synthetic diamond. *Physical Review B*, 86(3):035201, 2012.

[227] Mildred S Dresselhaus and Rafael Kalish. *Ion implantation in diamond, graphite and related materials*, volume 22. Springer Science & Business Media, 2013.

[228] Boris Naydenov, Friedemann Reinhard, Anke Lämmle, V Richter, Rafi Kalish, Ulrika FS D'Haenens-Johansson, Mark Newton, Fedor Jelezko, and Jörg Wrachtrup. Increasing the coherence time of single electron spins in diamond by high temperature annealing. *Applied Physics Letters*, 97(24):242511, 2010.

[229] JO Orwa, C Santori, KMC Fu, B Gibson, D Simpson, I Aharonovich, A Stacey, A Cimmino, P Balog, M Markham, et al. Engineering of nitrogen-vacancy color centers in high purity diamond by ion implantation and annealing. *Journal of applied physics*, 109(8):083530, 2011.

[230] Tim Schröder, Matthew E Trusheim, Michael Walsh, Luozhou Li, Jiabao Zheng, Marco Schukraft, Alp Sipahigil, Ruffin E Evans, Denis D Sukachev, Christian T Nguyen, et al. Scalable focused ion beam creation of nearly lifetime-limited single quantum emitters in diamond nanostructures. *Nature communications*, 8(1):1–7, 2017.

[231] M Schukraft, J Zheng, T Schröder, SL Mouradian, M Walsh, ME Trusheim, H Bakhru, and DR Englund. Invited article: Precision nanoimplantation of nitrogen vacancy centers into diamond photonic crystal cavities and waveguides. *Apl Photonics*, 1(2):020801, 2016.

[232] Sébastien Pezzagna, Dominik Wildanger, Paul Mazarov, Andreas D Wieck, Yanko Sarov, Ivo Rangelow, Boris Naydenov, Fedor Jelezko, Stefan W Hell, and Jan Meijer. Nanoscale engineering and optical addressing of single spins in diamond. *small*, 6(19):2117–2121, 2010.

[233] T Staudacher, F Ziem, L Häussler, R Stöhr, S Steinert, F Reinhard, J Scharpf, A Denisenko, and J Wrachtrup. Enhancing the spin properties of shallow implanted nitrogen vacancy centers in diamond by epitaxial overgrowth. *Applied Physics Letters*, 101(21):212401, 2012.

[234] Margarita Lesik, Nicole Raatz, Alexandre Tallaire, Piernicola Spinicelli, Roger John, Jocelyn Achard, Alix Gicquel, Vincent Jacques, Jean-François Roch, Jan Meijer, et al. Production of bulk nv centre arrays by shallow implantation and diamond cvd overgrowth. *Physica status solidi (a)*, 213(10):2594–2600, 2016.

[235] Alison E Rugar, Haiyu Lu, Constantin Dory, Shuo Sun, Patrick J McQuade, Zhi-Xun Shen, Nicholas A Melosh, and Jelena Vuckovic. Generation of tin-vacancy centers in diamond via shallow ion implantation and subsequent diamond overgrowth. *Nano Letters*, 20(3):1614–1619, 2020.

[236] Felipe Fávaro De Oliveira, Denis Antonov, Ya Wang, Philipp Neumann, Seyed Ali Momenzadeh, Timo Häußermann, Alberto Pasquarelli, Andrej Denisenko, and Jörg Wrachtrup. Tailoring spin defects in diamond by lattice charging. *Nature communications*, 8(1):1–8, 2017.

[237] Ossi Lehtinen, Boris Naydenov, Pia Börner, Kristina Melentjevic, Christoph Müller, Liam Paul McGuinness, Sebastien Pezzagna, Jan Meijer, Ute Kaiser, and Fedor Jelezko. Molecular dynamics simulations of shallow nitrogen and silicon implantation into diamond. *Physical Review B*, 93(3):035202, 2016.

[238] Suzanne B van Dam, Michael Walsh, Maarten J Degen, Eric Bersin, Sara L Mouradian, Airat Galiullin, Maximilian Ruf, Mark IJspeert, Tim H Taminiau, Ronald Hanson, et al. Optical coherence of diamond nitrogen-vacancy centers formed by ion implantation and annealing. *Physical Review B*, 99(16):161203, 2019.

[239] Ignas Lekavicius and Hailin Wang. Optical coherence of implanted silicon vacancy centers in thin diamond membranes. *Optics Express*, 27(22):31299–31306, 2019.

[240] Ruffin E Evans, Alp Sipahigil, Denis D Sukachev, Alexander S Zibrov, and Mikhail D Lukin. Narrow-linewidth homogeneous optical emitters in diamond nanostructures via silicon ion implantation. *Physical Review Applied*, 5(4):044010, 2016.

[241] JO Orwa, AD Greentree, I Aharonovich, ADC Alves, J Van Donkelaar, A Stacey, and S Prawer. Fabrication of single optical centres in diamond—a review. *Journal of Luminescence*, 130(9):1646–1654, 2010.

[242] JO Orwa, I Aharonovich, F Jelezko, G Balasubramanian, P Balog, M Markham, DJ Twitchen, AD Greentree, and S Prawer. Nickel related optical centres in diamond created by ion implantation. *Journal of applied physics*, 107(9):093512, 2010.

[243] J Schwartz, S Aloni, DF Ogletree, M Tomut, M Bender, D Severin, C Trautmann, IW Rangelow, and T Schenkel. Local formation of nitrogen-vacancy centers in diamond by swift heavy ions. *Journal of Applied Physics*, 116(21):214107, 2014.

[244] D Farfurnik, N Alfasi, S Masis, Y Kauffmann, E Farchi, Y Romach, Y Hovav, E Buks, and N Bar-Gill. Enhanced concentrations of nitrogen-vacancy centers in diamond through tem irradiation. *Applied Physics Letters*, 111(12):123101, 2017.

[245] Julian Schwartz, Shaul Aloni, D Frank Ogletree, and Thomas Schenkel. Effects of low-energy electron irradiation on formation of nitrogen–vacancy centers in single-crystal diamond. *New Journal of Physics*, 14(4):043024, 2012.

[246] Youying Rong, Ke Cheng, Zhiping Ju, Chengda Pan, Qiang Ma, Shikang Liu, Si Shen, Botao Wu, and Tianqing Jia. Bright near-surface silicon vacancy centers in diamond fabricated by femtosecond laser ablation. *Optics letters*, 44(15):3793–3796, 2019.

[247] Yan Liu, Gengxu Chen, Min Song, Xueting Ci, Botao Wu, E Wu, and Heping Zeng. Fabrication of nitrogen vacancy color centers by femtosecond pulse laser illumination. *Optics express*, 21(10):12843–12848, 2013.

[248] Yu-Chen Chen, Patrick S Salter, Sebastian Knauer, Laiyi Weng, Angelo C Frangeskou, Colin J Stephen, Shazeaa N Ishmael, Philip R Dolan, Sam Johnson, Ben L Green, et al. Laser writing of coherent colour centres in diamond. *Nature Photonics*, 11(2):77–80, 2017.

[249] Yu-Chen Chen, Benjamin Griffiths, Laiyi Weng, Shannon S Nicley, Shazeaa N Ishmael, Yashna Lekhai, Sam Johnson, Colin J Stephen, Ben L Green, Gavin W Morley, et al. Laser writing of individual nitrogen-vacancy defects in diamond with near-unity yield. *Optica*, 6(5):662–667, 2019.

[250] CJ Stephen, BL Green, YND Lekhai, L Weng, P Hill, S Johnson, AC Frangeskou, PL Diggle, Y-C Chen, MJ Strain, et al. Deep three-dimensional solid-state qubit arrays with long-lived spin coherence. *Physical Review Applied*, 12(6):064005, 2019.

[251] Donatella Carbonera. Optically detected magnetic resonance (odmr) of photoexcited triplet states. *Photosynthesis research*, 102(2-3):403, 2009.

[252] Brendon C Rose, Ding Huang, Zi-Huai Zhang, Paul Stevenson, Alexei M Tyryshkin, Sorawis Sangtawesin, Srikanth Srinivasan, Lorne Loudin, Matthew L Markham, Andrew M Edmonds, et al. Observation of an environmentally insensitive solid-state spin defect in diamond. *Science*, 361(6397):60–63, 2018.

[253] Kay D Jahnke, Alp Sipahigil, Jan M Binder, Marcus W Doherty, Mathias Metsch, Lachlan J Rogers, Neil B Manson, Mikhail D Lukin, and Fedor Jelezko. Electron–phonon processes of the silicon-vacancy centre in diamond. *New Journal of Physics*, 17(4):043011, 2015.

[254] Yuki Doi, Takahiro Fukui, Hiromitsu Kato, Toshiharu Makino, Satoshi Yamasaki, Toshiyuki Tashima, Hiroki Morishita, Shinji Miwa, Fedor Jelezko, Yoshishige Suzuki, et al. Pure negatively charged state of the nv center in n-type diamond. *Physical Review B*, 93(8):081203, 2016.

[255] Karin Groot-Berning, Nicole Raatz, Inga Dobrinets, Margarita Lesik, Piernicola Spinicelli, Alexandre Tallaire, Jocelyn Achard, Vincent Jacques, Jean-François Roch, Alexander M Zaitsev, et al. Passive charge state control of nitrogen-vacancy centres in diamond using phosphorous and boron doping. *physica status solidi (a)*, 211(10):2268–2273, 2014.

[256] UFS D'Haenens-Johansson, AM Edmonds, BL Green, ME Newton, G Davies, PM Martineau, RUA Khan, and DJ Twitchen. Optical properties of the neutral silicon split-vacancy center in diamond. *Physical Review B*, 84(24):245208, 2011.

[257] MV Hauf, B Grotz, B Naydenov, M Dankerl, S Pezzagna, J Meijer, F Jelezko, J Wrachtrup, M Stutzmann, FJPRB Reinhard, et al. Chemical control of the charge state of nitrogen-vacancy centers in diamond. *Physical Review B*, 83(8):081304, 2011.

[258] Toby W Shanley, Aiden A Martin, Igor Aharonovich, and Milos Toth. Localized chemical switching of the charge state of nitrogen-vacancy luminescence centers in diamond. *Applied Physics Letters*, 105(6):063103, 2014.

[259] David A Hopper, Joseph D Lauigan, Tzu-Yung Huang, and Lee C Bassett. Real-time charge initialization of diamond nitrogen-vacancy centers for enhanced spin readout. *Physical Review Applied*, 13(2):024016, 2020.

[260] P Siyushev, H Pinto, M Vörös, A Gali, Fedor Jelezko, and J Wrachtrup. Optically controlled switching of the charge state of a single nitrogen-vacancy center in diamond at cryogenic temperatures. *Physical review letters*, 110(16):167402, 2013.

[261] Y Doi, T Makino, H Kato, D Takeuchi, M Ogura, H Okushi, H Morishita, T Tashima, S Miwa, S Yamasaki, et al. Deterministic electrical charge-state initialization of single nitrogen-vacancy center in diamond. *Physical Review X*, 4(1):011057, 2014.

[262] AM Zaitsev, W Wang, KS Moe, and P Johnson. Spectroscopic studies of yellow nitrogen-doped cvd diamonds. *Diamond and Related Materials*, 68:51–61, 2016.

[263] RUA Khan, BL Cann, PM Martineau, J Samartseva, JJP Freeth, SJ Sibley, CB Hartland, ME Newton, HK Dhillon, and DJ Twitchen. Colour-causing defects and their related optoelectronic transitions in single crystal cvd diamond. *Journal of Physics: Condensed Matter*, 25(27):275801, 2013.

[264] Simone Salustro, Fabien Pascale, William C Mackrodt, Corentin Ravoux, Alessandro Erba, and Roberto Dovesi. Interstitial nitrogen atoms in diamond. a quantum mechanical investigation of its electronic and vibrational properties. *Physical Chemistry Chemical Physics*, 20(24):16615–16624, 2018.

[265] Neil B Manson, Morgan Hedges, Michael SJ Barson, Rose Ahlefeldt, Marcus W Doherty, Hiroshi Abe, Takeshi Ohshima, and Matthew J Sellars. Nv—n+ pair centre in 1b diamond. *New Journal of Physics*, 20(11):113037, 2018.

[266] E Baskin, A Reznik, D Saada, Joan Adler, and R Kalish. Model for the defect-related electrical conductivity in ion-damaged diamond. *Physical Review B*, 64(22):224110, 2001.

[267] Alan T Collins, Lars Allers, Christopher JH Wort, and Geoffrey A Scarsbrook. The annealing of radiation damage in de beers colourless cvd diamond. *Diamond and Related Materials*, 3(4-6):932–935, 1994.

[268] Jingyuan Linda Zhang, Hitoshi Ishiwata, Thomas M Babinec, Marina Radulaski, Kai Muller, Konstantinos G Lagoudakis, Constantin Dory, Jeremy Dahl, Robert Edgington, Veronique Soulière, et al. Hybrid group iv nanophotonic structures incorporating diamond silicon-vacancy color centers. *Nano letters*, 16(1):212–217, 2016.

[269] Thomas Lutz, Tamiko Masuda, John P Hadden, Ilja Fescenko, Victor Acosta, Wolfgang Tittel, and Paul E Barclay. Influence of nanostructuring on silicon vacancy center spins in diamond pillars. *arXiv preprint arXiv:1908.01525*, 2019.

[270] Kenneth W Lee, Donghun Lee, Preeti Ovartchaiyapong, Joaquin Minguzzi, Jero R Maze, and Ania C Bleszynski Jayich. Strain coupling of a mechanical resonator to a single quantum emitter in diamond. *Physical Review Applied*, 6(3):034005, 2016.

[271] Yu Guo, Yexin Feng, and Lixin Zhang. Revealing the growth mechanism of siv centers in chemical vapor deposition of diamond. *Diamond and Related Materials*, 61:91–96, 2016.

[272] Je-Hyung Kim, Shahriar Aghaeimeibodi, Christopher JK Richardson, Richard P Leavitt, Dirk Englund, and Edo Waks. Hybrid integration of solid-state quantum emitters on a silicon photonic chip. *Nano letters*, 17(12):7394–7400, 2017.

[273] Iman Esmaeil Zadeh, Ali W Elshaari, Klaus D Jons, Andreas Fognini, Dan Dalacu, Philip J Poole, Michael E Reimer, and Val Zwiller. Deterministic integration of single photon sources in silicon based photonic circuits. *Nano Letters*, 16(4):2289–2294, 2016.

[274] AJ Neves and Maria Helena Nazaré. *Properties, growth and applications of diamond*. Number 26. IET, 2001.

[275] SC Rand and LG DeShazer. Visible color-center laser in diamond. *Optics letters*, 10(10):481–483, 1985.

[276] L-TS Lin, MA Prelas, and Galina Popovici. Laser modes in diamond. In *Wide Band Gap Electronic Materials*, pages 187–206. Springer, 1995.

[277] SC Rand. Synthetic diamond for color center lasers. In *Tunable Solid-State Lasers II*, pages 276–280. Springer, 1986.

[278] R Hammerling, Aaron B Budgor, and Albert Pinto. Tunable solid state lasers. Technical report, Springer-Verlag New York Inc., New York, NY, 1985.

[279] Takeru Nakashima and Shuji Yazu. Optical properties and laser action of h3 center in synthetic diamond. In *Diamond Optics III*, volume 1325, pages 10–16. International Society for Optics and Photonics, 1990.

[280] Jan Jeske, Desmond WM Lau, Xavier Vidal, Liam P McGuinness, Philipp Reineck, Brett C Johnson, Marcus W Doherty, Jeffrey C McCallum, Shinobu Onoda, Fedor Jelezko, et al. Stimulated emission from nitrogen-vacancy centres in diamond. *Nature communications*, 8(1):1–8, 2017.

[281] Alexander Savvin, Alexander Dormidonov, Evgeniya Smetanina, Vladimir Mitrokhin, Evgeniy Lipatov, Dmitriy Genin, Sergey Potanin, Alexander Yelisseyev, and Viktor Vins. Nv diamond laser. *arXiv preprint arXiv:2103.03784*, 2021.

[282] Siddharth Dhomkar, Pablo R Zangara, Jacob Henshaw, and Carlos A Meriles. On-demand generation of neutral and negatively charged silicon-vacancy centers in diamond. *Physical review letters*, 120(11):117401, 2018.

[283] Louis Nicolas, Tom Delord, Paul Huillery, Clément Pellet-Mary, and Gabriel Hétet. Sub-ghz linewidth ensembles of siv centers in a diamond nanopyramid revealed by charge state conversion. *ACS Photonics*, 6(10):2413–2420, 2019.

[284] Weng W Chow, Stephan W Koch, and Murray III Sargent. *Semiconductor-laser physics*. Springer Science & Business Media, 2012.

[285] P.W. Milonni and J.H. Eberly. *Laser Physics*. Wiley, 2010.

[286] A.E. Siegman. *Lasers*. University Science Books, 1986.

[287] Joel A Greenberg and Daniel J Gauthier. Steady-state, cavityless, multimode superradiance in a cold vapor. *Physical Review A*, 86(1):013823, 2012.

[288] Han-Wen Hu, Golam Haider, Yu-Ming Liao, Pradip Kumar Roy, Hung-I Lin, Shih-Yao Lin, and Yang-Fang Chen. Ultralow threshold cavity-free laser induced by total internal reflection. *ACS omega*, 5(30):18551–18556, 2020.

[289] Lachlan J Rogers, Kay D Jahnke, Marcus W Doherty, Andreas Dietrich, Liam P McGuinness, Christoph Müller, Tokuyuki Teraji, Hitoshi Sumiya, Junichi Isoya, Neil B Manson, et al. Electronic structure of the negatively charged silicon-vacancy center in diamond. *Physical Review B*, 89(23):235101, 2014.

[290] Stefan Häußler, Gergő Thiering, Andreas Dietrich, Niklas Waasem, Tokuyuki Teraji, Junichi Isoya, Takayuki Iwasaki, Mutsuko Hatano, Fedor Jelezko, Adam Gali, et al. Photo-luminescence excitation spectroscopy of siv- and gev- color center in diamond. *New Journal of Physics*, 19(6):063036, 2017.

[291] Elke Neu, Mario Agio, and Christoph Becher. Photophysics of single silicon vacancy centers in diamond: implications for single photon emission. *Optics express*, 20(18):19956–19971, 2012.

[292] Eduardo Granados, David J Spence, and Richard P Mildren. Deep ultraviolet diamond raman laser. *Optics express*, 19(11):10857–10863, 2011.

[293] J.C. Diels, W. Rudolph, and P.F. Liao. *Ultrashort Laser Pulse Phenomena: Fundamentals, Techniques, and Applications on a Femtosecond Time Scale*. Optics and photonics. Academic Press, 1996.

[294] Johannes Skaar. Fresnel equations and the refractive index of active media. *Physical Review E*, 73(2):026605, 2006.

[295] Kadir Durak, Chi Huan Nguyen, Victor Leong, Stanislav Straupe, and Christian Kurtsiefer. Diffraction-limited fabry–perot cavity in the near concentric regime. *New Journal of Physics*, 16(10):103002, 2014.

[296] Jingyuan Linda Zhang, Shuo Sun, Michael J Burek, Constantin Dory, Yan-Kai Tzeng, Kevin A Fischer, Yousif Kelaita, Konstantinos G Lagoudakis, Marina Radulaski, Zhi-Xun Shen, et al. Strongly cavity-enhanced spontaneous emission from silicon-vacancy centers in diamond. *Nano letters*, 18(2):1360–1365, 2018.

[297] Tom Feng and Bradley D Schwartz. Characteristics and origin of the 1.681 ev luminescence center in chemical-vapor-deposited diamond films. *Journal of applied physics*, 73(3):1415–1425, 1993.

[298] Justin B Spring, Benjamin J Metcalf, Peter C Humphreys, W Steven Kolthammer, Xian-Min Jin, Marco Barbieri, Animesh Datta, Nicholas Thomas-Peter, Nathan K Langford, Dmytro Kundys, et al. Boson sampling on a photonic chip. *Science*, 339(6121):798–801, 2013.

[299] Noel H Wan, Tsung-Ju Lu, Kevin C Chen, Michael P Walsh, Matthew E Trusheim, Lorenzo De Santis, Eric A Bersin, Isaac B Harris, Sara L Mouradian, Ian R Christen, et al. Large-scale integration of artificial atoms in hybrid photonic circuits. *Nature*, 583(7815):226–231, 2020.

[300] Lingyan He, Mian Zhang, Amirhassan Shams-Ansari, Rongrong Zhu, Cheng Wang, and Lončar Marko. Low-loss fiber-to-chip interface for lithium niobate photonic integrated circuits. *Optics letters*, 44(9):2314–2317, 2019.

[301] Junqiu Liu, Arslan S Raja, Martin HP Pfeiffer, Clemens Herkommer, Hairun Guo, Michael Zervas, Michael Geiselmann, and Tobias J Kippenberg. Double inverse nanotapers for efficient light coupling to integrated photonic devices. *Optics letters*, 43(14):3200–3203, 2018.

[302] W Redjem, A Durand, T Herzig, A Benali, S Pezzagna, J Meijer, A Yu Kuznetsov, HS Nguyen, Sébastien Cueff, J-M Gérard, et al. Single artificial atoms in silicon emitting at telecom wavelengths. *Nature Electronics*, pages 1–6, 2020.

[303] Michael Hollenbach, Yonder Berencén, Ulrich Kentsch, Manfred Helm, and Georgy V Astakhov. Engineering telecom single-photon emitters in silicon for scalable quantum photonics. *Optics Express*, 28(18):26111–26121, 2020.

[304] A Durand, Y Baron, W Redjem, T Herzig, A Benali, S Pezzagna, J Meijer, A Yu Kuznetsov, J-M Gérard, I Robert-Philip, et al. Broad diversity of near-infrared single-photon emitters in silicon. *arXiv preprint arXiv:2010.11068*, 2020.

[305] Tsung-Ju Lu, Benjamin Lienhard, Kwang-Yong Jeong, Hyowon Moon, Ava Iranmanesh, Gabriele Grosso, and Dirk Englund. Bright high-purity quantum emitters in aluminum nitride integrated photonics. *ACS Photonics*, 7(10):2650–2657, 2020.

[306] Yongzhou Xue, Hui Wang, Nan Xie, Qian Yang, Fujun Xu, Bo Shen, Jun-jie Shi, Desheng Jiang, Xiuming Dou, Tongjun Yu, et al. Single-photon emission from point defects in aluminum nitride films. *The Journal of Physical Chemistry Letters*, 11(7):2689–2694, 2020.

[307] Jianwei Wang, Stefano Paesani, Yunhong Ding, Raffaele Santagati, Paul Skrzypczyk, Alexia Salavrakos, Jordi Tura, Remigiusz Augusiak, Laura Mančinska, Davide Bacco, et al. Multidimensional quantum entanglement with large-scale integrated optics. *Science*, 360(6386):285–291, 2018.

[308] Tsung-Ju Lu, Michael Fanto, Hyeongrak Choi, Paul Thomas, Jeffrey Steidle, Sara Mouradian, Wei Kong, Di Zhu, Hyowon Moon, Karl Berggren, et al. Aluminum nitride integrated photonics platform for the ultraviolet to visible spectrum. *Optics express*, 26(9):11147–11160, 2018.

[309] Junqiu Liu, Guanhao Huang, Rui Ning Wang, Jijun He, Arslan S Raja, Tianyi Liu, Nils J Engelsen, and Tobias J Kippenberg. High-yield wafer-scale fabrication of ultralow-loss, dispersion-engineered silicon nitride photonic circuits. *arXiv preprint arXiv:2005.13949*, 2020.

[310] Yi Sun, Walter Shin, David Arto Laleyan, Ping Wang, Ayush Pandey, Xianhe Liu, Yuanpeng Wu, Mohammad Soltani, and Zetian Mi. Ultrahigh q microring resonators using a single-crystal aluminum-nitride-on-sapphire platform. *Optics letters*, 44(23):5679–5682, 2019.

[311] Jia Liu, Haizhong Weng, Adnan Ali Afridi, Jing Li, Jiangnan Dai, Xiang Ma, Hanling Long, Yi Zhang, Qiaoyin Lu, John F Donegan, et al. Photolithography allows high-q aln microresonators for near octave-spanning frequency comb and harmonic generation. *Optics Express*, 28(13):19270–19280, 2020.

[312] Sara L Mouradian and Dirk Englund. A tunable waveguide-coupled cavity design for scalable interfaces to solid-state quantum emitters. *APL Photonics*, 2(4):046103, 2017.

[313] Chi Xiong, Xiankai Sun, King Y Fong, and Hong X Tang. Integrated high frequency aluminum nitride optomechanical resonators. *Applied Physics Letters*, 100(17):171111, 2012.

[314] Efraim Rotem, Jeffrey M Shainline, and Jimmy M Xu. Electroluminescence of nanopatterned silicon with carbon implantation and solid phase epitaxial regrowth. *Optics express*, 15(21):14099–14106, 2007.

[315] KM Lee, KP O'donnell, J Weber, BC Cavenett, and GD Watkins. Optical detection of magnetic resonance for a deep-level defect in silicon. *Physical Review Letters*, 48(1):37, 1982.

[316] Bradley D Hauer, Paul H Kim, Callum Doolin, Allison JR MacDonald, Hugh Ramp, and John P Davis. On-chip cavity optomechanical coupling. *EPJ Techniques and Instrumentation*, 1(1):4, 2014.

List of Publications

JOURNAL ARTICLES

- Sichen Mi, Marcell Kiss, Teodoro Graziosi, and Niels Quack. Integrated photonic devices in single crystal diamond. Journal of Physics: Photonics, 2(4): 042001, 2020.

- Sichen Mi, Adrien Toros, Teodoro Graziosi, and Niels Quack. Non-contact polishing of single crystal diamond by ion beam etching. Diamond and Related Materials, 92: 248, 2019.

- Marcell Kiss, Sichen Mi, Gergely Huszka, and Niels Quack. Diamond diffractive optic: recent progress and perspectives. Advanced Optical Technologies (published online ahead of print) , 2020.

- Adrien Toros, Marcell Kiss, Teodoro Graziosi, Sichen Mi, Riad Berrazouane, Mehdi Naamoun, Jelena Vukajlovic Plestina, Pascal Gallo, and Niels Quack. Reactive ion etching of single crystal diamond by inductively coupled plasma: State of the art and catalog of recipes. Diamond and Related Materials, 108: 107839, 2020.

- Teodoro Graziosi, Sichen Mi, Marcell Kiss, and Niels Quack. Single crystal diamond micro-disk resonators by focused ion beam milling. APL Photonics, 3(12): 126101, 2018.

CONFERENCE PAPERS

- Sichen Mi, Christian Santschi, Marcell Kiss, Olivier J. F. Martin, and Niels Quack. Size control of self-organized gold nanoparticles on nanopatterned single crystal diamond. In 2018 International Conference on Optical MEMS and Nanophotonics (OMN), pages 1 - 5. IEEE, 2018.

- Teodoro Graziosi, Sichen Mi, Marcell Kiss, and Niels Quack. Freestanding optical micro-disk resonators in single-crystal diamond by reactive ion etching and multidirectional focused ion-beam milling. In Advances in Photonics of Quantum Computing, Memory, and Communication XI, volume 10547, page 105470R. International Society for Optics and Photonics, 2018.

- Teodoro Graziosi, Sichen Mi, Marcell Kiss, and Niels Quack. Enhancement of optical quality factor by thermal annealing of single crystal diamond microresonators. In 2018 International Conference on Optical MEMS and Nanophotonics (OMN), pages 1 - 5. IEEE, 2018.

PATENTS

- Niels Quack, Sichen Mi, Teodoro Graziosi, and Adrien Toros. Non-contact polishing of a crystalline layer or substrate by ion beam etching. 2020. WO2020021501.

Sichen Mi

Research interest:
quantum photonics, nonlinear optics, microfabrication

École Polytechnique Fédérale de Lausanne
Station 17, 1015 Lausanne, Switzerland
(+41) 021 693 77 73
sichen.mi@epfl.ch

EDUCATION

École Polytechnique Fédérale de Lausanne   Lausanne, Switzerland
Ph.D. in Photonics   *Feb. 2017 – Mar. 2021*

Beijing University of Posts and Telecommunications   Beijing, China
M.S. in Physics   *Sep. 2013 – Mar. 2016*

Central China Normal University   Wuhan, China
B.A. in Journalism, B.S. in Physics   *Sep. 2007 – Jun. 2011*

HONORS

IPRS Scholarship   May 2016
Queensland University   *Brisbane, Australia*

Outstanding Master Thesis   Mar. 2016
Beijing University of Posts and Telecommunications   *Beijing, China*

National Scholarship for Graduate Student   Dec. 2015
Ministry of Education of P.R.C.   *Beijing, China*

GRANTS

E.U. Project RADIATE   Transnational Access Grant
principle investigator on user project 20002237-ST   *Oct. 2020 – Present*

TALKS

Integrated Photonic Devices in Single Crystal Diamond [invited]   Jul. 2019
Beijing Normal University   *Beijing, China*

Dry Etching Approach for Diamond Fine Polishing [invited]   Jul. 2019
Huaqiao University   *Xiamen, China*

Ion Beam Polishing of SCD Substrates for Diamond Photonics Applications   May 2019
Symposium LATSIS 2019 on Diamond photonics   *Lausanne, Switzerland*

Self-organization of Diamond Surface during Ion Beam Etching   Sep. 2018
IEEE International Conference on Optical MEMS and Nanophotonics 2018   *Lausanne, Switzerland*

SKILLS

Cleanroom
   thin film, implantation, micro/nano 3D printing, photo/ebeam lithography, wet and ion beam dry etching, ICP-RIE

Characterization
   ellipsometry, AFM, SEM, Raman/photoluminescence/absorption spectroscopy, EDX, XRD, micro-CT

Programming
   Matlab, Mathematica, Python, Linux scripting, C/C++, SQL, NoSQL

Design
   FDTD, Comsol, QCAD, FreeCAD, FRED, DeScribe, L-Edit, Klayout, SRIM, LAMMPS

ACADEMIC SERVICES

Reviewer for Optics Express, Diamond and Related Materials